

DAMAGE DETECTION AND IDENTIFICATION
IN SANDWICH COMPOSITES USING
NEURAL NETWORKS

by

Andres Cecchini

A thesis submitted in partial fulfillment of the requirements for the degree of

MASTER OF SCIENCES
In
MECHANICAL ENGINEERING

UNIVERSITY OF PUERTO RICO
MAYAGÜEZ CAMPUS
2005

Approved by:

Frederick A. Just-Agosto, PhD
Member, Graduate Committee

Date

Abdul Basir Shafiq, PhD
Member, Graduate Committee

Date

David Serrano, ScD
President, Graduate Committee

Date

Luis A. Godoy, PhD
Representative of Graduate Studies

Date

Paul Sundaram, PhD
Chairperson of the Department

Date

Abstract

Marine, aerospace, ground and civil structures can receive unexpected loading that may compromise integrity during their life span. Therefore, improvement in detecting damage can save revenue and lives depending upon the application. The prognostic capability is usually a function of the examiner's experience, background and data collection during the evaluation. Nondestructive evaluation (NDE) methods are varied and specific to a given type of system (material, damage type, loading and environmental scenarios). As a result, one method of damage detection alone cannot examine all possible conditions and may even give false readings. In other words, by using more than one NDE technique, the probability of ensuring a more accurate detection increases. This work examined various existing NDE techniques to assess damage in sandwich composites structures including: vibration modal analysis, transient thermal response, and acoustic emission. Sandwich composites consisting of two carbon fiber/epoxy matrix face sheets laminated onto a urethane foam core were experimentally and analytically characterized using vibration, and thermal response to detect the presence of various types of damages. A neural network (NN) approach that uses vibration and thermal signatures to determine the condition of a composite sandwich structure is purposed. The data used to train a probabilistic neural network (PNN) were provided by numerical simulations. Literature offers substantial evidence of the validity of each of the chosen damage detection schemes separately. However, we will show that these methods can work jointly to complement each other in detecting the state of a sandwich composite structure.

Resumen

Las estructuras comunmente utilizadas en ingeniería sufren la acción de cargas impredecibles, la cuales puden comprometer su integridad durante la vida útil. Sin embargo, métodos de detección de daños mas sofisticados pueden evitar pérdidas económicas y humanas dependiendo de la aplicación. La capacidad de diagnostico predictivo depende de la experiencia de la persona que realiza la evaluación, de sus conocimientos previos y de la información obtenida durante la inspección. Además, los métodos no destructivos de evaluación son muy variados y específicos para cada tipo de material, daño, carga y aplicación. Por lo tanto, el uso de un único método no es suficiente para cubrir todas las posibles condiciones y podría producir falsos resultados. En otras palabras, usando varios métodos de evaluación simultaneamente aumenta la probabilidad de detección del daño. El presente trabajo examina algunos de los métodos no destructivos actualmente utilizados para evaluar daños en estructuras de materiales compuestos tipo sandwich como por ejemplo análisis modal de vibraciones, comportamiento termal en estado transitorio, emisiones acústicas, etc. Estructuras de material compuesto formadas por dos laminas de fibras de carbonos en una matriz de epoxy separadas por un nucleo de poliuretano liviano fueron estudiadas analítica y experimentalmente usando resultados termales y de vibraciones. Esta información es analizada y clasificada por un systema de redes neurales en busca de daños y defectos en el material. El proceso de aprendizaje del systema de redes se realizó usando resultados obtenidos de modelos numéricos. Aunque los métodos no destructivos antes mencionados funcionan bien por si solos, aqui mostraremos que pueden trabajar conjuntamente complementandose entre ellos en la deteccion de daños en este tipo de materiales.

Acknowledgments

I would like to thank my advisor Dr. David Serrano for his constant guidance and support throughout this research. I also would like to thank the member of my graduated committee Dr. Fred Just and Dr. Basir Shafiq for their help and disposition. Finally, I would like to thank Dr. Sergio Preidikman for his advice and friendship.

Contents

List of Tables.....	vii
List of Figures.....	viii
Chapter 1: Introduction.....	2
1.1 Introduction.....	2
1.2 Objectives.....	5
1.3 Non Destructive Inspection Technologies.....	6
1.4 Structural Health Monitoring and Damage Detection.....	8
1.5 Data Processing Intelligent Systems.....	10
1.6 Sandwich Composite Materials.....	11
1.7 Approach: Innovative Aspect of the Research.....	15
Chapter 2: Literature Review.....	16
2.1 Vibration Based Techniques.....	16
2.2 Thermal Based Techniques.....	19
2.3 Acoustic Emission Based Techniques.....	20
2.4 Other Techniques.....	21
Chapter 3: Vibrations Analysis.....	25
3.1 Vibrations Problem.....	25
3.1.1 Equations of Motion.....	25
3.1.2 The Eigen Problem.....	26
3.2 Numerical Model.....	27
3.3 Fitting Model Parameters.....	29
3.4 Curvature Finite Difference Approximation.....	36
3.5 Undamaged Case.....	37
3.6 Damaged Case.....	38
3.6.1 Simple Damage Scenarios.....	39
3.6.2 Multiple Damages Scenarios.....	43
3.7 Scope of the Method.....	45
Chapter 4: Thermal Analysis.....	49
4.1 Heat Transfer Problem.....	49
4.1.1 Problem Formulation.....	49
4.2 Numerical Model.....	56
4.3 Undamaged Case.....	58
4.4 Damaged Case.....	60
4.4.1 Simple Damage Scenarios.....	60
4.4.2 Multiple Damages Scenarios.....	63
4.5 Scope of the Method.....	63

Chapter 5: Experimental Validation	64
5.1 Introduction.....	64
5.2 Modal Testing.....	64
5.2.1 Test Specimens.....	67
5.2.2 Experimental Set Up.....	68
5.2.3 Results.....	69
5.3 Infrared Thermography Testing.....	81
5.3.1 Test Specimens.....	81
5.3.2 Experimental Set Up.....	82
5.3.3 Results.....	83
Chapter 6: Neural Network Implementation	97
6.1 Preface.....	97
6.2 Neural Network Selection.....	100
6.3 Curvature Method.....	102
6.3.1 Simple Damage Scenarios.....	104
6.3.2 Multiple Damages Scenarios.....	107
6.4 Thermal Method.....	116
6.4.1 Simple Damage Scenarios.....	118
6.4.2 Multiple Damages Scenarios.....	124
6.5 Curvature and Thermal Approaches Together.....	124
Chapter 7: Conclusions and Future Work	126
References	128
Appendix A: Matlab Code for Damage Detection	134

List of Tables

3.1	First three natural frequencies of an aluminum beam.....	28
3.2	Linear thin composite element properties.....	29
3.3	Linear isotropic brick element properties.....	30
3.4	First three experimental natural frequencies.....	30
3.5	Elastic properties used in the FE model.....	35
3.6	First three natural frequencies for the intact FE beam.....	35
3.7	Natural frequencies of damaged FE beam.....	39
3.8	Idem of different damage locations.....	41
4.1	FV model parameters.....	57
5.1	Experimental natural frequencies of the undamaged beam.....	70
5.2	Experimental natural frequencies of the damaged beam 1.....	74
6.1	Training with curvature damage scenarios.....	104
6.2	Results from curvature test damage cases.....	107
6.3	Training with thermal damage scenarios.....	121
6.4	Results from thermal test damage cases.....	123

List of Figures

1.1	Sandwich composite panel.....	12
1.2	Face yielding mode of failure.....	13
1.3	Face wrinkling mode of failure.....	13
1.4	Core failure mode.....	13
1.5	Failure of de adhesive bond.....	14
1.6	Core indentation.....	14
1.7	Neural network approach.....	15
2.1	Shaerographic excitation: c) idem images of damages: a) with thermal excitation; b) vibratory.....	22
2.2	EMIR method: a) transmission configuration; b) interferometric configuration; c) detection of water trapped in damaged sandwich; d) idem by interferometric technique: amplitude image; e) idem: phase image; f) idem by transmission technique (amplitude image).....	23
3.1	FE model and coordinate system.....	27
3.2	Variation of the objective function with respect to the face sheet a) mass density; b) longitudinal modulus of elasticity; c) transversal modulus of elasticity; d) mayor poisson ratio; e) minor poisson ratio; f) shear modulus of elasticity	31
3.3	Variation of the objective function with respect to the foam core g) mass density; h) modulus of elasticity; i) poisson ratio; j) shear modulus o elasticity.....	32
3.4	Quadratic interpolation method.....	33
3.5	Convergence of the quadratic interpolation method.....	34
3.6	Node location in the FE model.....	37
3.7	First three flexural mode shapes for the intact beam.....	38
3.8	Curvature mode shapes for the intact beam.....	38
3.9	FE model of damage case 2.....	39
3.10	Mode shapes for the damaged beam 2.....	40
3.11	Curvature mode shapes for the damaged beam 2.....	40
3.12	Difference in curvature mode shapes for the damage case 2.....	41
3.13	Difference in curvature mode shapes for the damage case 1.....	42
3.14	Difference in curvature mode shapes for the damage case 3.....	42
3.15	Difference in curvature mode shapes for the damage case 4.....	42
3.16	Difference in curvature mode shapes for the damage case 5.....	43
3.17	FE model of multiple damages (case 6).....	43
3.18	Difference in curvature mode shapes for the damage case 6.....	44
3.19	FE model of damage case 7.....	44
3.20	Difference in curvature mode shapes for the damage case 7.....	45
3.21	FE model of damage case 8.....	45

3.22	Mode shapes for the damaged beam 8.....	46
3.23	Curvature mode shapes for the damaged beam 8.....	46
3.24	Difference in curvature mode shapes for the damage case 8.....	46
3.25	FE model of damage case 9.....	47
3.26	Difference in curvature mode shapes for the damage case 9.....	47
3.27	FE model of damage case 10.....	48
3.28	Difference in curvature mode shapes for the damage case 10.....	48
4.1	Convection heat transfer coefficient.....	51
4.2	One dimensional FV model.....	52
4.3	Block diagram of CGSTAB code.....	55
4.4	Three dimensional FV mesh.....	56
4.5	Initial temperature distribution.....	57
4.6	Surface thermal distribution of the undamaged case: a) 5 sec.; b) 10 sec.; c) 15 sec.; d) 20 sec.; e) 25 sec.; f) 30 sec.; g) 35 sec.; h) 40 sec.; i) 45 sec.; j) 50 sec.; k) 55 sec.; l) 60sec.....	58
4.7	Idem for damage case 1: a) 10 sec.; b) 15 sec.; c) 30 sec.; d) 35 sec.....	60
4.8	Idem for damage case 2: a) 50 sec.; b) 55 sec.....	61
4.9	Idem for damage case 3: a) 5 sec.; b) 15 sec.; c) 30 sec.; d) 35 sec.....	62
4.10	Idem for damage case 4: a) 50 sec.; b) 55 sec.....	62
4.11	Idem for multiple damage case 5: a) 15 sec.; b) 20 sec.....	63
5.1	FRF $H(\omega)$ definition.....	65
5.2	Typical FRF plots.....	66
5.3	Classical log magnitude plot of FRFs.....	66
5.4	Modal testing set up.....	68
5.5	Bode plot of the undamaged beam.....	70
5.6	Experimental measuring nodes.....	71
5.7	Experimental mode shapes of the intact beam.....	71
5.8	Experimental curvature mode shapes of the intact beam.....	71
5.9	FEA and experimental results of the undamaged case, mode shape 1.....	72
5.10	Idem, mode shape 2.....	72
5.11	Idem, mode shape 3.....	72
5.12	Damage case 1.....	73
5.13	Bode plot of the damaged beam 1.....	73
5.14	Experimental mode shapes of the damaged beam 1.....	74
5.15	Experimental curvature mode shapes of the damaged beam 1.....	74
5.16	FEA and experimental results of the damaged beam 1, mode shape 1.....	75
5.17	Idem, mode shape 2.....	75
5.18	Idem, mode shape 3.....	75
5.19	FEA and measured results of the damage beam 1, difference in curvature mode shape 1.....	76
5.20	Idem difference in curvature mode shape 2.....	76
5.21	Idem difference in curvature mode shape 3.....	76
5.22	Difference in curvature mode shapes, damaged beam 1.....	77

5.23	Damage case 2.....	77
5.24	Difference in curvature mode shapes, damaged beam 2.....	77
5.25	Damage case 3.....	78
5.26	Experimental mode shapes of the damaged beam 3.....	78
5.27	Experimental curvature mode shapes of the damaged beam 3.....	78
5.28	Difference in curvature mode shapes, damaged beam 3.....	78
5.29	Damage case 4.....	79
5.30	Difference in curvature mode shapes, damaged beam 4.....	79
5.31	Difference in curvature mode shapes, damaged beam 5.....	80
5.32	Difference in curvature mode shapes, damaged beam 6.....	80
5.33	IR thermography testing set up.....	82
5.34	Thermal response of the undamaged case: a) 5 sec.; b) 10 sec.; c) 15 sec.; d) 20 sec.; e) 25 sec.; f) 30 sec.; g) 35 sec.; h) 40 sec.; i) 45 sec.; j) 50 sec.; k) 55 sec.; l) 60 sec.....	83
5.35	Damage case 1.....	86
5.36	Thermal response of the damaged case 1: a) 5 sec.; b) 10 sec.; c) 15 sec.; d) 20 sec.; e) 25 sec.; f) 30 sec.; g) 35 sec.; h) 40 sec.; i) 45 sec.; j) 50 sec.; k) 55 sec.; l) 60 sec.....	86
5.37	Idem, damage case 2.....	89
5.38	Damage case 3.....	91
5.39	Thermal response of the damage case 3, a) 5 sec.; b) 10 sec.; c) 30 sec.; d) 35 sec.....	91
5.40	Damage case 4.....	92
5.41	Thermal response of the damage case 4, a) 50sec.; b) 55 sec.....	93
5.42	Damage case 5.....	93
	Thermal response of damage case 5 , a) 5 sec.; b) 10 sec.; c) 15 sec.; d) 20 sec.; e) 25 sec.; f) 30 sec.; g) 35 sec.; h) 40 sec.; i) 45 sec.; j) 50 sec.; k) 55 sec.; l) 60 sec.....	94
6.1	NN diagram.....	98
6.2	PNN architecture.....	101
6.3	NN scheme for curvature data classification.....	103
6.4	NN curvature training data: a); b); c) and bond failures; e) surface crack; f) surface indentation.....	105
6.5	NN curvature test data: a); b); c); and e) bond failures; d) core failure; f) surface crack.....	106
6.6	NN multiple damage curvature test data N6: bond failures.....	108
6.7	Curvature peaks: a) curvature peaks of mode shape 1 of damage case N6; b) peak 1; c) peak 2;.....	109
6.8	Idem for curvature peaks of mode shape 2.....	110
6.9	Idem for curvature peaks of mode shape 3.....	111
6.10	NN multiple damage curvature test data N7: bond failures.....	112
6.11	Curvature peaks: a) curvature peaks of mode shape 1 of damage case N7; b) peak 1; c) peak 2;.....	113

6.12	Idem for curvature peaks of mode shape 2.....	114
6.13	Idem for curvature peaks of mode shape 3.....	115
6.14	Pre processing scheme of IR thermal image.....	117
6.15	NN scheme for thermal data classification.....	118
6.16	NN thermal training data: a) indentation 15 sec.; b) idem 50 sec.; c) notch 10 sec.; d) crack 55 sec.; e) indentation 15 sec.; f) idem; g) idem; h) idem 35 sec...	119
6.17	NN training contours: a) indentation 15 sec.; b) idem 50 sec.; c) notch 10 sec.; d) crack 55 sec.; e) indentation 15 sec.; f) idem; g) idem; h) idem 35 sec.....	120
6.18	NN thermal test data: a) indentation 30 sec.; b) crack 50sec.; c) indentations 15 sec.; d) indentation 15 sec.; e) idem 30 sec.; f) idem 50 sec...	122
6.19	NN test contours: a) indentation 30 sec.; b) crack 50sec.; c) indentations 15 sec.; d) indentation 15 sec.; e) idem 30 sec.; f) idem 50 sec...	123
6.20	General NN approach for damage detection.....	125

Chapter 1

Introduction

This first chapter introduces to the basic concepts and terms related to the damage detection subject. Some important topics are discussed in order to understand the methodology followed in this work. Finally, we describe our motivation and the innovative aspect of the research.

1.1 Introduction

The subject of structural health monitoring has been receiving a growing amount of interest from researchers in diverse fields of engineering. Nondestructive inspection techniques are generally used to investigate the critical changes in the structural parameters so that an unexpected failure can be prevented. Although there are many techniques and approaches involved in the nondestructive evaluation (NDE) of structural systems [1], they can all be mostly categorized as local or global methods. The first class includes methods designed to provide information about a relatively small region of the structure under study by using local measurements. Examples include acoustic techniques, thermal field methods or curvature approach. The second class of methods uses global measurements to determine the general state of the system. Vibration methods which involve measurement of natural frequencies fit into this category. Clearly, the two approaches are complementary to each other, with the optimum selection of method highly dependent on the scope of the problem at hand. In this study, local methods that concentrate on a part of the structure are used to detect, locate and quantify damages. One of the primary considerations when selecting a nondestructive testing technique is, whether it is capable of detecting the existing defect with sufficiently high

probability. This establishes the threshold rejection criterion of whether the component is fit for service.

Not all NDE techniques are physically capable of detecting all damages. Each one has its own limitations. The capability of a method depends on the inherent limitations of the procedure used. Among the promising NDE methods are those based on the analysis of structural dynamic response measurements to identify a suitable mathematical model corresponding to the state of the physical structure. Deterioration and damage result in a reduction in the structural stiffness. This reduction produces significant changes in the dynamic properties, such as natural frequencies, mode shapes and structural damping. Since the measurement of natural frequencies is easier than that of changes in structural damping, damage can be detected from dynamic analysis using natural frequencies and mode shapes. Although changes in natural frequencies give a useful indication of the existence of damage, it can be concluded that a damage identification method based on this feature is not sufficient to locate the damage [2]. Therefore, mode shapes information is required to determine the location of the damage. Since displacements and curvature mode shapes can be obtained by both experimental as well as numerical means, this work focuses on damage detection techniques that use this information. Later, the difference between the undamaged and damaged state is performed to improve damage detection. As previous mentioned this technique produces successful results in detecting and locating damages which cause significantly reduction on stiffness of the structure. However, this approach may give problems in dealing with thin and light structures, as panels of composite materials, where, if the defect is small, natural mode shapes may mask the local vibration pattern induced by the fault. For these cases, it is necessary to use another non destructive inspection technique that complements the vibration method.

Thermal analysis is a method based on the acquisition of external surface temperature distribution data from a specimen in response to a thermal transient excitation induced by external heating and exposed to free convection. The purpose of using thermal techniques

is to show that the temperature distribution over the sample changes significantly due to a severe variation in the mechanical properties and this feature could be related to a specific damage. There exist others NDE techniques which can be used for damage characterization purposes. Acoustic emission testing will be considered as an alternative method.

While there are many approaches that have been investigated and are still being developed for signature based NDE of structures, the class of health monitoring approaches that do not require detailed knowledge of the vulnerable parts of the structure or of the failure modes of the structure, have a significant advantage in that they have the potential to handle unexpected failure patterns. Among the structure identification approaches that have been receiving growing attention recently are artificial neural networks (ANNs). Several studies [3] have demonstrated that ANNs are a powerful tool for identification of systems typically encountered in the structural dynamics field.

ANNs were originally developed to simulate the function of the human brain or neural system, resulting in systems that learn by experience. The use of ANNs has increased dramatically in recent years in the applied mechanics field in order to model complex system behavior. Its potential has been recognized in the field of monitoring and control of structural systems [4]. The primary strengths of ANN methods in this context are that they can potentially deal with demanding problems of robustness, complex nonlinear systems and online identification. In view of the strong interest that ANNs have generated in the computational mechanics community, it is not surprising that investigators have started to evaluate the suitability and capabilities of these networks for damage detection purposes. Several studies [5-8] have demonstrated that these neural networks (NNs) offer a powerful tool for assessing the condition of structures with inherent damage.

1.2 Objectives

The aim of this work is the development of an intelligent system for data processing and defect characterization to detect and identify the location and extent of damages in sandwich composites structures. In particular, this system was tested for pattern recognition using both numerical and experimental data from different sources such as thermal, acoustic and vibration analysis. Among these diagnostic techniques, the most largely studied and applied are those based on vibration measurements. In this field, several strategies for structural excitation, vibration measurement and data processing have been presented. However, this approach may give problems in cases where the defect is too small to change the modal parameters (natural frequencies and mode shapes). Therefore, three nondestructive techniques were studied in this work to obtain diverse information that allows the evaluation of the health of the structure under investigation. The fundamental curvature mode shapes were used locally to identify the damage sites corresponding to a reduction in stiffness, which show up as spikes in the curve, while thermal distribution images were generated to detect a variation in mechanical properties such as thermal conductivity, specific heat or mass density. The third technique to be considered was acoustic emission (AE) analysis, which produced additional information about the localization and scale of damages.

In order to handle this information and to identify combined cases, it is important that the data be presented or modeled in a unified framework. Three dimensional numerical models of sandwich composite structures with several different defects were used to generate damage scenarios to train an ANN. This NN was later employed to classify the measured data, previously processed with dedicated algorithms for feature extraction. The selection of the most appropriate NN model, based on its performance in pattern recognition applications, was a very important consideration of the thesis. A procedure to generate a training set from numerical models is proposed.

The processing system was tested and optimized on the numerical data, before final application to real experimental results. The issues to be resolved in this thesis are summarized in the topics stated below:

1. To select appropriate NDE techniques in order to investigate critical changes in structural parameters.
2. To find an adequate NN architecture based on its performance in data classification.
3. To use features extraction techniques to the data before the NN implementation.
4. To create and validate numerical models to generate different damage scenarios.
5. To unify the NN application in order to interpret the information from different NDE methods.
6. To perform experimental analysis to test the feasibility of the proposed approach in detecting real damage cases.

1.3 Nondestructive Inspection Technology

Nondestructive testing (NDT) is a branch of the materials sciences that is concerned with all aspects of the uniformity, quality and serviceability of materials and structures. Essentially, NDT refers to all the methods which allow testing or inspection of a system without impairing its future usefulness even without taking it out of service [9]. The science of NDT incorporates all the technology for detection and measurement of significant properties. In other words, the purpose of NDT is to determine whether a material or a component will satisfactorily perform its intended function. By using NDE methods and techniques, it is possible to decrease the factor of ignorance about a system without decreasing its factor of safety. In general, the use of NDT will fall into one of the following categories:

1. Determination of material properties.
2. Detection, characterization, location and sizing of discontinuities or defects.

3. Determining quality of manufacture or fabrication of a component or structure.
4. Checking for deterioration after a period of service for a component or structure.

Some of the benefits derived from NDT are increased productivity, improved serviceability and safety. Increased serviceability of equipment and materials will result through the application of NDE methods and techniques that find and locate defects which may cause malfunctioning or breakdown of equipment. A variety of NDE techniques have been developed to detect and characterize defects. All the NDE techniques are based on physical principles. Practically, every form of energy has been used in NDE. Similarly, nearly every property of the materials to be inspected has been made the basis for some method or technique. Almost all methods of NDE involve subjecting the specimen being examined to some form of external energy source and analyzing the detected response signals. The essential parts of any NDE test are:

1. Application of a testing or inspection medium.
2. Modification of the testing or inspection medium by defects or variations in the structure or properties of the material.
3. Detection of these changes by suitable detector.
4. Conversion of these changes into a suitable detector.
5. Interpretation of the information obtained.

It is important that the interpretation of the NDE results be made by an experienced or skilled person or computer [9]. Interpretation of the results sometimes determines the success or failure of a test method or technique. The most popular NDE techniques currently used are:

1. Ultrasonic testing.
2. Radiography (X-ray, Gamma-ray, etc.).
3. Eddy current testing.
4. Liquid penetrant testing.

5. Magnetic (particle, flux leakage, etc.).
6. Acoustic emission testing.
7. Infrared thermography.
8. Visual testing (optical).
9. Vibration Testing.

However, ultrasonic testing, radiography, liquid penetrant, magnetic particles and visual testing are not suitable for structural health monitoring (SHM) application. On the other hand, eddy current testing is applicable only to conductive materials while acoustic emission testing is a real time method of damage detection.

In many types of NDT, the sensitivity of the technique depends upon the ability to distinguish the significant part of the signal from the general background due to noise or inherent background signals from the material being examined. The power and speed of modern computers, signal processing methods and modeling numerical methods have allowed remarkable developments took in NDE techniques. Significant improvements have been made both in the NDT equipment and in the specific techniques used. Similarly, use of multiple NDT sensors, NDE techniques and computer assisted processing in modern nondestructive inspection systems have reduced costs by increasing both the speed and reliability of inspection.

1.4 Structural Health Monitoring and Damage Detection

The process of implementing a damage detection strategy for engineering structure is referred to as Structural Health Monitoring (SHM) [10]. The SHM process involves the observation of a system over time using periodically sampled response measurements from an array of sensors. The extraction of damage sensitive features from these measurements and the statistical analysis of these features are then used to determine the current state of system health. SHM essentially involves the embedding of an NDE

system (or a set of NDE systems) into a structure to allow continuous remote monitoring for damage. There are several advantages to using a SHM system over traditional inspection cycles, such as reduced down time, elimination of component tear down inspections and the potential prevention of failure during operation.

Damage characterization is probably the most fundamental aspect of detecting damage, the familiarity of what kinds of damage are common in a type of material or structure, and the knowledge of what reasonable changes in properties correspond to these forms of damage. These damage characteristics depend on the type of material the structure is constructed with, as well as the structural configuration. With metallic structures, designers and operators are mostly concerned with fatigue cracks and corrosion, while for composite materials, delaminations and impact damage are more of a concern. Once an understanding of the damage signature in the material of concern is reached, then the sensing method and sensors can be selected.

Sensors are used to record variables such as strain, acceleration, sound waves, electrical or magnetic impedance, pressure or temperature. A SHM system requires a specific number of sensors, depending on its size, arrangement and desired coverage area. Sensing systems can generally be divided into two classes: passive or active sampling. Passive sampling systems are those that operate by detecting responses due to perturbations of ambient conditions without any artificially introduced energy. Several vibrational techniques can be performed passively, with the use of accelerometers, ambient frequency response and acoustic emission with piezoelectric wafers. Active sampling systems are those that require externally supplied energy to properly function. A few strain based examples of active systems include electrical and magnetic impedance measurements. Active vibrational techniques include the transfer function based modal analysis. Passive techniques tend to be simpler to implement and operate with a SHM system and provide useful global damage detection capabilities, however generally active methods are more accurate in providing localized information about a damaged area. An

effective design of a structural health monitoring system will use several different sensing methods, taking advantage of both the strengths and weaknesses of each one.

1.5 Data Processing Intelligent Systems

Algorithms are probably the most essential component of a SHM system. They are necessary to decipher and interpret the collected data. Examples of algorithms that have been used include spectral analysis, expert systems (ES) and codes that perform wavelet decomposition. Spectral analysis [11] involves the frequency response function (FRF) using the fast Fourier transform algorithm. This technique provides a quick and accurate approach in obtaining structural FRFs that may be used to extract parameters.

Wavelet analysis may be viewed as an extension of the traditional Fourier transform (FT) with adjustable window location and size [12]. The merits of wavelet analysis lie in its ability to examine local data to provide multiple levels of details and approximations of the original signal. Therefore, transient behavior of the data can be retained. However, other algorithms are more appropriate for implementing in fault diagnosis and detection such as rule based ES, fuzzy logic systems and ANNs.

A rule based ES is defined [13] as one which contains information obtained from a human expert and represents that information in the form of rules, such as IF-THEN. The rule can then be used to perform operations on data to inference in order to reach appropriate conclusion. These inferences are essentially a computer code that provides a methodology for reasoning about information in the rule base or knowledge base, and for formulating conclusions.

On the other hand, fuzzy systems are based on membership functions and rules of association that process vague, imprecise or ambiguous information [14]. The proper selection of these functions and rules is essential to successful development of a fuzzy

logic based decision system. Known inputs and corresponding correct decisions are used to generate the membership functions used to develop the rule base. Fuzzy sets are commonly predetermined or manually defined. This teaching method is referred to as supervised learning because the fuzzy sets are prescribed.

Other architectures, such as ANNs have the advantage of using unsupervised learning [13]. An unsupervised system learns from training data that are clustered into patterns to form classes. In recent years, there has been a growing interest in using ANNs, a computing technique that operate in a manner analogous to that of biological nervous systems. This concept is used to implement software simulations for the massively parallel processes that involve processing elements interconnected in network architecture. ANNs are suitable for pattern classification and natural information processing tasks and they are finding applications in almost all branches of science and engineering.

The current work deals with the recognition of features extracted from different NDE tests. This information could be represented in diverse formats or contaminated by noise due to various reasons. Besides, some discrepancies may occur when matching these features with known patterns. To solve these issues a statistical based approach should be implemented such as Bayesian classifier [15] which stores a single probabilistic summary for each class. Probabilistic neural networks (PNNs) belong to Bayesian classifiers and are used for classification problems. Bayesian NN will be discussed in detail in chapter 6.

1.6 Sandwich Composite Materials

The sandwich structure is a composite configuration that consists of high strength composite facing sheets bonded to a lightweight foam or honeycomb core (Figure 1.1). Examples of these structures include skins made of glass/carbon/Kevlar fibers in vinyl ester/epoxy matrix bonded and separated by an aluminum honeycomb or polyurethane

foam. Sandwich structures have extremely high flexural stiffness to weight ratios and widely used in mechanical structures such as airplanes and ships. The design flexibility offered by these and other composite configurations is obviously quite attractive to designers, and the potential now exists to design not only the structure, but also the structural material itself. We are interested in carbon fiber – epoxy skins with polyurethane foam panels due to the relevance of this material for the NAVY.

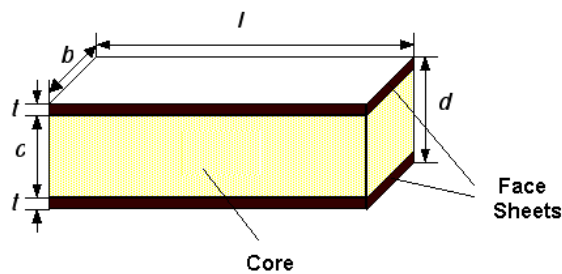


Figure 1.1: Sandwich composite panel.

The disadvantage, however, is that composite materials present challenges for design, maintenance and repair over metallic parts since they tend to fail by combined failures modes [16]. Furthermore, damage detection in composites is much more difficult due to the anisotropy of the material, the conductivity of the fibers, the insulative properties of the matrix, and the fact that much of the damage often occurs beneath the top surface of the laminate. There are 5 principal modes of failure of sandwich composites with foam cores:

1. *Yielding or Fracture* of the tensile face sheet
2. *Buckling or Wrinkling* of the compression face sheet
3. *Failure of the core* in shear although there is also a lesser possibility of tensile or compressive failure of the core
4. *Failure of the bond* between the face sheet and the core
5. *Indentation* of the faces and core at the loading points

Face Yielding

Face yielding (Figure 1.2) occurs when the normal tensile stress in the face equals the strength (yield strength for ductile face sheet materials, fracture strength for brittle face sheet materials).



Figure 1.2.

Face Wrinkling

Face wrinkling (Figure 1.3) occurs when the normal stress in the compression face sheet of the beam reaches the level of instability (buckling).



Figure 1.3.

Core Failure

The core will fail when the principal stresses in the core combine to exceed the yield criterion (Figure 1.4). Generally, the shear stresses in the core are large compared with the normal stresses and so failure will occur when the maximum shear stress in the core exceeds the shear yield strength of the core. This shear yield strength corresponds to plastic bending of the cell walls about the cell edges which in turn depends on the foam density and the yield strength of the foam substrate.

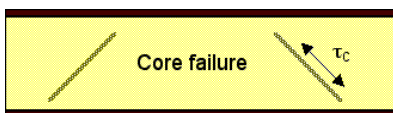


Figure 1.4.

Failure of the Adhesive Bond

Failure of the adhesive bond between the face sheet and the core is a very important failure mechanism (Figure 1.5). For polymer matrix composites skins bonded to foam cores, the epoxy used to make the bond is usually stronger than the foam and failure will generally occur in the foam, not the bond. However, if a crack like defect exists in the bond, such as might arise from incomplete coverage of the adhesive or a trapped air pocket for in situ foamed composites, then failure can occur in the bond plane by extension of the crack. Both cases are included into this failure mode.

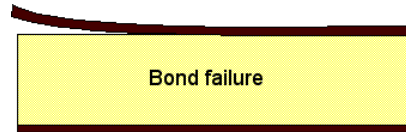


Figure 1.5.

Core Indentation

The problem of indentation of the core only occurs when loads are highly localized and arises because the stress immediately under the loading point is greater than the crushing strength of the core (Figure 1.6).

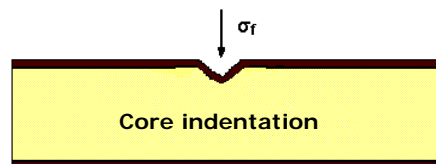


Figure 1.6.

In addition, other types of failures [17] can occur in the laminated composite (face sheet) such as fiber breaking, debonding, matrix microcracking and delamination. Those defects that produce a significant reduction in stiffness of the structure are expected to be detected by changes in the dynamic parameters (natural frequencies, damping ratio and

mode shapes) while others faults are examined by using thermal images and acoustic emission techniques.

1.7 Approach: Innovative Aspect of the Research

Many NDE techniques (mentioned in section 1.3) have been used to localize and identify damages in a structure and several algorithms (discussed in section 1.5) have been implemented to characterize these defects. However, a combined method of NDE techniques could be more effective in detecting different kind of damages or a combination of those. These NDE techniques will complement to each other and a particular defect in the structure could be localized by one or more technique.

The approach of this work consists of using measurements from diverse NDE techniques to identify damages in sandwich composites materials using NNs. As mentioned in section 1.3, vibration measurements, infrared thermography and acoustic emission testing are considered in this study. Data for the training process of the NN will be provided by finite element simulations. Once properly trained, the neural network will in theory provide damage information when measured structural responses are presented to the system. Figure 1.7 shows schematically the NN approach.

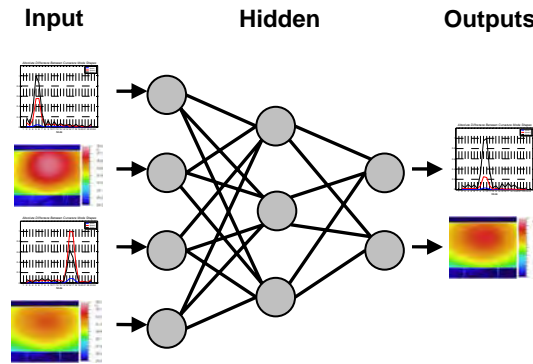


Figure 1.7: NN approach.

Chapter 2

Literature Review

The following chapter focuses on mentioning some of the previous works done in damage detection subject. These works are classified according to the NDE technique used for damage characterization. Other NDE based methods which were not mentioned in the previous chapter are discussed in section 2.4.

1.6 Vibrations Based Techniques

Any localized defect in a structure reduces the stiffness and modifies the damping in the damaged area. These features are related to variation in the dynamic properties, such as, decreases in natural frequencies and modification of the modes of vibration of the structure. One or more of above characteristics can be used to detect and locate damages.

Pandey, Biswas and Samman [18] investigated the curvature mode shapes as a possible candidate for detecting cracks. It was shown that the absolute changes in the curvature mode shapes are localized in the region of damage and hence can be used to detect defects in a structure. Finite element analysis (FEA) was performed for two models, a cantilever and a simply supported isotropic beam, to obtain the displacement mode shapes. No experimental verification was performed in this work.

Adams and Cawley [19] employed a sensitivity analysis to deduce the location of damage in two dimensional (2D) structures, based only on FEA. Flexural modes of vibration were used in this case. The method was applied to the case of a metallic flat plate with the assumption that the modulus of elasticity in the damage area was equal to zero.

Ratcliffe and Bagaria [20] presented an experimental nondestructive vibration based technique for locating damages in a composite beam. The study was limited to delaminations. The method operates on the fundamental displacement eigenvectors, which are converted into a curvature mode shapes. Then, to extract small features the curvature was locally smoothed with a gapped cubic polynomial. This procedure could operate solely on data obtained from the damaged structure. The damage location method was tested by using a FE model of a composite beam before experimental demonstration.

Ratcliffe [21] also developed a technique for identifying the location of structural damage in a beam using a 1D FEA. A finite difference approximation called Laplace's differential operator was applied to the mode shapes to identify the location of the damage. This procedure is best suited to the mode shapes obtained from fundamental natural frequencies. In both cases [20-21], the interpretation of the data was done visually.

Zhao, Ivan and DeWolf [22] consider in their investigation a variety of diagnostic parameters, including static displacements, natural frequencies, mode shapes and other parameters based on mode shapes (slope array and state array). The method used was a counter propagation neural network (CPNN) and it was applied only to continuous beam FE models. It was concluded that there is no approach that has consistent advantages over others. The best way is to use multiple approaches at the same time to produce reliable results.

Byon and Nishi [23] presented the application of hierarchical NNs for damage identification in a carbon fiber reinforced plastic (CFRP) laminated beam. Damage was introduced in the test specimen by cutting the unidirectional prepreg and replacing with teflon film. When the first three natural frequencies and/or the third mode shape of the beam were used as inputs data, NN estimated the exact location and amount of damage.

Toro, Shafiq, Serrano and Just [24] applied an eigen parameter based technique to detect localized damage in geometrically complex sandwich composite structures using 3D orthotropic FEA. It was shown that the fundamental displacement mode shape curvature of a sandwich structure could be used to identify the unique damage sites corresponding to a reduction in stiffness. A segment wise analysis approach was suggested for non planar or discontinuous structures. PNNs were used to aid in damage detection of 3D geometries based on training performed with the finite element simulations.

Sahin and Shenoi [25] investigated the effectiveness of the combination of global and local vibration based analysis data as input for a feedforward back propagation ANN for location and severity prediction of damage in fiber reinforced plastic laminates. Later, the authors [26] performed the same analysis over steel beams using strain gauges and accelerometers to obtain resonant frequencies and strain mode shapes. In both cases studied, the selection of features as input data was considered crucial in the accuracy of prediction of damage. They concluded that although reduction in natural frequencies is considered as an indicator for the existence of the damage and its severity, it did not provide any useful information about the location of the damage.

Kessler, Spearing, Atalla, Cesnik and Soutis [27] presented an experimental and analytical method for the in situ detection of damage in composite materials. Modal analysis techniques (frequency response and impedance) were applied to graphite/epoxy specimens containing representative damage modes such as holes, deformation by impact and delaminations. A limitation of this method is that not much information about the specific location or type of damage can be inferred.

Masri, Nakamura, Chassiakos and Caughey [28] presented a neural network based approach for the detection of changes in the characteristics of structural systems unknown to the NN (i.e. not in training set). Later, Masri, Smyth, Chassiakos, Caughey and

Hunter [29] presented a structural damage detection methodology based on nonlinear system identification approaches. These methods rely on the use of vibration response (accelerations, velocities, and displacements) from a healthy theoretical system to train a feedforward NN for identification purposes. NNs showed to be capable of detecting changes in the physical system with respect to its reference (or undamaged) state.

Another popular approach in nondestructive damage detection is to use spectral analysis. This technique provides a quick and accurate approach in obtaining structural FRFs that may be used to extract parameters [11]. These parameters are then compared with baselines to identify the changes in structural integrity. Spectral analysis can detect location of damage but it does not provide information about the type of damage. The undamaged case data is used to identify the healthy state of the structure. However spectral analysis usually involves a data reduction technique which has a high computational cost.

Zang and Imregun [11] dealt with structural damage detection using measured FRFs as input data to a back propagation ANNs and the output was a prediction of the actual state of the specimen. The methodology was applied to detect three different states of a real space antenna: reference, slight mass damage and slight stiffness damage. The results showed that it was possible to distinguish between the three states of the structure, subject to using a suitable NN configuration. This approach could also be done using FEA.

1.7 Thermal Based Techniques

Stimulated infrared (IR) thermography is a NDE method used for the localization and characterization of thermally resistive defects. In recent years, infrared thermography has gained prominence among the NDE techniques used in detection of defects, particularly for composite structures. This method is based on that in presence of a defect; the surface

temperature evolution is locally modified producing a thermal contrast whose localization allows identifying the damaged area.

Shih, Shin, Delpak, Hu, Plassmann, Wawrzynek and Kogut [30] explored the possibility of detecting geometrical defects in concrete specimens using thermal imaging. The method was based on the characteristics of flow heat phenomenon. They used an IR camera to capture the surface temperature distribution in order to determine the position of the crack and other geometrical imperfections. In this work, the detection process was not automated.

Bai and Wong [31] developed a photo thermal model in order to investigate the behavior of thermal waves in homogeneous plates and layered plates under convective conditions. This model was then utilized to predict the phase differences produced by multi layer subsurface defects. Then the authors used experimental results from lock in thermography to compare with theoretical results obtained by solving numerically.

Plotnikov and Winfree [32] presented comparisons of results from thermal contrast, time derivative and phase analysis methods for defect visualization. These comparisons were based on 3D simulations (finite difference) of a test case representing a plate with multiple delaminations. Comparisons were also based on experimental data obtained from a specimen with flat bottom holes and a composite panel with delaminations. The authors concluded that both thermal contrast and phase thermography are effective methods for defect edge extraction while time derivative is suitable to measure the defect depth.

1.8 Acoustic Emission Based Techniques

The AE technique is a NDE method that permits continuous damage inspection, classification and identification of modes of failure in real time, which is critical for

taking preventive measures. AE techniques detect transient acoustic waves generated by a sudden change in the local stress field in a material. The use of AE in NDT is based upon the fact that crack tips have high stresses and will grow producing AE that can be detected by sensors.

Bakuckas, Prosser and Johnson [33] used the AE technique to locate damage in a titanium matrix composite system based on the arrival times of AE events between two sensors. The authors established correlations between the observed damage growth mechanisms and the AE results in terms of the events amplitude.

Quispitupa, Shafiq, Just and Serrano [34] presented an AE based stiffness reduction model that identifies the extent of damage in sandwich composites subjected to fatigue loading conditions. In this work it was concluded that AE yields very accurate information about the extent and location of damage in various constituents of sandwich composites.

1.9 Other Techniques

In addition to the NDE techniques described above, there are other methods which also provide information used for damage detection purposes. These include: stimulated shearography, the ElectroMagnetic/InfraRed (EMIR) method and electrical impedance.

Shearography

Shearography belongs to speckle interferometry techniques [35]. It consists in illuminating the sample with coherent light and making the reflected wave front interfere with itself, producing a slightly shifted (image “shear”). This interferometry image is registered for two given states of the object to be controlled, first unperturbed, then under a stress produced by a mechanical or thermal excitation. The difference between two interference images gives a pattern representative of the differential displacements of the

surface in the direction of shearing. For NDE purpose, this imaging technique needs to be coupled with a mechanical or thermo mechanical stimulation of the structure, with the damage creating a local perturbation of the displacement field. Figure 2.1 shows typical results corresponding to both thermal and purely mechanical stimulation.

The ElectroMagnetic/InfraRed (EMIR) Method

The principle of the EMIR method is the following [35]: the structure to be tested is illuminated by a microwave electromagnetic (EM) field (X-band). An IR camera observes a photothermal thin film converter, some tens of microns thick, of controlled electrical conductivity, placed in near vicinity of the structure. The image gives directly the space distribution of the electric field intensity in the film plane, allowing visualizing local perturbations in the field due to existing defected areas. Defects can be abnormal structural arrangement and/or abnormal EM properties. One of the advantages of (EMIR) method resides in its sensitivity to the presence of water and/or moisture trapped in the composite material due to the damage. This is of practical use, since water absorption is possible after the damage occurrence, in the field condition. Two different configurations of this method are presented in Figure 2.2 a and b. Detection of water trapped in damaged sandwiches using these configurations is shown in Figure 2.2 c, d, e and f.

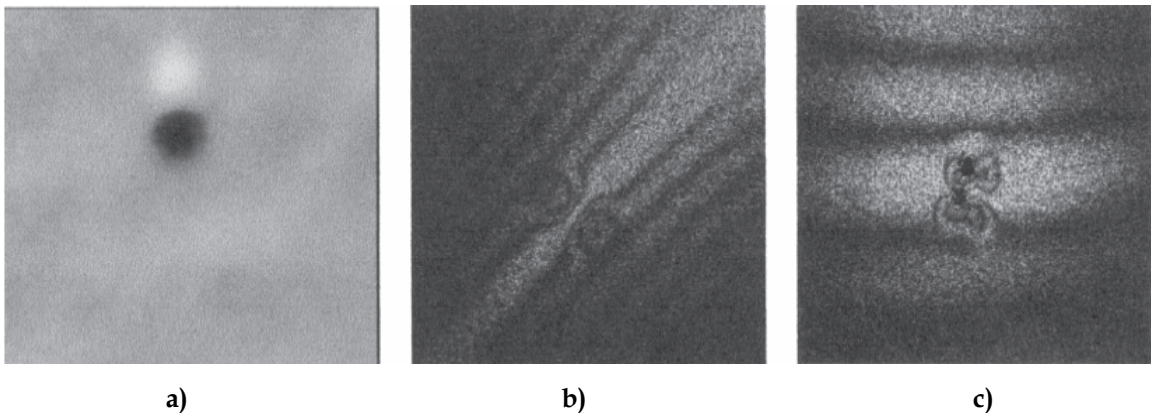


Figure 2.1: Shaerographic images of damages: a) with thermal excitation; b) vibratory excitation; c) idem.

Balageas, Bourasseau, Dupont, Bocherens, Dewynter-Marty and Ferdinand [35] tested the techniques described above in addition with stimulated IR thermography and ultrasonic testing in order to compare their performance when applied to the same sandwich composite specimens. Moreover, they used two integrated HMS based on the one hand on microbending sensitive fibers and Optical Time Domain Reflectometry (OTDR), and on the other hand on Fiber Bragg Grating (FBG) sensors. Their experiments demonstrated that HMS can detect damage with sensitivity comparable to that of the external NDE techniques.

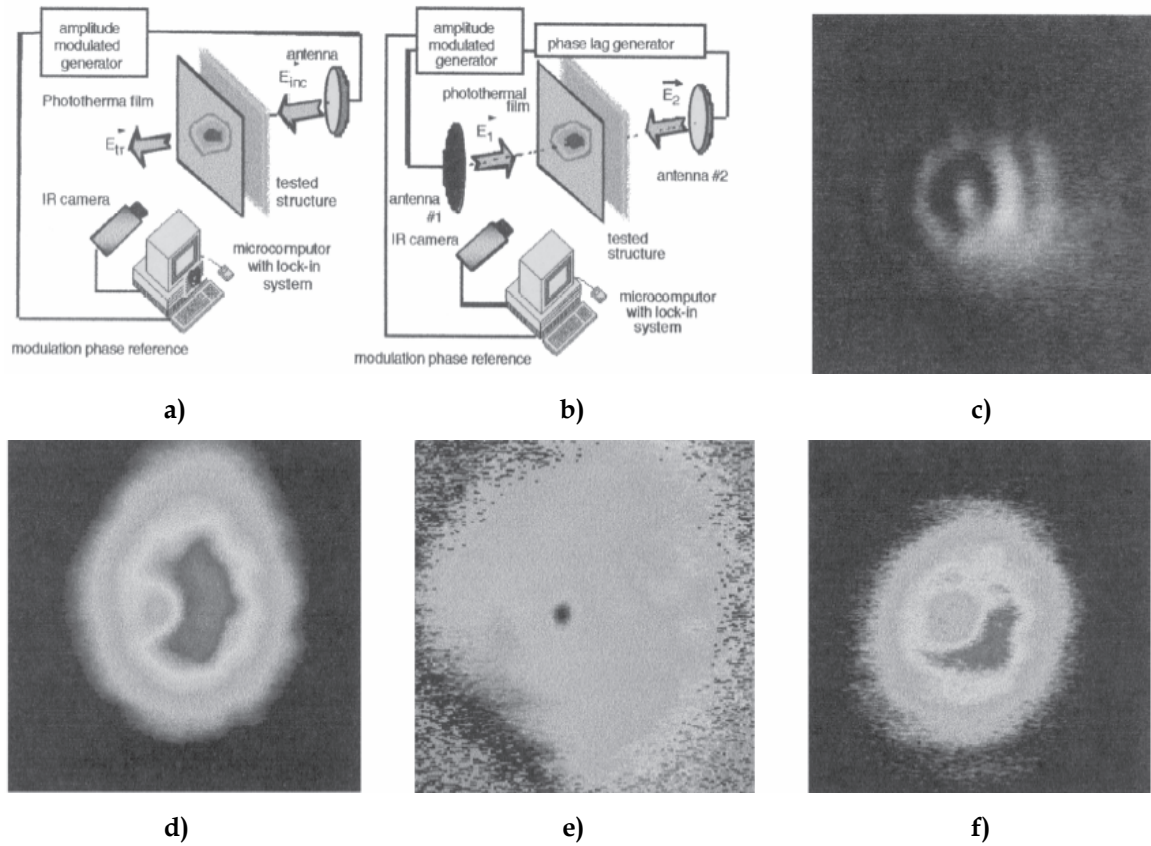


Figure 2.2. EMIR method: a) transmission configuration; b) interferometric configuration; c) detection of water trapped in damaged sandwich; d) idem by interferometric technique: amplitude image; e) idem: phase image; f) idem by transmission technique (amplitude image) .

Electrical Impedance

The fundamental idea is that through applying and monitoring electric signals within an electrically conductive material, the structural condition of it can be determined [36]. In this method an electric current is applied and the electric potential is recorded at monitoring electrodes around the area of study. Damage, in this case, is linked to a reduction in the conductivity as would be appropriate for a tear in an electroactive membrane or fiber breakage in a composite laminate structure.

Anderson, Lemoine and Ambur [36] developed an electric potential based damage detection technique in conjunction with a feedforward back propagation NN inversion scheme to predict damage in electrically conductive composite structures.

According to previous mentioned shearography testing requires a very complex and expensive equipment while EMIR method is only efficient when the damage leads to water or moisture trapping in the structure. On the other hand, electrical impedance scheme is applicable to electrically conductive composite structures. Therefore, we consider that IR thermography and vibrations testing are the most adequate for SHM in sandwich composite structures. The next chapter is based on numerical vibration analysis and we will prove the feasibility of this approach.

Chapter 3

Vibrations Analysis

This chapter focuses on using vibration based analysis to generate features that can be used to predict severity as well as location of damages. More precisely we are interested in the behavior of natural frequencies and mode shapes of the structure. Several damaged scenarios will be created using finite element models. Then, linear modal analysis will be performed and modal parameters will be obtained. Finally, the feasibility of this method in detecting and locating damages will be discussed.

3.1 Vibrations Problem

This section deals with the mathematical formulation of the vibration problem and how the solutions of the equations of motion are related to eigenvalue and eigenvector problems.

3.1.1 Equations of Motion

The equations of motion for a vibrating structure are commonly derived by applying Newton's second law to all of the degrees of freedom (DOFs) of interest. In practice, damping is normally ignored in light weight structures such as sandwich composite panels what does not affect the accuracy of the results.

Assuming negligible damping and assuming that the structure is in free vibrations, a finite set of equilibrium equations are obtained. Expression (3.1) represents a system of second order coupled linear ordinary differential equations, where $[\mathbf{M}]$ and $[\mathbf{K}]$ represent the mass matrix and the stiffness matrix respectively and $\{ \mathbf{U}(\mathbf{t}) \}$ is the nodal displacement vector. $\{ \ddot{\mathbf{U}}(\mathbf{t}) \}$ is the second temporal derivate of $\{ \mathbf{U}(\mathbf{t}) \}$.

$$[\mathbf{M}] \{ \ddot{\mathbf{U}}(\mathbf{t}) \} + [\mathbf{K}] \{ \mathbf{U}(\mathbf{t}) \} = \{ \mathbf{0} \} \quad (3.1)$$

In order to obtain the natural frequencies and mode shapes of the structure, it is not necessary to solve the system of equations (3.1). That means that it is not required to know the displacement vector $\{ \mathbf{U}(\mathbf{t}) \}$ at any time. Instead, we will use a procedure which connects the free vibration problem with eigenvalue problems.

3.1.2 The Eigenvalue Problem

It is well known that the system (3.1) has a solution of the form of simple harmonic motion $\{ \mathbf{U}(\mathbf{t}) \} = \{ \mathbf{u} \} \cdot e^{i\omega t}$ [37], where $\{ \mathbf{u} \}$ is a vector of constants to be determined, ω is a constant to be determined and $i = \sqrt{-1}$. Substituting this solution in equation (1):

$$\{ -\omega^2 \cdot [\mathbf{M}] + [\mathbf{K}] \} \{ \mathbf{u} \} \cdot e^{i\omega t} = \{ \mathbf{0} \} \quad (3.2)$$

Note that the scalar $e^{i\omega t} \neq 0$ for any value of t and hence equation (3.2) yields the fact that ω and $\{ \mathbf{u} \}$ must satisfy the following generalized eigenvalue problem:

$$\{ [\mathbf{K}] - \omega^2 \cdot [\mathbf{M}] \} \{ \mathbf{u} \} = \{ \mathbf{0} \} \quad (3.3)$$

Pre and post multiplying equation (3.3) by the matrix $[\mathbf{M}]^{-1/2}$, we transform the generalized eigenvalue problem into a standard eigenvalue problem:

$$\{ ([\mathbf{M}]^{-1/2} \cdot [\mathbf{K}] \cdot [\mathbf{M}]^{-1/2}) - \omega^2 \cdot [\mathbf{I}] \} \{ \mathbf{u} \} = \{ \mathbf{0} \} \quad (3.4)$$

$$\{ [\mathbf{A}] - \omega^2 \cdot [\mathbf{I}] \} \{ \mathbf{u} \} = \{ \mathbf{0} \} \quad (3.5)$$

In equation (3.5), ω represents the eigenvalue (modal frequency) and $\{ \mathbf{u} \}$ the associated eigenvector (mode shape) of the matrix $[\mathbf{A}]$. If the system being modeled has

n degrees of freedom, the matrices $[\mathbf{M}]$, $[\mathbf{K}]$ and $[\mathbf{A}]$ will have dimension $n \times n$ and the vector $\{ \mathbf{u} \}$ will have n components. Equation (3.5) will produce result n eigenvalues and n eigenvectors.

Various approaches exist to numerically solve eigenvalue problems. These include: QR iteration, Jacobi, Power and the Lanczos methods [38]. In the current work natural frequencies and mode shapes are obtained by performing linear modal analysis using FEMPRO/ALGOR FEA[®] commercial software [39].

3.2 Numerical Model

In model dependent analyses, it is important to have an accurate numerical model before performing experiments. In this section we will use a FE model of a sandwich composite cantilever beam to demonstrate the feasibility of the curvature approach. The model was created according to the test specimen studied later in section 5.2.2 The sandwich beam was conformed by two carbon fiber-epoxy face sheets bonded a by rigid polyurethane foam. The face sheets were made of epoxy matrix reinforced by carbon fibers along longitudinal and transversal directions. The beam dimensions were 23 in length, 2 in width and 0.286 in thick, while the foam core was 0.25 in wide. The model and coordinate system are shown in Figure 3.1.

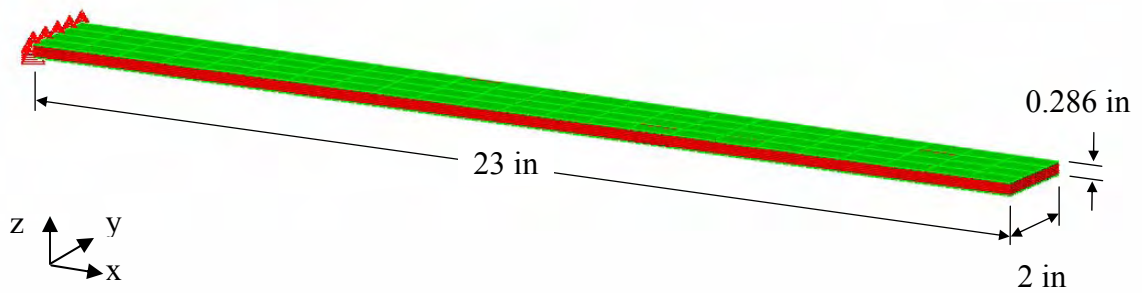


Figure 3.1: FE model and coordinate system.

The FE model of the beam was created in ALGOR[®] FEA commercial software. Two layers of eight nodes “thin composite elements” were used for the face sheets and six layers of eight nodes “brick elements” for the foam core. The cantilever boundary condition was modeled by constraining all degree of freedoms of the nodes located at the root of the beam. For a cantilever beam the vibration mode shapes that can most accurately be measured are flexural mode shapes, therefore we selected as features of study the first three flexural mode shapes and the corresponding natural frequencies.

In order to test the numerical model and check mesh independency, four mesh densities were used for modeling an isotropic aluminum cantilever beam. Aluminum is a well known material and theoretical solutions (natural frequencies and mode shapes) are available in the literature [37]. After performing linear modal analysis for the first three natural frequencies, results obtained from different models were compared to the closed form solutions. Table 3.1 lists the frequencies and the percentage difference between theoretical and finite element analysis (FEA) results. The variation in natural frequencies is less than 2 % between 4 x 23 x 8 and 32 x 184 x 8 mesh densities. Therefore the first model was used for all later simulations due to the computational efficiency.

Table 3.1: First three natural frequencies of an aluminum beam (Hz).

Mode N°	Closed - Form Solution	Elements			
		4 x 23 x 8	8 x 46 x 8	16 x 92 x 8	32 x 184 x 8
1 st	17.600	17.952 (2.00)	17.843 (1.37)	17.794 (1.10)	17.772 (0.97)
2 nd	110.300	112.461 (1.96)	111.734 (1.29)	111.418 (1.01)	111.276 (0.88)
3 rd	308.832	315.785 (2.25)	312.988 (1.34)	311.921 (1.00)	311.473 (0.85)

Since we are interested in flexural mode shapes, only translation degrees of freedom along Z direction were considered in the analysis. Translation along the X and Y axis and rotations are neglected.

3.3 Fitting Model Parameters

To fit the numerical results with further experimental measurements, it is essential to know what values of the parameters required for the FE model best characterize the physical properties of the test specimen. To deal with this problem, we need first to obtain experimental results. The mean square error between numerical frequencies ω^n and measured frequencies ω^e were used to build the objective function to be minimized.

$$\text{objective function} = \left(\frac{\omega_1^e - \omega_1^n}{\omega_1^e} \right)^2 + \left(\frac{\omega_2^e - \omega_2^n}{\omega_2^e} \right)^2 + \left(\frac{\omega_3^e - \omega_3^n}{\omega_3^e} \right)^2 \quad (3.6)$$

As mentioned in the previous section, the numerical model of the sandwich beam was made of eight nodes thin composite elements and eight nodes brick elements. ALGOR[®] FEA requires six elastic properties for the linear thin composite element type and four elastic properties for the linear isotropic brick element type. The elastic constants and the notation followed in this work are shown in Table 3.2 and Table 3.3. Therefore, our objective function is a thirteen variable valued function. In other words, for obtaining a single value of the objective function it must be evaluated in the ten elastic properties and the three experimental modal frequencies.

Table 3.2: Linear thin composite element properties.

Notation	Property
ρ_f	Mass density
E_f^L	Longitudinal modulus of elasticity
E_f^T	Transversal modulus of elasticity
ν_f^{12}	Major Poisson's ratio
ν_f^{21}	Minor Poisson's ratio
G_f	Shear modulus of elasticity

Table 3.3: Linear isotropic brick element properties.

Notation	Property
ρ_c	Mass density
E_c	Modulus of elasticity
ν_c	Poisson's ratio
G_c	Shear modulus of elasticity

The experimental frequencies listed in Table 3.4 were available from the test later described in section 5.2.1. The numerical frequencies are not sensitive to all the variables in the same way. A simple sensitivity study showed that only six of the ten elastic properties are significant for the objective function. Figure 3.2 and Figure 3.3 show the behavior of the objective function with respect to the model parameters. The variables E_f^T , ν_f^{12} , ν_f^{21} and ν_c do not modify significantly the objective function, therefore they can be ignored in the optimization process.

Table 3.4: Experimental natural frequencies.

Mode N°	Natural Frequency [Hz]
1 st	25.625
2 nd	134.062
3 rd	314.062

Thus, the original thirteen variable valued objective function (3.7) was reduced to a six variable valued function (3.8):

$$\textit{original objective function} = f(\rho_f, E_f^L, E_f^T, \nu_f^{12}, \nu_f^{21}, G_f, \rho_c, E_c, \nu_c, G_c, \omega_1^e, \omega_2^e, \omega_3^e) \quad (3.7)$$

$$\textit{reduced objective function} = f(\rho_f, E_f^L, G_f, \rho_c, E_c, G_c) \quad (3.8)$$

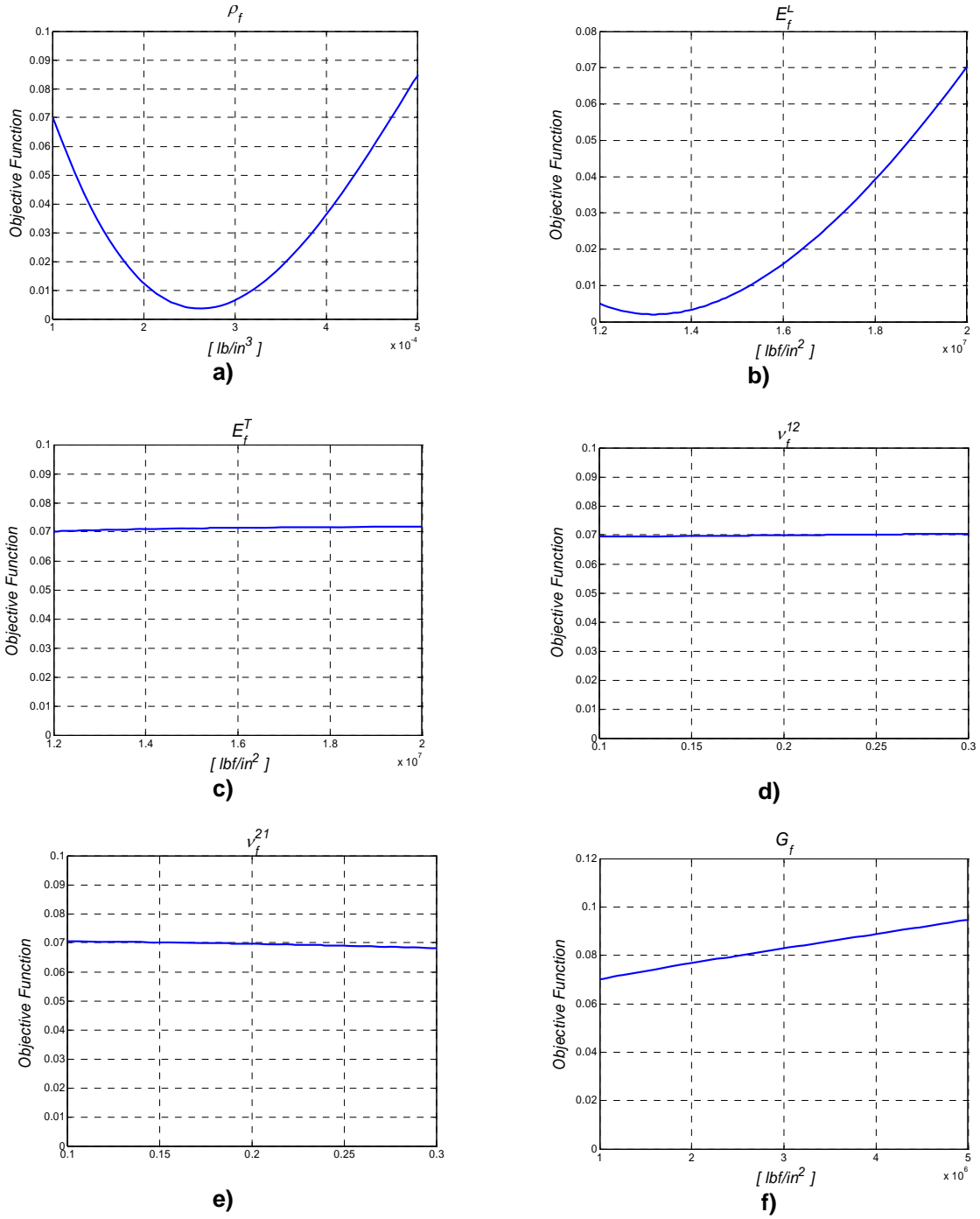


Figure 3.2: Variation of the objective function with respect to the face sheet parameters a) mass density; b) longitudinal modulus of elasticity; c) transversal modulus of elasticity; d) mayor poisson ratio; e) minor poisson ratio; f) shear modulus of elasticity.

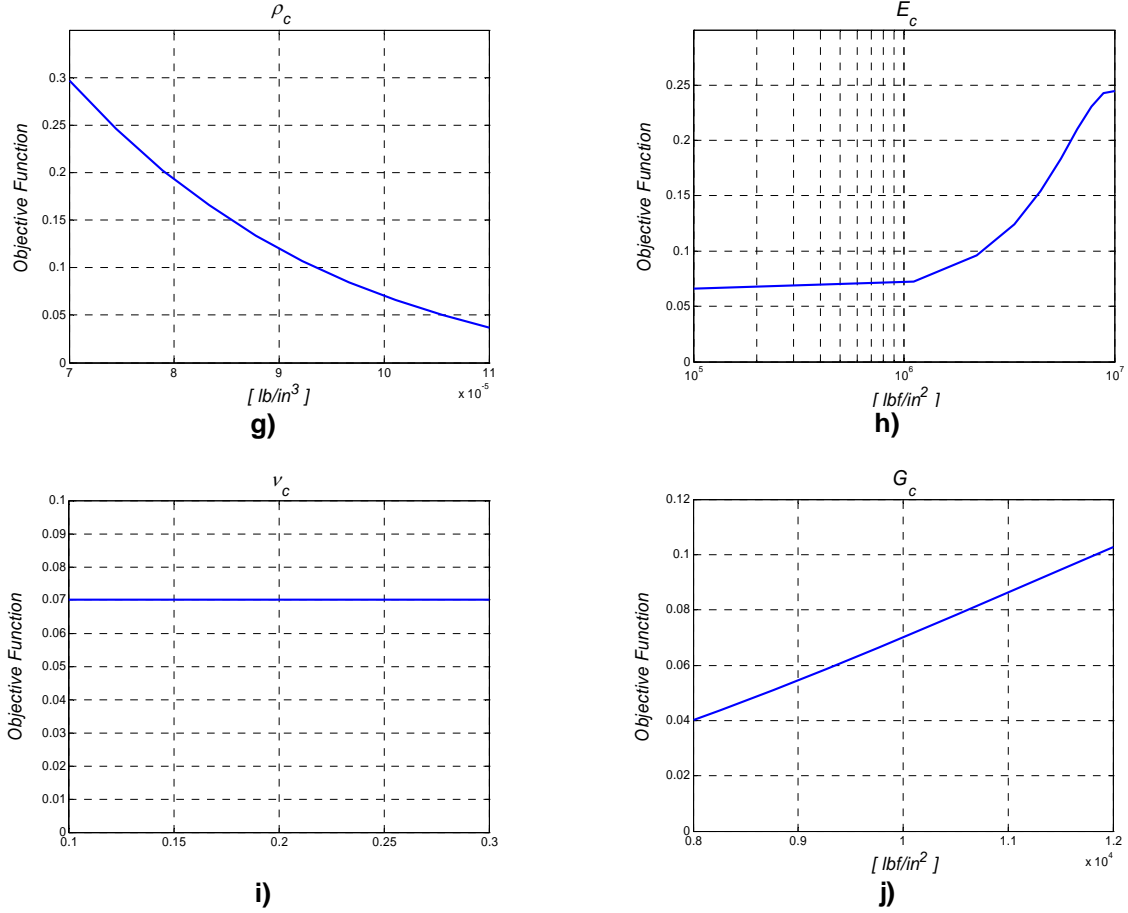


Figure 3.3: Variation of the objective function with respect to the foam core g) mass density; h) modulus of elasticity; i) poisson ratio; j) shear modulus of elasticity.

Since an analytical expression for the objective function (f) in terms of the elastic properties was not available and we only had some discrete values of this function, it was necessary to apply an interpolation technique. The method chosen to optimize the reduced objective function was the quadratic interpolation method [65]. This procedure is based on selecting three values for the first variable ($\rho_f^1, \rho_f^2, \rho_f^3$) while keeping the remaining variables fixed ($E_f^L, G_f, \rho_c, E_c, G_c$) and evaluating the function f at those points (equations (3.9)). Then, a second order polynomial $h_1(\rho_f)$ is used to approximate the objective function at those values and a local minimum (ρ_f^*) of $h_1(\rho_f)$ is found.

$$\begin{aligned}
&f(\rho_f^1, E_f^L, G_f, \rho_c, E_c, G_c) \\
&f(\rho_f^2, E_f^L, G_f, \rho_c, E_c, G_c) \\
&f(\rho_f^3, E_f^L, G_f, \rho_c, E_c, G_c)
\end{aligned} \tag{3.9}$$

Later, setting the value ρ_f^* for the variable ρ_f and selecting three values for the second variable $(E_f^{L1}, E_f^{L2}, E_f^{L3})$, three new values of the objective function are obtained:

$$\begin{aligned}
&f(\rho_f^*, E_f^{L1}, G_f, \rho_c, E_c, G_c) \\
&f(\rho_f^*, E_f^{L2}, G_f, \rho_c, E_c, G_c) \\
&f(\rho_f^*, E_f^{L3}, G_f, \rho_c, E_c, G_c)
\end{aligned} \tag{3.10}$$

A new second order polynomial $h_2(E_f^L)$ is used to fit the function f at those points and a local minimum, E_f^{L*} , of this polynomial is found. Figure 3.4 depicts the optimization method for the first two variables ρ_f and E_f^L .

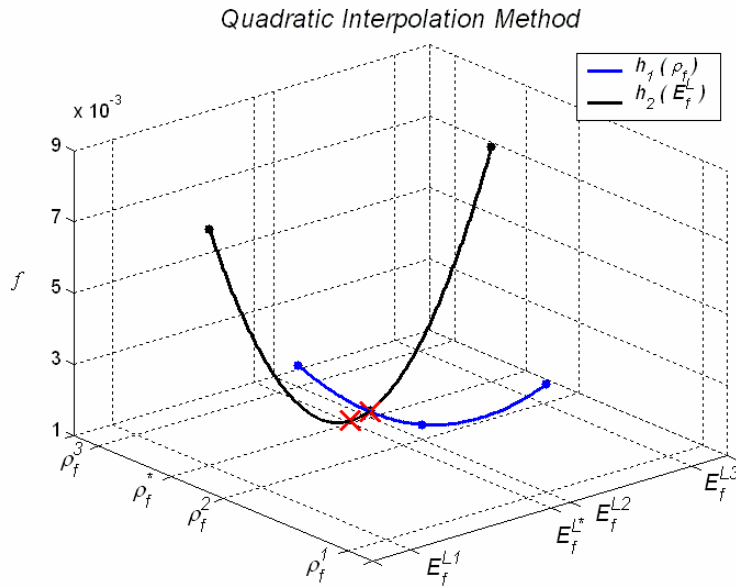


Figure 3.4.

This procedure is repeated for all the variables until a satisfactory value of objective function is reached. Each time the six variables of f are updated, an iteration of the optimization method is completed.

Note that initial values for the six elastic constants $(\rho_f, E_f^L, G_f, \rho_c, E_c, G_c)$ are required in order to start the optimization method. The further these values are from the optimum, the greater the number of iterations that are needed by the method to converge to a solution. As a starting point, typical elastic property values for materials used in sandwich composite panels [41] were used as input parameters to the numerical model.

Two complete iterations were necessary to obtain a satisfactory level of accuracy in the numerical results. However the procedure was not stopped until five iterations to check the stability of the solution. Convergence of the method is shown in Figure 3.5. The final elastic properties of the FE model listed in Table 3.5 lead to the value 1.178×10^{-3} for the objective function.

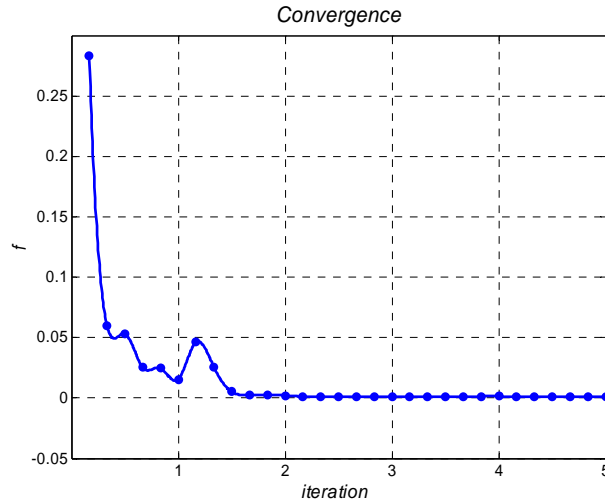


Figure 3.5.

Because of the fiber orientation in the face sheets, mechanical properties of this material are equal along both longitudinal and transversal directions. In addition, the

foam core longitudinal modulus of elasticity is negligible compared with the face sheet modulus of elasticity.

Table 3.5: Elastic properties used in the FE model.

Property	Face Sheet	Foam Core
Mass density (lb/in ³)	1.97×10^{-4}	1.56×10^{-5}
Longitudinal modulus of elasticity (lbf/in ²)	8.13×10^6	1×10^2
Transversal modulus of elasticity (lbf/in ²)	8.13×10^6	—
Major Poisson's ratio	0.3	0.3
Minor Poisson's ratio	0.3	—
Shear modulus of elasticity (lbf/in ²)	9×10^4	5.6×10^3

Setting the above elastic constants for the finite element model, the first three natural frequencies were calculated and compared with those obtained experimentally in section 5.2.3. Table 3.6 indicates that the maximum difference between numerical and experimental results was less than 3 %.

Table 3.6: Natural frequencies of the intact FE beam.

Mode N°	Experimental Results	Finite Element Results
1 st	25.625	24.903 (2.81)
2 nd	134.062	134.668 (0.45)
3 rd	314.062	318.859 (1.52)

According to the level of accuracy obtained with this model, elastic properties listed in Table 5 will be used for all later finite element simulations. Moreover, section 5.2.3 shows the close agreement between numerical mode shapes and curvature mode shapes measured in the modal testing.

3.4 Curvature Finite Difference Approximation

Localized changes in stiffness result in a mode shape that has a localized change in slope, therefore, this feature will be studied as a possible candidate for damage detection purposes. For a beam in bending the curvature (κ) can be approximated by the second derivate of the deflection:

$$\kappa = \frac{d^2 z}{dx^2} \quad (3.11)$$

In addition, numerical and experimental mode shape data is discrete in space, thus the change in slope at each node can be estimated using finite difference approximations. In this work the central difference equation was used to approximate the second derivate of the displacements \mathbf{u} along the X direction at node i :

$$\kappa_i = \frac{z_{i-1} - 2 \cdot z_i + z_{i+1}}{h^2} \quad (3.12)$$

The term $h = z_i - z_{i-1}$ is the element length. In this process meshing and node numbering is very important. Equation (3.12) require the knowledge of the displacements at node i , node $i - 1$ and node $i + 1$ in order to evaluate the curvature at node i . Thus, the value of the curvature of the mode shapes could be calculated starting from node 2 thru node 23. After obtaining the curvature mode shapes the absolute difference between the undamaged and damaged state is determined to improve damage detection

$$\Delta(\kappa_i) = \left| \kappa_i \Big|_{No\ Damage} - \kappa_i \Big|_{With\ Damage} \right| \quad (3.13)$$

As a result of this analysis, a set of curvature vectors for different damage localizations are obtained. These vectors will be used as input data to train the neural network. A neural network is employed to make pattern recognition and to classify further numerical (FEA) results and experimental vibration measurements.

3.5 Undamaged Case

By using the same finite element model presented in section 3.3, linear mode shapes and natural frequencies analysis was performed in ALGOR[®] FEA. The numerical results were exported to MATLAB[®] [41] to be processed. The first three natural frequencies of the intact cantilever beam were listed previously in Table 3.6.

The associated mode shapes were sketched evaluating the displacements in Z direction of the 24 equidistant nodes located at the centerline of the beam as shown in Figure 3.6. In order to unify the results from the different cases, mode shapes were normalized by setting the largest grid point displacement equal to 1.

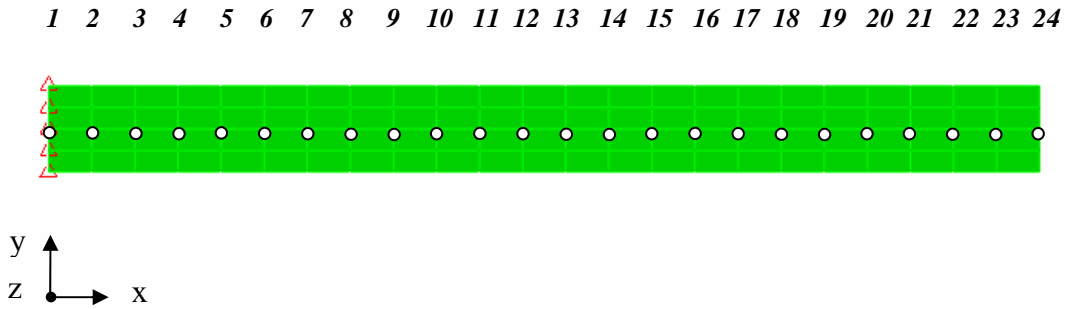


Figure 3.6: Node location in the FE model.

Figure 3.7 shows the first three mode shapes for the intact cantilever beam. The curvature mode shapes were calculated from the displacements mode shapes by applying the central difference approximation for the second derivate. The first three curvature mode shapes are shown in Figure 3.8.

It can be noticed from these figures that all the mode shapes and curvature mode shapes are smoothed functions, what indicate the absence of damages. Undamaged curvature mode shapes will be used to compare further results. Since changes in the curvature are local in nature, they can be used to detect and locate damages in the beam.

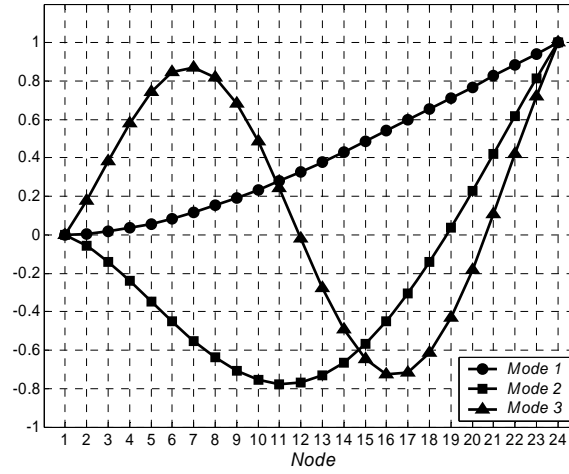


Figure 3.7: Mode shapes - Intact beam.

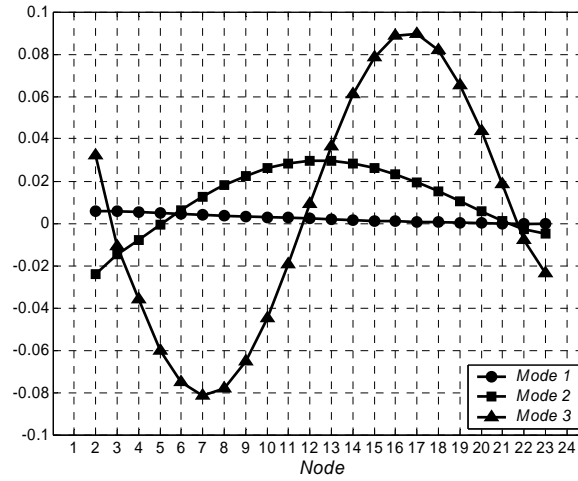


Figure 3.8: Curvature mode shapes - Intact beam.

3.6 Damaged Case

Structural damage was modeled as a local separation between the face sheet and the foam core. A 1 in x 2 in bond failure was created in the FE model by having a region where elements were not connected to each other. Five different locations were selected along the beam span for setting the damages. These locations are between node 3 - 4, node 5 - 6, node 9 - 10, node 16 - 17 and node 20 - 21. The dimensions used to model the

failure were kept constant during the analyses. The damage scenarios were studied individually and then some combined cases were studied.

3.6.1 Simple Damage Scenarios

The first scenario selected for studying the effect of a localized damage in the beam is shown in Figure 3.9. As in the previous section, linear mode shapes and natural frequency analysis was performed using ALGOR FEA[®]. The elastic properties of the materials are the same as that for the undamaged beam and remain constant for all the cases.

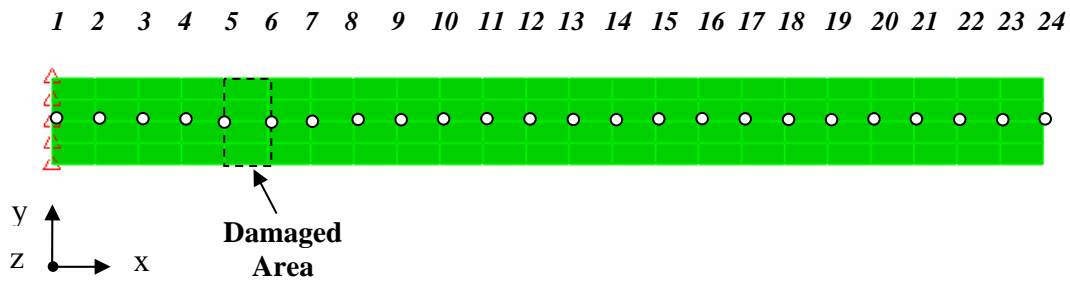


Figure 3.9: FEM of damage case 2.

The first three natural frequencies of the damaged cantilever beam (case 2) are listed in Table 3.7. Since the damage produced a localized reduction in stiffness, the natural frequencies have decreased compared to those corresponding to the intact beam (Table 3.6). The associated mode shapes and curvature mode shapes are shown in Figure 3.10 and Figure 3.11.

Table 3.7: Frequencies of the damaged FE beam.

Mode N ^o	Natural Frequency [Hz]
1 st	24.547
2 nd	122.079
3 rd	303.989

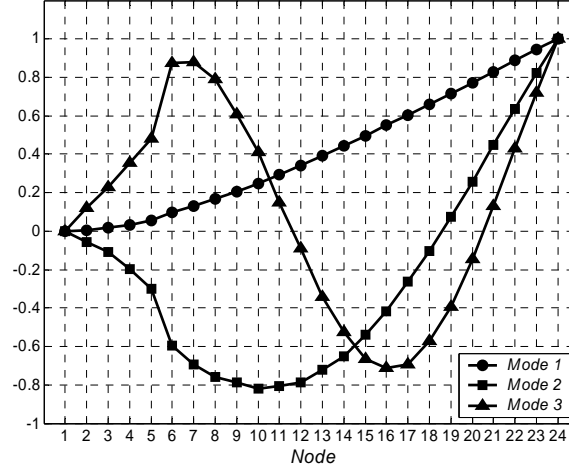


Figure 3.10: Mode shapes - Damage case 2.

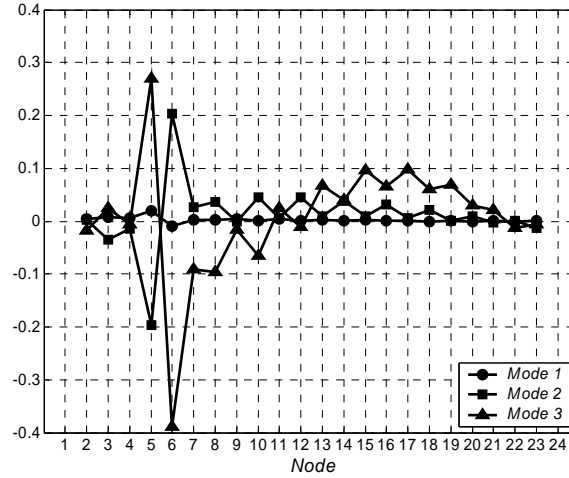


Figure 3.11: Curvature mode shapes - Damage case 2.

From these figures, it can be seen that both mode shapes and curvature mode shapes suffer significant irregularities which are more marked in the damaged area. In section 3.7 the selection of the difference in curvature mode shapes as feature for damage detection and location is justified. Figure 3.12 shows the absolute difference in curvature between the intact beam and the damaged beam. This feature also was normalized by setting the largest value equal to 1.

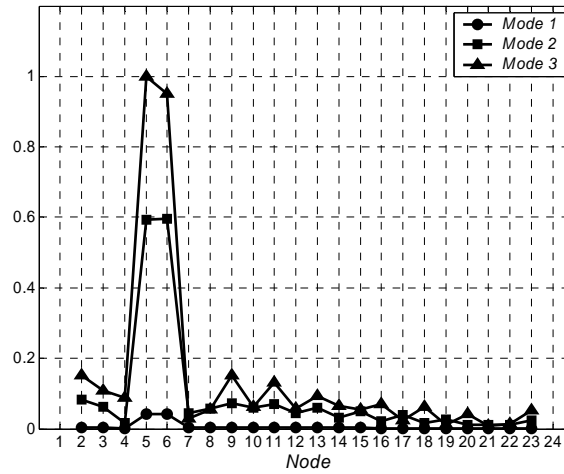


Figure 3.12: Difference in curvature - Damage case 2.

The maximum difference value for each curvature mode shape occurs in the damage location, which was placed between node 5 and node 6. In other areas of the beam this characteristic was much smaller. Although the third mode shapes was the most sensitive to the failure it is important that the three curvature mode shapes peak at the damaged location. The same analysis was performed for the other damage cases and analogous results were obtained. Natural frequencies are all listed in Table 3.8. Although the reduction in natural frequencies is related to the existence of damage and its severity, this feature can not provide any useful information about the location of the damage. Thus, this modal parameter will not be considered in the following cases. Curvature mode shapes were calculated and compared with the undamaged case (Figures 3.13-3.16).

Table 3.8: Natural frequencies for different damage locations (Hz).

Mode N ^o	Damage Case				
	1) Node 3 - 4	2) Node 5 - 6	3) Node 9 - 10	4) Node 16 -17	5) Node 20 - 21
1 st	24.558	24.547	24.559	24.731	24.885
2 nd	119.547	122.079	130.546	130.949	129.549
3 rd	279.013	303.989	295.377	318.483	286.192

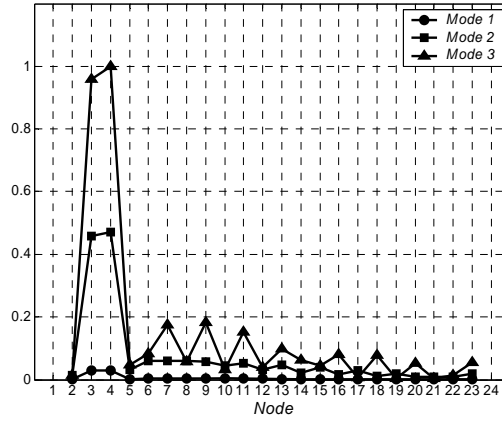


Figure 3.13: Difference in curvature - Damage case 1.

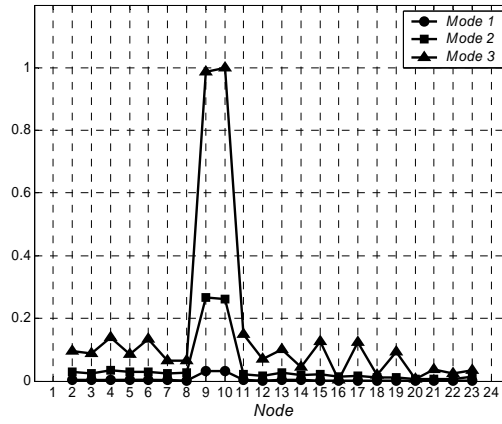


Figure 3.14: Difference in curvature - Damage case 3.

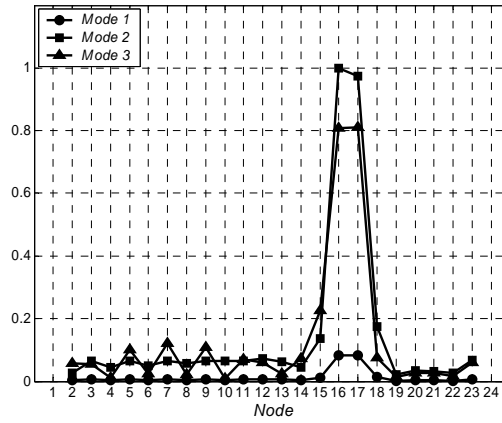


Figure 3.15: Difference in curvature - Damage case 4.

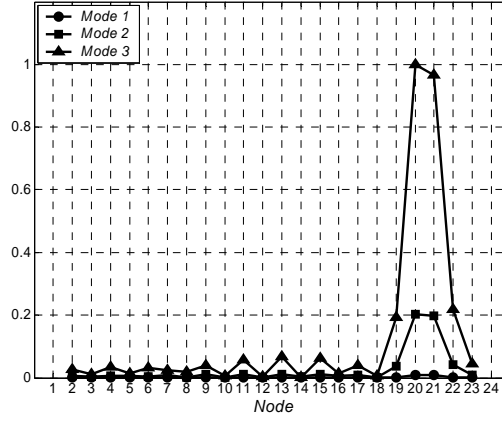


Figure 3.16: Difference in curvature - Damage case 5.

Each plot shows a peak at the damage location; therefore this feature successfully identified the position of the damage along the length of the beam. Always the third mode shape was the most sensitive to the damage except in damage case 4 where the second mode shape better identified the failure. In chapter 6, differences in curvature mode shapes will be used as input patterns to the neural network and the corresponding damage position as its associated target in the training procedure for further case classification.

3.6.2 Multiple Damages Scenarios

In order to investigate the behavior of curvature mode shapes when multiple damages are present in the beam, the same analysis was performed for a beam containing simultaneously two of the previous damage scenarios.

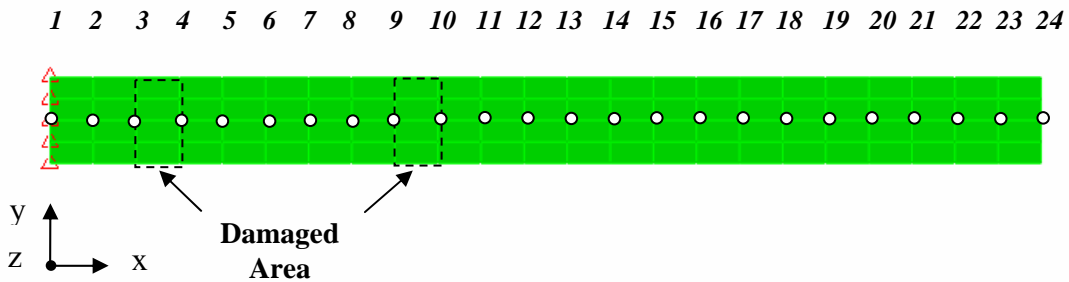


Figure 3.17: FE model of multiple damages (case 6).

The first of the multiple damage scenarios was a combination of damage case 1 and damage case 3 as shown in Figure 3.17. Curvature mode shapes were calculated for this multiply damaged beam and compared with those from the intact beam. The results are plotted in Figure 3.18.

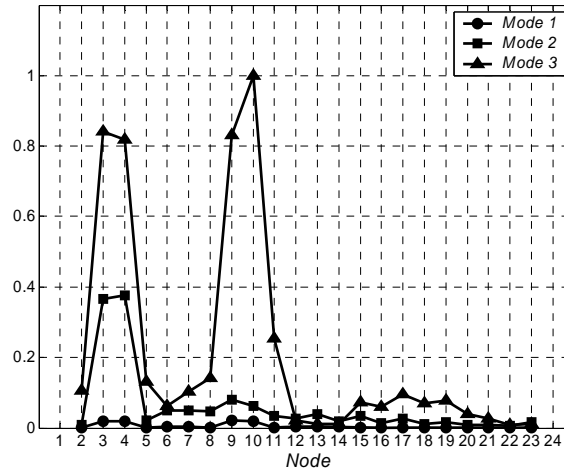


Figure 3.18: Difference in curvature - Damage case 6.

The second of the multiple damage scenarios was a combination of damage case 2 and damage case 4 as shown in Figure 3.19. The results are plotted in Figure 3.20.

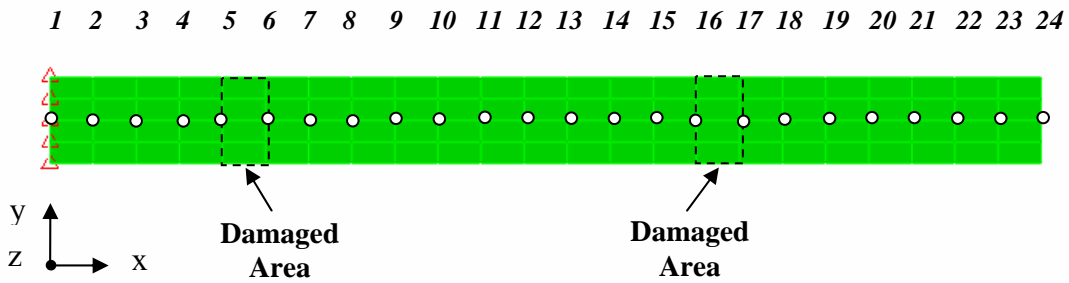


Figure 3.19: FE model of damage case 7.

According to the previous results, the proposed approach not only successfully located the damage for single cases but also for multiple damage scenarios.

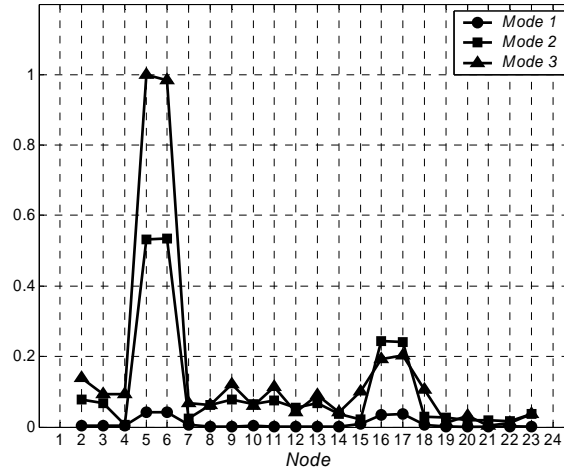


Figure 3.20: Difference in curvature - Damage case 7.

This particular characteristic makes this procedure suitable for real application where, in most cases, structures may contain several defects at the same time.

3.7 Scope of the Method

This section focuses on the limitations of the damage detection curvature approach. Different damage sizes and location were studied. First, a 0.75 in x 0.0625 in x 0.018 in surface crack was modeled between node 11 and node 12. Figure 3.21 shows the damage location. The mode shapes and curvature mode shapes are plotted in Figure 3.22 and Figure 3.23 respectively.

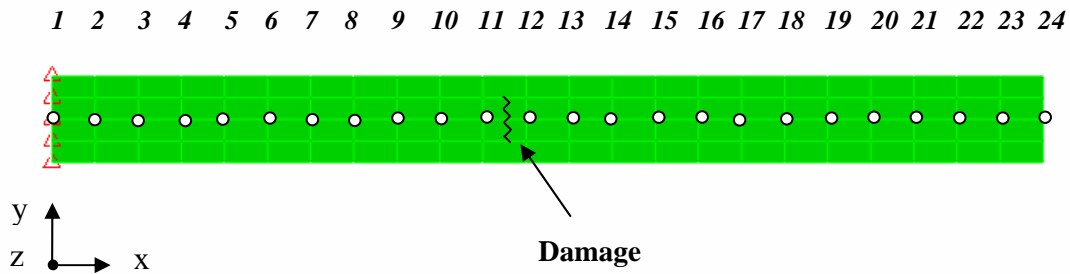


Figure 3.21: FE model of damage case 8.

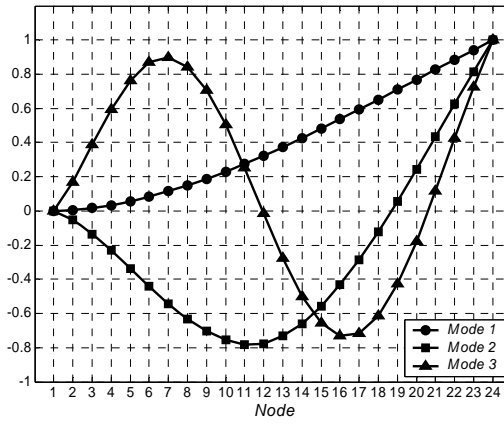


Figure 3.22: Mode shapes - Damage case 8.

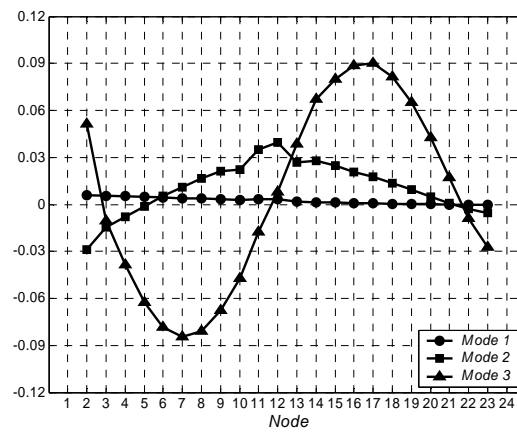


Figure 3.23: Curvature mode shapes - Damage case 8.

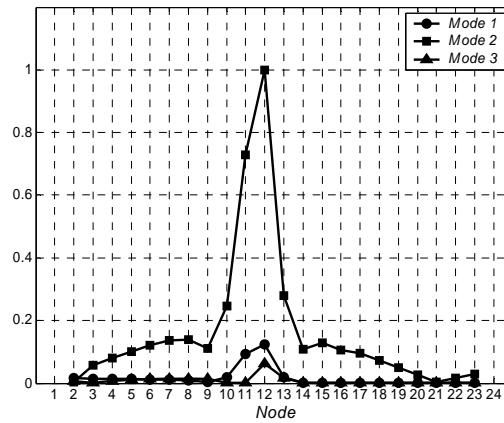


Figure 3.24: Difference in curvature - Damage case 8.

This damage scenario was not detected using the natural mode shapes because they did not significantly change from the undamaged mode shapes. A small peak can be observed in the second curvature mode shape. Performing the difference between curvature mode shapes, Figure 3.24 is obtained. Although the second curvature mode shape was the most sensitive to the crack, the three curves show peaks between node 11 and node 12. This damage case validates the selection of the curvature approach for damage detection reasons.

Finally, a damage scenario consisting in a 0.0625 in diameter and 0.018 in depth indentation introduced between node 10 and node 11 on the surface of the sandwich beam model. Differences in curvature mode shapes were calculated and plotted in Figure 3.26.

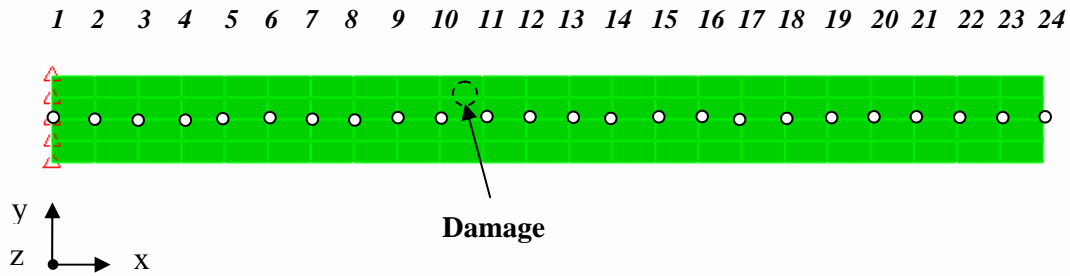


Figure 3.25: FE model of damage Case 9.

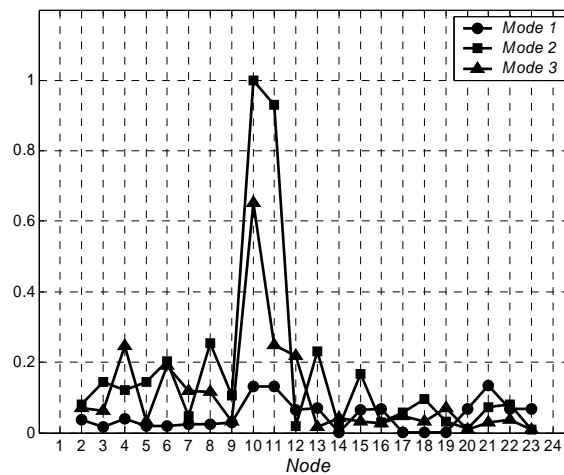


Figure 3.26: Difference in curvature - Damage case 9.

This case shows that curvature approach may mask the damage location when it does not severely reduce the stiffness of the structure. The first curvature mode shape was unable to predict the defect location. Another example is the damage scenario shown in Figure 3.27 whose curvature data is plotted in Figure 3.28.

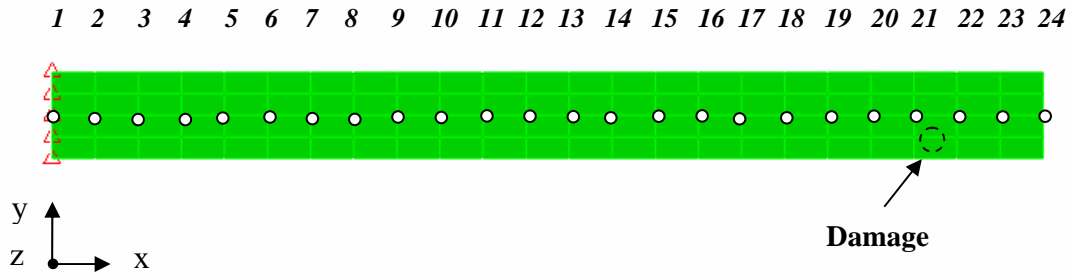


Figure 3.27: FE model of damage Case 10.

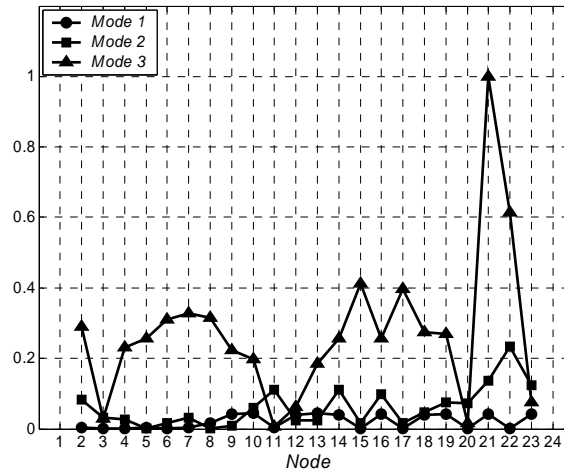


Figure 3.28: Difference in curvature - Damage case 10.

These situations could be classified erroneously by the neural network. Therefore, in the next chapter thermal transient analysis is considered as an alternative method of damage characterization that complements the curvature method.

Chapter 4

Thermal Analysis

In this chapter the transient thermal response of a sandwich composite structure is studied. The mathematical formulation of the problem is presented. Then, a numerical approximation technique is used to solve the governing equations. The thermal distribution on the surface of the model is analyzed when damages are introduced. Finally, the feasibility of this feature being used for damage detection is discussed.

4.1 Heat Transfer Problem

The analysis consists in the acquisition of external surface temperature data from a numerical model in response to a thermal transient excitation induced by external heating and exposed to free convection condition. This method is based on the fact that in presence of a defect; the surface temperature evolution is locally modified producing a thermal contrast whose localization allows identifying the damaged area.

4.1.1 Problem Formulation

The governing partial difference equation that models the temperature distribution is the three dimensional transient heat conduction equation [42,43]:

$$\rho \cdot c_p \cdot \frac{\partial T}{\partial t} = \frac{\partial}{\partial x} \left(k \cdot \frac{\partial T}{\partial x} \right) + \frac{\partial}{\partial y} \left(k \cdot \frac{\partial T}{\partial y} \right) + \frac{\partial}{\partial z} \left(k \cdot \frac{\partial T}{\partial z} \right) \quad (4.1)$$

The terms T , ρ , k and c in equation (1) represent temperature, mass density, thermal conductivity and specific heat capacity respectively, (x, y, z) are the spatial coordinates and t is the time. To solve this equation, it is necessary to use a set of initial and boundary

conditions. In particular, one initial condition in time and two boundary conditions in space are used. To simplify the notation, we rename the coordinates $\mathbf{x} = (x, y, z) = (x_1, x_2, x_3)$.

Initial conditions:

$$\begin{aligned} T_{x_i}^0 &= \tilde{T}^0 & x_i &\in \tilde{\Gamma} \\ T_{x_i}^0 &= T^0 & x_i &\in \Gamma \end{aligned} \quad (4.2)$$

\tilde{T}^0 and T^0 are initial temperature values for points placed in the regions $\tilde{\Gamma}$ and Γ of the domain of equation (4.1)

Boundary conditions:

$$k \cdot \frac{\partial T}{\partial x_i} \Big|_{x_i=0} = h \cdot (T_0 - T_\infty) \quad k \cdot \frac{\partial T}{\partial x_i} \Big|_{x_i=Lx_i} = h \cdot (T_{Lx_i} - T_\infty) \quad (4.3)$$

In the above equation h represents the convection heat transfer coefficient, T_∞ is the ambient temperature and Lx_i is the model length in x_i direction. The coefficient h for the vertical face was approximated by using the correlation for a vertical plate. This correlation is formulated in terms of non dimensional numbers [43]. The first of them is the Nusselt number defined as:

$$Nu = \frac{h Lx_2}{k_a} = CRa^n \quad (4.4)$$

In equation (4.4), k_a represents the thermal conductivity of the air, Lx_2 is the height of the plate, and C and n are constant that depend on the Raleigh number Ra . In this case, it is recommended [43] to use $C = 1.02$ and $n = 0.148$.

The Raleigh number Ra is defined as:

$$Ra = \frac{g\beta(T_s - T_\infty) Lx_2^3}{\nu_a \alpha_a} \quad (4.5)$$

The term g is the gravity constant, T_s is the surface temperature where h is evaluated, T_∞ is the temperature of the air far way from the beam, ν_a is the viscosity of air, and α_a is the diffusivity of the air. The term β is the volumetric thermal expansion, which is approximated by:

$$\beta = \frac{1}{T_{film}} \quad (4.6)$$

$$T_{film} = \frac{T_s + T_\infty}{2} \quad (4.7)$$

The temperatures T_s and T_∞ are in Kelvin. Figure 4.1 shows the convection heat transfer coefficient used in the numerical simulation.

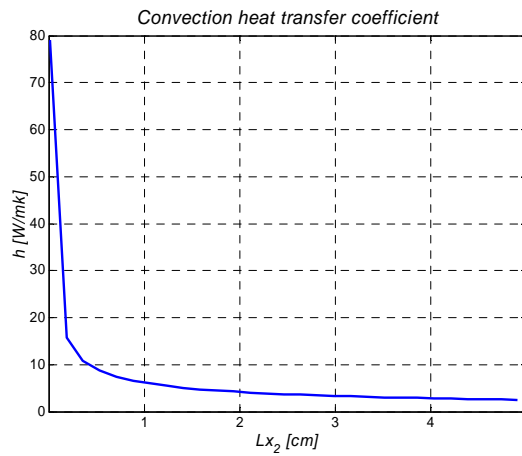


Figure 4.1.

Several numerical methods are available to solve equation (4.1). These include FEA, the finite difference (FD) method, finite volume (FV) method, among others. An algorithm that allows the handling of parameters defined above was required. The FV code was selected in order to obtain the numerical solution of the thermal problem [44,45,46]. This technique involves integrating the differential equation into a control volume. The integration process is done around a nodal point P . Its neighboring nodal points are called E and W (east and west) in x_1 direction, N and S (north and south) in x_2 direction and T and B (top and bottom) in x_3 direction. According to the notation used in the literature, capital letters indicate the nodal point while small letters refer to the boundary of the control volume around the point P .

To show how this technique works, we approximate equation (4.1) along x_1 direction. The first step in FV technique is to divide the original domain into discrete control volumes. The simplest case of control volume is a cube centered in each nodal point.

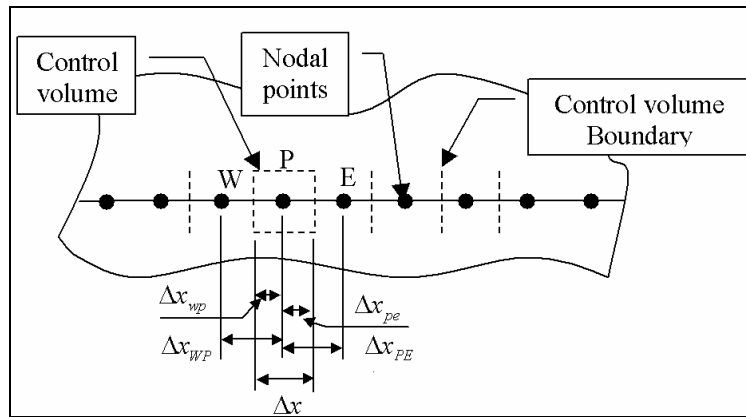


Figure 4.2: 1D FV model.

Figure 4.2 describes the 1D model of FV. Then, the x_1 dimensional version of equation (4.1) is integrated over the domain of the control volume (Ω):

$$\int_{\Omega} \left(\frac{\partial}{\partial x_1} \left(k \cdot \frac{\partial T}{\partial x_1} \right) - \rho \cdot c_p \cdot \frac{\partial T}{\partial t} \right) d\Omega = 0 \quad (4.8)$$

$d\Omega = dx_1 \cdot dx_2 \cdot dx_3$. Solving equation (4.8):

$$\left(k \cdot A \cdot \frac{\partial T}{\partial x_1} \right) \Big|_e - \left(k \cdot A \cdot \frac{\partial T}{\partial x_1} \right) \Big|_w - \rho \cdot c_p \cdot \Delta x_1 \cdot A \cdot \frac{\partial T}{\partial t} = 0 \quad (4.9)$$

In equation (4.9), A represents the cross sectional area and Δx_1 is the dimension along x_1 axis of the control volume. The flux terms are approximated by:

$$\left(k \cdot A \cdot \frac{\partial T}{\partial x_1} \right) \Big|_e = k \cdot A \cdot \left(\frac{T_{x_{1E}} - T_{x_{1P}}}{\Delta x_{1EP}} \right) \quad (4.10)$$

$$\left(k \cdot A \cdot \frac{\partial T}{\partial x_1} \right) \Big|_w = k \cdot A \cdot \left(\frac{T_{x_{1P}} - T_{x_{1W}}}{\Delta x_{1PW}} \right) \quad (4.11)$$

Where Δx_{1EP} is the length between x_{1E} and x_{1P} , Δx_{1PW} is the length between x_{1W} and x_{1P} , and $T_{x_{1E}}$, $T_{x_{1W}}$, $T_{x_{1P}}$ are the temperatures of the nodal point E , W and P respectively. Substituting equations (4.10) and (4.11) into equation (4.9):

$$k \cdot A \cdot \left(\frac{T_{x_{1E}} - T_{x_{1P}}}{\Delta x_{1EP}} \right) - k \cdot A \cdot \left(\frac{T_{x_{1P}} - T_{x_{1W}}}{\Delta x_{1PW}} \right) - \rho \cdot c_p \cdot \Delta x_1 \cdot A \cdot \frac{\partial T}{\partial t} = 0 \quad (4.12)$$

Rewriting the above equation:

$$\left(\frac{T_{x_{1E}} - T_{x_{1P}}}{\Delta x_{1EP}} \right) - \left(\frac{T_{x_{1P}} - T_{x_{1W}}}{\Delta x_{1PW}} \right) = \frac{\rho \cdot c_p}{k} \cdot \Delta x_1 \cdot \frac{\partial T}{\partial t} \quad (4.13)$$

Regrouping terms:

$$\alpha \cdot \Delta x_1 \cdot \frac{\partial T}{\partial t} = a_E \cdot T_{x_{1E}} + a_W \cdot T_{x_{1W}} - a_P \cdot T_{x_{1P}} \quad (4.14)$$

In equation (4.14), α is the thermal diffusivity. The coefficients are defined as:

$$\begin{aligned} a_E &= \frac{1}{\Delta x_{1EP}} \\ a_W &= \frac{1}{\Delta x_{1PW}} \\ a_P &= a_W + a_E \end{aligned} \quad (4.15)$$

In addition, equation (4.14) must be integrated in time. A fully implicit scheme was used to solve the integration. This method approximates the time derivate by using equation (4.16) with a Δt time step.

$$\frac{\partial T}{\partial t} = \frac{T^{t+\Delta t} + T^t}{\Delta t} \quad (4.16)$$

Equation (4.14) takes the form:

$$\alpha \cdot \Delta x_1 \cdot \left(\frac{T^{t+\Delta t} + T^t}{\Delta t} \right) \Bigg|_{x_{1P}} = a_E \cdot T_{x_{1E}}^{t+\Delta t} + a_W \cdot T_{x_{1W}}^{t+\Delta t} - a_P \cdot T_{x_{1P}}^{t+\Delta t} \quad (4.17)$$

Rewriting equation (4.17):

$$(a_P + a_0) \cdot T_{x_{1P}}^{t+\Delta t} = a_E \cdot T_{x_{1E}}^{t+\Delta t} + a_W \cdot T_{x_{1W}}^{t+\Delta t} - a_0 \cdot T_{x_{1P}}^t \quad (4.18)$$

Where:

$$a_0 = \frac{\alpha \cdot \Delta x_1}{\Delta t} \quad (4.19)$$

The iterative method (4.18) starts at the initial temperature values given by equations (4.2). The matrix form of equation (4.18) is:

$$[A] \{\tilde{T}\} = \{\tilde{B}\} \quad (4.20)$$

Where $[A]$ is the matrix of coefficients $\{\tilde{T}\}$ is the vector of the unknown temperatures and $\{\tilde{B}\}$ is a vector computed from the right hand side of equation (4.18). The vector $\{\tilde{B}\}$ contains all known values obtained from the initial condition, the previous time step or the boundary conditions.

To solve the system (4.20) the Conjugated Gradient Stabilized (CGSTAB) algorithm [38] was written in a FORTRAN [47] code. The block diagram of the code is shown in Figure 4.3. The main program **trans3d** uses five subroutines. The first of them is the subroutine **init** which reads the data of the problem: initial conditions, dimensions, and so forth. Then the 3D mesh is generated by the subroutine **gridgen**. The assembly of the matrix $[A]$ is done by **calct** which uses the subroutine **bct** to set the boundary conditions. The subroutine **cgstab3d** solves the linear system (4.20) using the CGSTAB algorithm. Finally the subroutine **tecplot** prints the results in the TECPLOT[®] [48] file format.

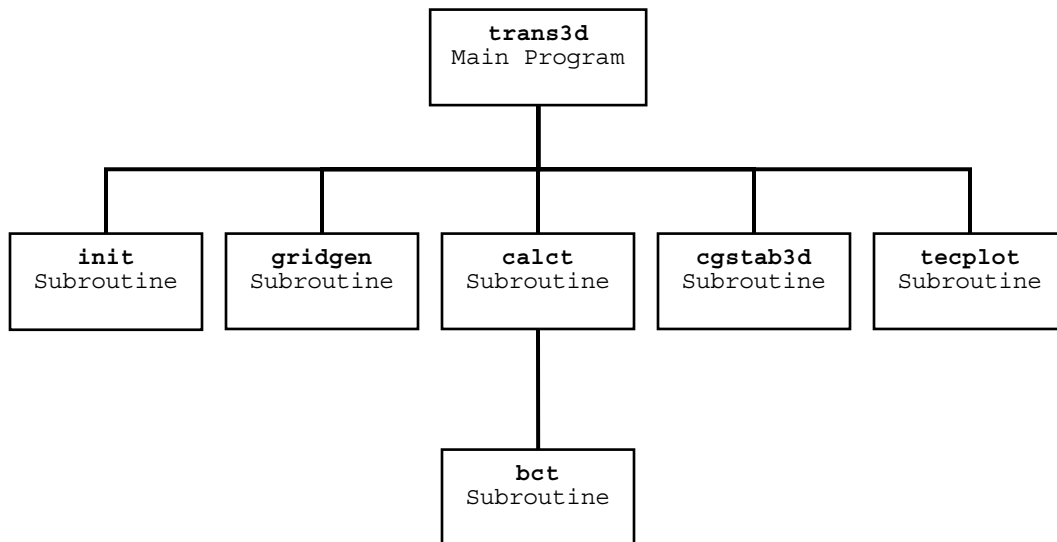


Figure 4.3: Block diagram of CGSTAB code.

TECPLOT[®] was used to generate a set of images (bitmaps) of the surface temperature distribution as a function of time. These images are related to a particular damage case. Later, the bitmaps will be converted to numerical data to train a neural network. As in the vibration approach, this neural network will be employed to make pattern recognition and to classify measured thermal data for damage detection.

4.2 Numerical Model

As mentioned previously the temperature distribution on the test specimen was predicted using the FV method. This numerical solution provided a basis for the required temperature range and sensitivity of the infrared imager that was used in the experimental application. The FV model was a 6 in x 2 in x 0.286 in sandwich composite. This model was created by using a 96 x 29 x 20 nodes grid. It gave a spatial resolution of a 0.0625 in x 0.069 in on the $x_1 - x_2$ plane (Figure 4.4). Three different thermal properties were set in the x_3 direction corresponding to the materials of the sandwich.

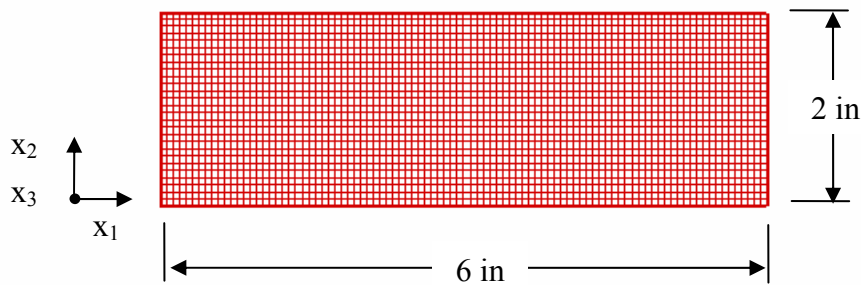


Figure 4.4: 3D FV mesh.

The defects were represented as inclusions of a material with thermal properties different from that of the composite material. Air properties were used to represent material defects. Free convection losses from the beam surface were considered. The thermal properties of the sandwich and defects do not vary with temperature. An instant surface heating was modeled by setting \tilde{T}^0 and T^0 as initial temperatures in the regions

$\tilde{\Gamma}$ and Γ respectively (Figure 4.5). The transient thermal distribution of the model is directly related to the heated area $\tilde{\Gamma}$. The parameters required for this model are listed in Table 4.1.

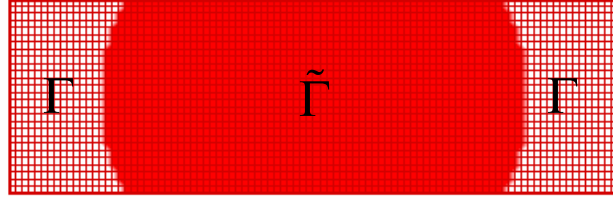


Figure 4.5: Initial temperature distribution.

Table 4.1: FV model parameters.

Parameter	Value
Spatial resolution $\Delta x_1, \Delta x_2, \Delta x_3$ [cm]	1.58, 1.75, 0.036
Time step Δt [sec]	0.01
Initial temperature \tilde{T}^0 [K, °C]	353.15, 80
Initial temperature T^0 [K, °C]	298.15, 25
Ambient temperature T_∞ [K, °C]	298.15, 25
Face sheet material thermal diffusivity α_f [sec/cm]	0.062
Foam core material thermal diffusivity α_c [sec/cm]	0.22
Damage thermal diffusivity α_d [sec/cm]	0.22
Convection coefficient h [W/cm K]	Figure 4.1

The solution of this model allows obtaining a temperature value at each node of the grid for a moment in time from initial to infinity with a defined time step. The first 60 seconds of the transient thermal response of the sandwich composite are represented in a sequence of 12 images. This sequence is similar to one received from an infrared camera, except it is free from noise, optical distortions and inhomogeneous heating. Image processing techniques will be applied to this ideal temperature response in order to study scope of the proposed thermal NDE.

4.3 Undamaged Case

The normal thermal response of the sandwich composite was simulated using the FV model described in the previous section. The model parameters values were set according to Table 4.1. The study was limited to a 4 in x 2 in centered area. The temperature range selected was 25 °C - 28 °C using a scale of 16 colors. The surface temperature distribution was plotted every 5 seconds during an interval of 60 seconds (Figure 4.6). The isotherms have elliptical shapes shifted from the center. This effect is associated with the variation of the convection coefficient h along x_2 direction (Figure 4.1) and it will be present when the face sheet is placed vertically. No shifting due to convection will be present if the face sheet is horizontal. Any irregularity can be observed from this sequence of images.

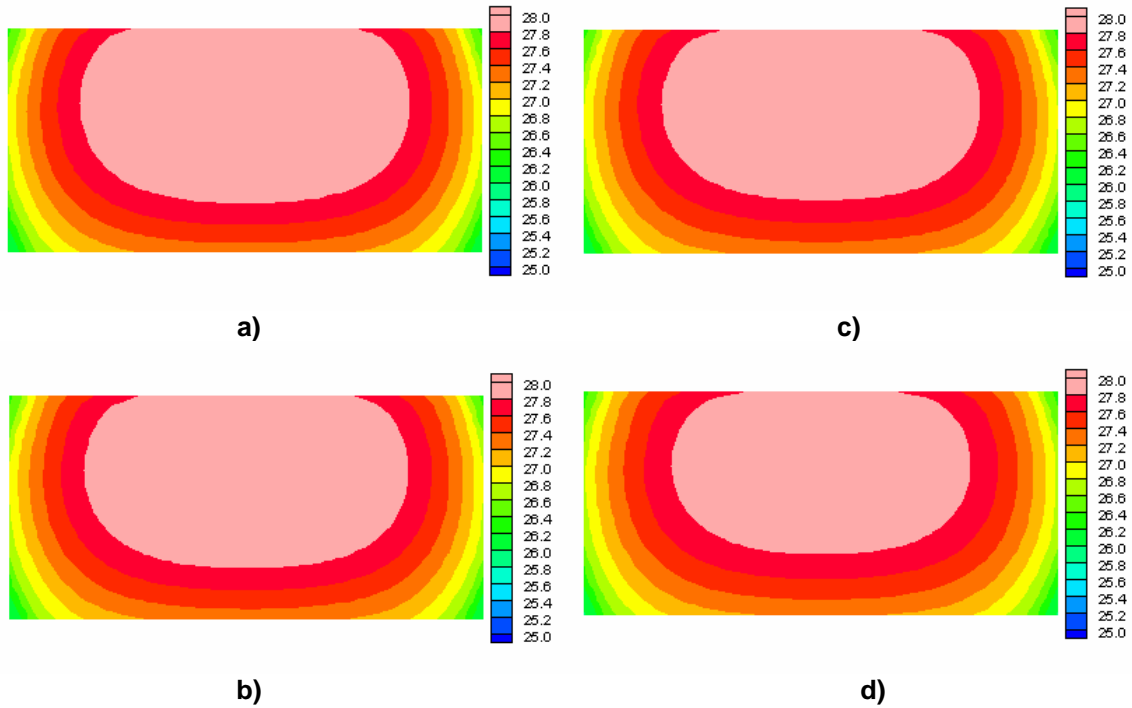


Figure 4.6. Undamaged case: a) 5 sec.; b) 10 sec.; c) 15 sec.; d) 20 sec.

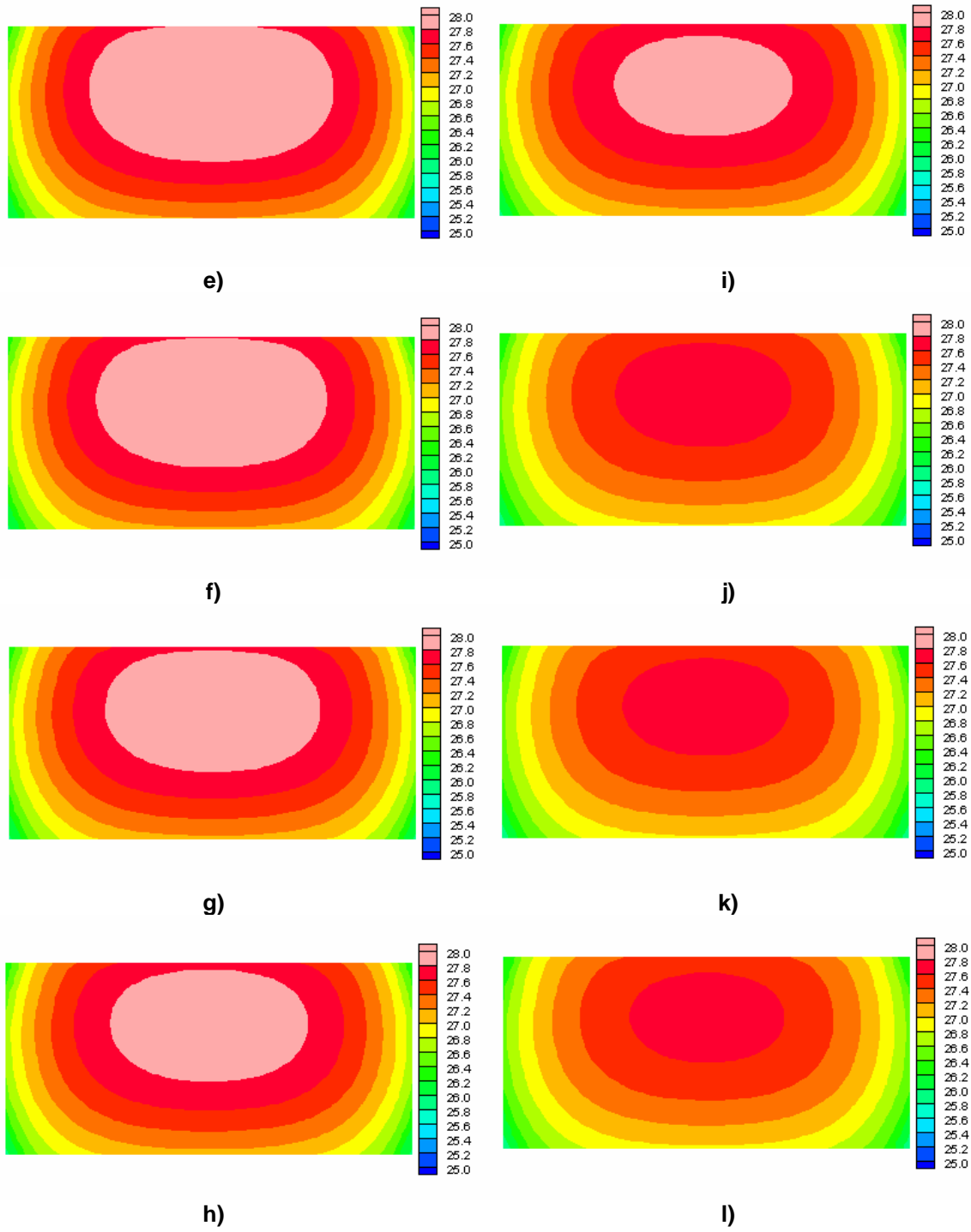


Figure 4.6. Undamaged case: e) 25 sec.; f) 30 sec.; g) 35 sec.; h) 40 sec.; i) 45 sec.; j) 50 sec.; k) 55 sec.; l) 60sec.

4.4 Damaged Case

4.4.1 Simple Damage Scenarios

In order to study the thermal distribution around a surface defect, a 1/16 in diameter indentation was modeled. The depth of this damage is equal to the face sheet thickness. As mentioned in the previous section, the thermal diffusivity of the defect is much less than the face sheet diffusivity. Thus, while the temperature on the surface of the model decreases, the defect location appears visible as a hot spot. For all the damage cases studied in this section, we will only show the most relevant images. These images represent the success of the thermal analysis in detecting the damage location. In Figure 4.7 a and b a hot spot can be clearly visualized while in Figure 4.7 c and d the damage is less noticeable.

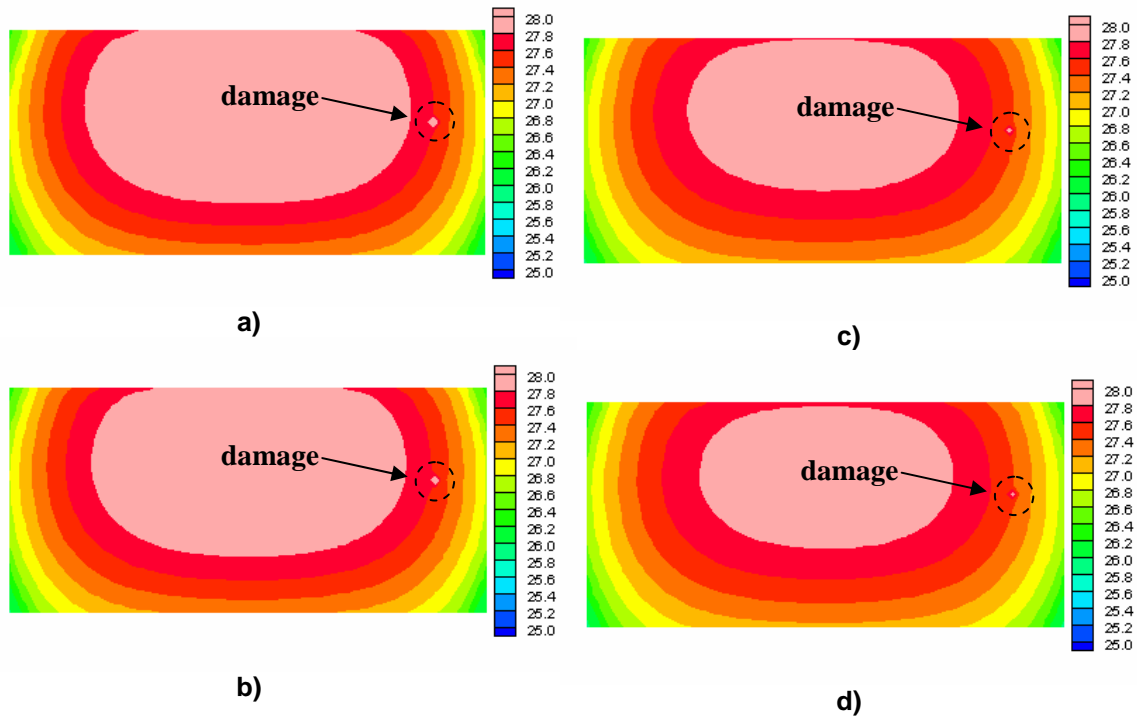


Figure 4.7. Damage case 1: a) 10 sec.; b) 15 sec.; c) 30 sec.; d) 35 sec.

The relative position of the damage respect to the heated zone is the factor that determines the time at which the damage can be identified. The location and size of the damage can be extracted from an image using edge extraction techniques. These features will be used later to characterize each damage case (section 6.4).

The next damage scenario includes the same type of damage studied in the previous case but with different location. The simulated defect was placed near to the heating focus. Two thermal images were able to locate the damage. Figure 4.8 correspond to 50 and 55 seconds of transient thermal response of the model respectively. Because of its position, the defect was not detected until the last seconds of the interval of study. A small hot spot can be seen inside the red area.

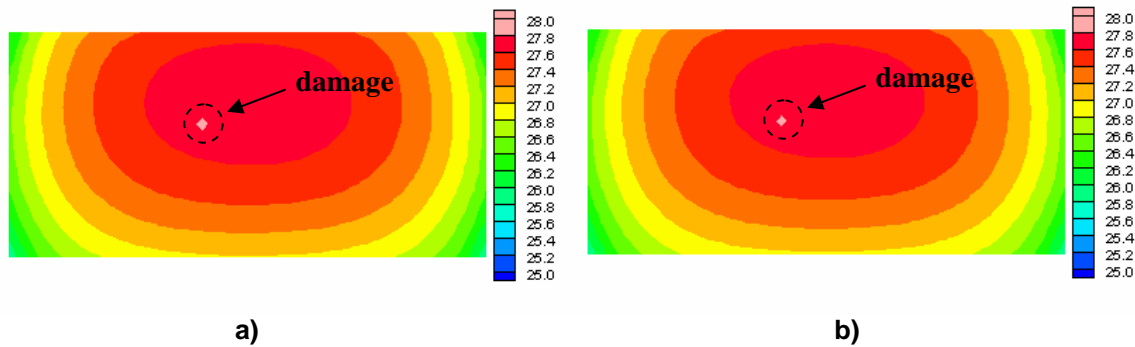


Figure 4.8. Damage case 2: a) 50 sec.; b) 55 sec.

The next damage case consists of a 1/8 in diameter notch through the face sheet of the sandwich composite. Size of the damage is an important factor when locating it. The bigger the size, the longer the period of time that the defect is visible. The numerical solution was plotted at 5, 10, 30 and 35 seconds in Figure 4.9. Note that in all the cases studied until now, the temperature distribution changed only in the vicinity of the damage. Far away from this area the thermal response remained unperturbed. Thus most of the information contained in each image is not required for damage detection.

Therefore, features extraction techniques are required in order to reduce the amount of data and retain the relevant information.

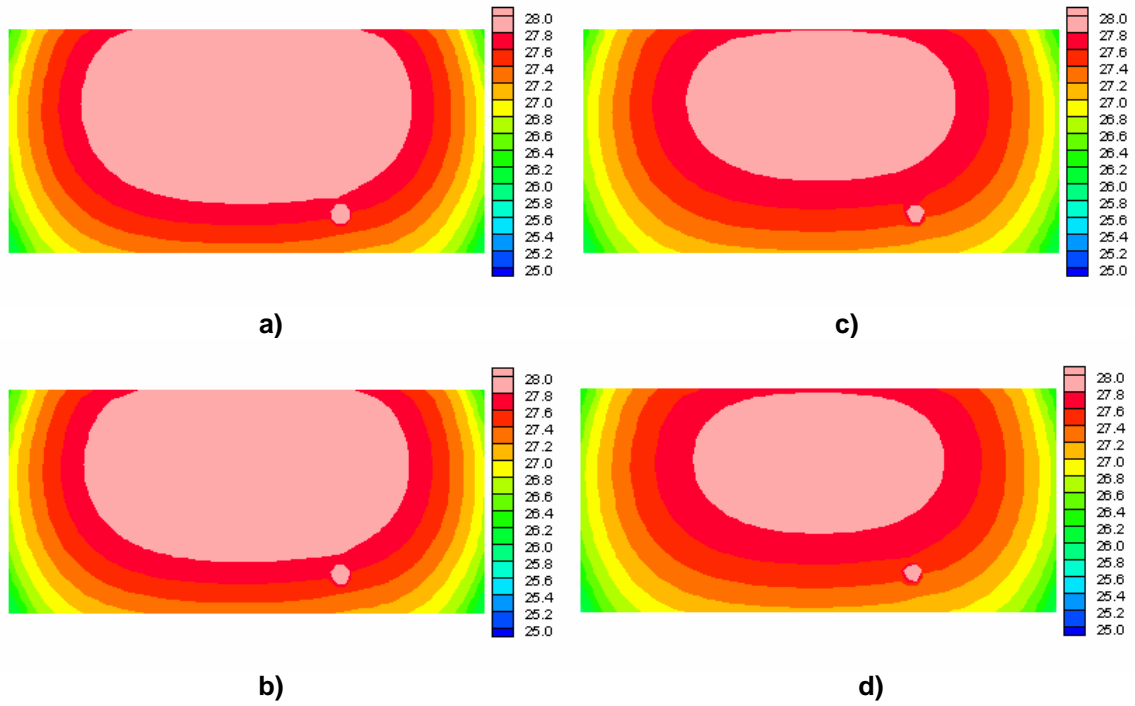


Figure 4.9. Damage case 3: a) 5 sec.; b) 15 sec.; c) 30 sec.; d) 35 sec.

A 3/8 in surface crack was created in the FV model by connecting consecutive damaged elements. The thermal response at 50 and 55 seconds is shown in Figure 4.10.

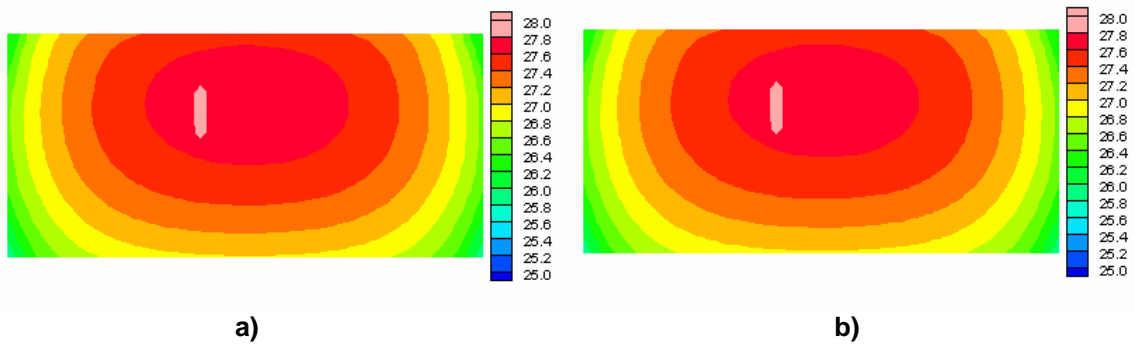


Figure 4.10. Damage case 4: a) 50 sec.; b) 55 sec.

4.4.2 Multiple Damage Scenarios

Multiple damage states may be common in sandwich composite structures. The thermal technique presented here is especially suitable for these cases. The same concepts and conclusions for a single damage state apply when several damages occur in the material. The feature extraction method, which will be described in Chapter 6, identifies each hot spot in an image and then classifies it according to a data base of known damage cases. Figure 4.11 a and b show the FV solution at 15 and 20 seconds respectively. In both images two hot spots can be distinguished.

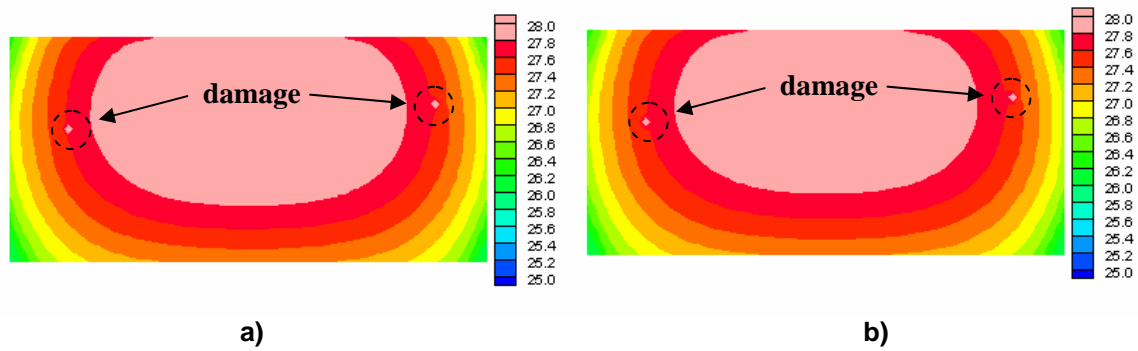


Figure 4.11. Damage case 5: a) 15 sec.; b) 20 sec

4.5 Scope of the Method

Note that all the damage cases analyzed in this chapter included surface failures. This is the principal limitation of thermal transient analysis. Because of the thermal distribution only changes in the vicinity of the damage, this technique is unable to detect subsurface defects. This conclusion will be demonstrated by experimental results in Chapter 5. However thermal response showed to be suitable to identify small surface defects which were almost undetectable by the curvature approach studied in Chapter 4. These two techniques complement each other and will be used together in order to improve the damage detection capability.

Chapter 5

Experimental Validation

5.1 Introduction

The purpose of experiments is to acquire real information about the behavior of the specimen under study in response to an external excitation (thermal or vibration) and to validate the numerical results. Validation of the numerical models is crucial as they are the source of the data used in the damage detection process. As previously mentioned, two non destructive evaluation methods will be studied. Modal testing will be performed in order to obtain the dynamic properties of the structure (natural frequencies and mode shapes) and IR thermography will provide necessary information about the surface temperature distribution over the beam. Several damages scenarios will be tested by both techniques with the purpose of determining the limitations of each method. The obtained experimental data will be used for training and simulating an ANN in order to identify and locate the damage.

5.2 Modal Testing

In modal testing, Frequency Response Function (FRF) measurements are usually made under controlled conditions, where the test structure is artificially excited. The FRF is a fundamental measurement that isolates the inherent dynamic properties (frequencies and mode shapes) of a mechanical structure [49]. The FRF describes the input output relationship between two degrees of freedom (DOFs) on a structure as a function of frequency. In Figure 5.1 the output of the mechanical system $X(\omega)$ is related to the input $F(\omega)$ through the factor $H(\omega)$. A brief look at the mathematical representation of the

dynamics of a structure reveals that FRFs can be completely represented in terms of modal parameters [50].

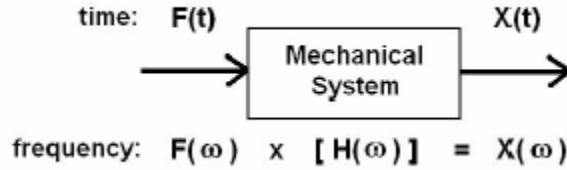


Figure 5.1: FRF $H(\omega)$ definition.

The equations of motion for a vibrating structure are commonly derived by applying Newton's second law to all of the DOFs of interest in the structure. In an experimental situation, this results in a finite set of equations, one for each measured DOF:

$$[M]\{\ddot{X}(t)\} + [K]\{X(t)\} = \{F(t)\} \quad (5.1)$$

The excitation forces and responses are functions of time t , and the coefficient matrices $[M]$ and $[K]$ are constants. This dynamic model describes the vibration response of a linear, time invariant structure. If initial conditions are ignored, the equivalent frequency domain form of the dynamic model can be represented in terms of discrete Fourier Transform (FT) [50]:

$$\{X(\omega)\} = [H(\omega)]\{F(\omega)\} \quad (5.2)$$

This equation is a definition of the FRF matrix. It also indicates that FRF ($H(\omega)$) is defined [49] as the ratio of the FT of an output response ($X(\omega)$) divided by the FT of the input force ($F(\omega)$) that caused the output. An FRF is a complex valued function of frequency and can be displayed in various formats as shown in Figure 5.2. In this chapter, the Bode representation will be used to plot the measured FRFs. Figure 5.3 is a typical plot of the Log Magnitude of an FRF measurement (solid curve), but several resonance curves are also plotted as dotted lines.

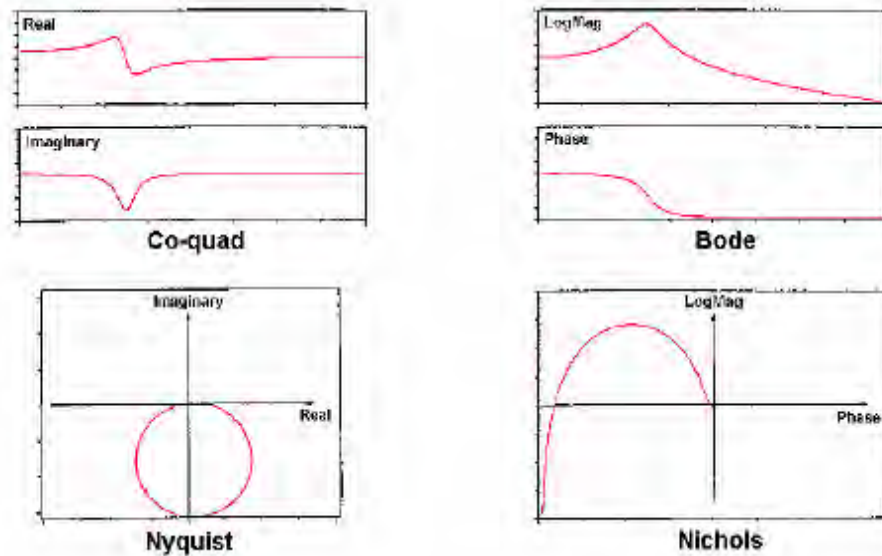


Figure 5.2: Typical FRF plots.

Each of these resonance curves (dotted lines) is the structural response due to a single mode of vibration. The overall structural response is in fact, the summation of resonance curves. In other words, the overall response of a structure at any frequency is a summation of responses due to each of its modes. It is also evident that close to the frequency of one of the resonance peaks, the response of one mode will dominate the frequency response [49]. The frequency of a resonance peak in the FRF is used as the modal frequency. This peak frequency is not exactly equal to the modal frequency but is a close approximation, especially for lightly damped structures.

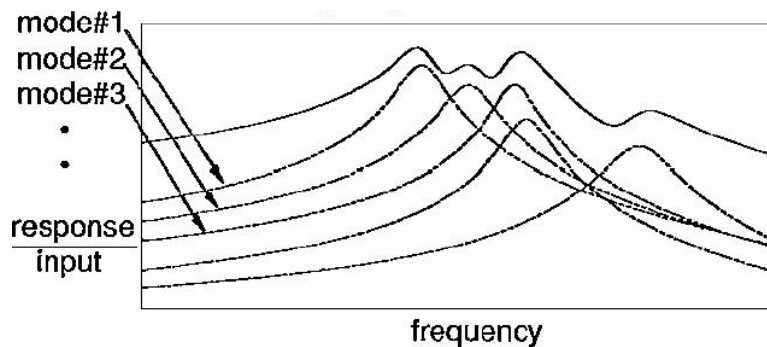


Figure 5.3: Log magnitude of an FRF.

To properly identify a resonant peak two characteristics must be present: the magnitude of the FRF must be at a local maximum and a phase shift of approximately $n\pi$ degrees must occur. On the other hand, mode shapes can be obtained by applying well known curve fitting methods [49]. However, in the current work mode shapes are found by exciting the structure at each one of the peak frequencies and measuring the response (displacements) at several points of the structure. Thus, experimental modal parameters (frequencies and mode shapes) are obtained from a set of FRF measurements.

5.2.1 Test Specimens

Several sandwich composite beams were used as specimens for experimental testing. The samples are made of two carbon fiber-epoxy face sheets bonded by rigid polyurethane foam. The face sheets are made of epoxy matrix reinforced by carbon fibers along longitudinal and transversal directions. All the tested samples were 47 in length, 2 in width and 0.286 in thick with 0.25 in of the thick of foam core.

The mid point of the beam was considered to be the optimum DOF from which to excite the flexural modes of the beam. This location is the best choice for the shaker and the reference accelerometer installation. Only one half of the beam was used as test model, the other half was used for symmetry reasons. The geometric symmetry with respect to Y axis (see Figure 5.4), avoided the rotation of the cross section at the middle of beam simulating a cantilever condition.

In the first stage, modal testing was performed using an intact sandwich beam in order to adjust the finite element model. Later, numerous fault scenarios were created by introducing different types of damages at diverse locations along the beam. These included bond and core failures and superficial cracks. The objective of the study was to evaluate the scope of applicability of the method. Finally, multiple damage scenarios were analyzed to observe the behavior of modal parameters under these conditions.

5.2.2 Experimental Set Up

FRF measurements must be acquired by providing artificial excitation with one or more shakers attached to the structure. Two common types of shakers are electro dynamic and hydraulic shakers. A variety of broad band excitation methods can be used, employing low level random, sine or transient signals [51]. At least a 2 channel Fast Fourier Transform (FFT) analyzer and a single axis accelerometer are required to make FRF measurements using a shaker. In this work, the test structure was set into vibration by using a VTS (Vibration Test Analysis) electro dynamic shaker [52]. The shaker input signals were created from the Virtual Function Generator (VFG) of the SigLabTM commercial package [53]. A 6 channel DSPT SigLab Dynamic Signal Analysis (DSA) system [54] was used to deal with the signals. Figure 5.4 depicts the experimental equipment and set up and the coordinate system. The DSA system sends the excitation signal to the shaker through output channel 1 (OC1) while receiving the measurements from a reference accelerometer and a Laser Doppler Vibrometer (LDV) [55] through input channels 1 (IC1) and 2 (IC2).

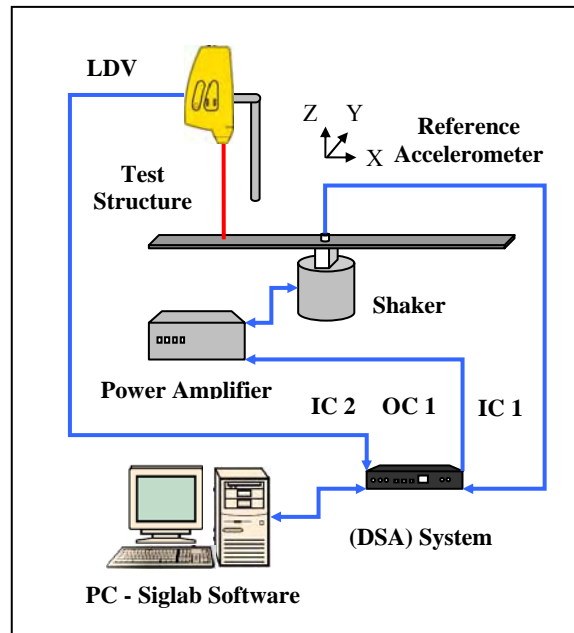


Figure 5.4: Modal testing set up.

The OMETRON VH300+ model (LDV) is a highly accurate and versatile non contact vibration transducer for applications where it is undesirable to mount a vibration transducer onto a vibrating object. It is optimal for vibrations measurements without mass loading on lightweight structures such as sandwich composite panels. Measurement noise was removed by using frequency domain averaging methods in Siglab.

It is important to note that only the translational DOF in the Z direction was considered in this analysis. First, the shaker was driven with a random input signal. The first three flexural frequencies were identified from FRF measurements as peaks frequencies. Later, the structure was excited by sinusoidal signals equal in frequency to the peak frequencies in order to excite one natural mode at a time. The response of the structure (displacements) was measured by positioning the LDV at several locations along the span of the test specimen. Then, the displacements vectors were exported to MATLAB[®] where curvature mode shapes were computed. This data was stored in an adequate format for further classification purposes.

5.2.2 Results

Experimental Undamaged Case

We started our test by driving the shaker at a random input signal of bandwidth 0 - 500 Hz. It was expected that the first three modal frequencies of the intact cantilever beam were in this range. The magnitude and phase of the obtained FRF are shown in Figure 5.5. Clearly, the three peaks can be identified at about 26 Hz, 135 Hz and 315 Hz. In addition, phase shifts of approximately 180 degrees occurred at those frequencies. These peak frequencies were related to the modal frequencies of the specimen. Table 5.1 lists the first three flexural modal frequencies for the undamaged beam. Mode shapes can be sampled from as many points on the structure as desired. The more a mode shape is measured (sampled) across the span of the beam, the more accurately a change can be identified with a specific region of the structure when it occurs. In order to characterize

each mode shape with reasonable fidelity, sufficient test points are required. According to literature the [56], reasonable fidelity is commonly accepted to be at least 10 points/cycle along any axis with sine like deformations. For a cantilever beam in bending, sinusoidal like deformation occurs along the span of the beam. The highest spatial frequency is a sine cycle along the X axis and corresponds to the 3rd mode shape (see Figure 5.7).

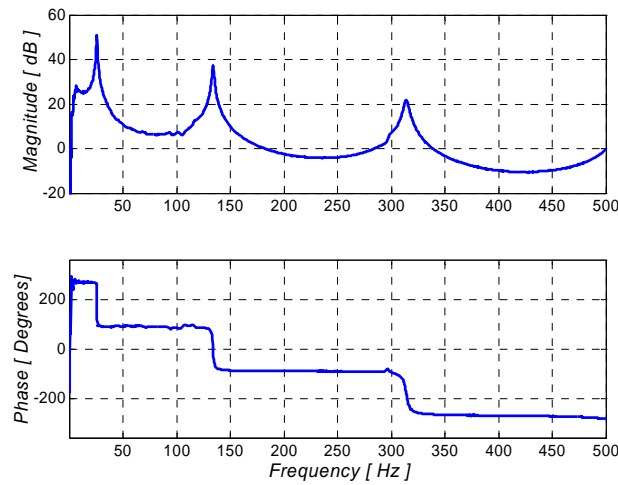


Figure 5.5: Bode plot - Intact beam.

Table 5.1. Experimental natural frequencies.

Mode N ^o	Natural Frequency [Hz]
1 st	25.625
2 nd	134.062
3 rd	314.062

The test model was chosen to have 24 equally spaced points in the X direction from the reference accelerometer to the end of the beam. Along the Y axis for a given X location, the Z deformations appeared to be straight lines and parallel to the Y axis when the structure vibrates in bending. Therefore any point in this direction may be sampled. Figure 5.6 shows a scheme of the positions where displacements in the Z direction were measured.

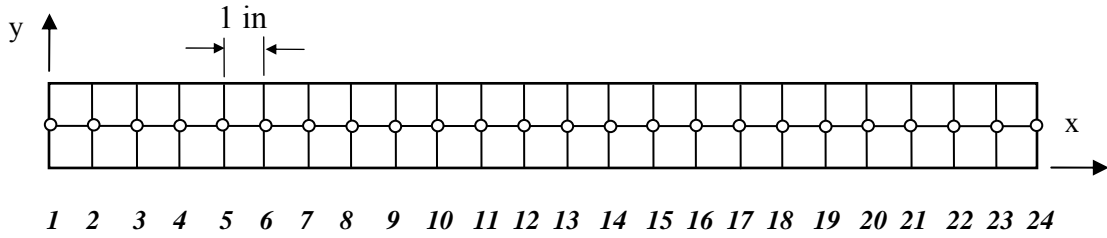


Figure 5.6: Measuring nodes.

In order to excite one mode shape at a time, the beam was excited by a sinusoidal signal equal in frequency to each peak frequency. The response of the structure was measured sequentially at every node. Mode shapes and curvature mode shapes are plotted in Figure 5.7 and Figure 5.8. The irregularities in the experimental curvature mode shapes are caused by small errors introduced in the measurements. In this case, there was no damage present in the structure. These curvature mode shapes will be used to compare with all later damaged cases.

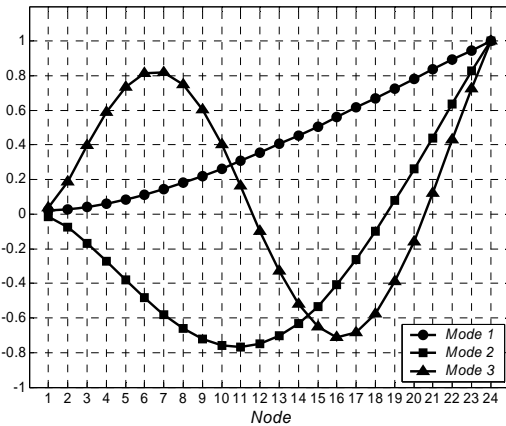


Figure 5.7: Mode shapes - Intact beam.

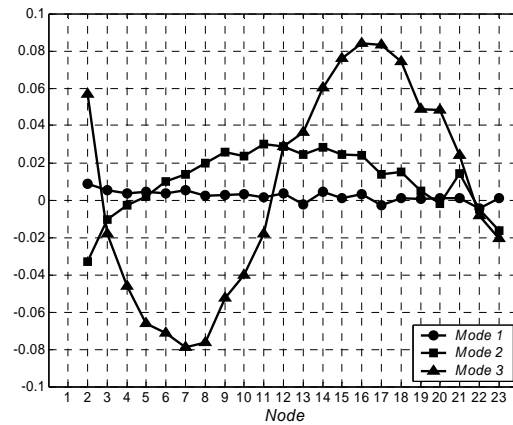


Figure 5.8: Curvature - Intact beam.

Any difference between such states will be represented by a peak in the difference of curvature. Figure 5.9-5.11 compare experimental with FEA mode shapes for the intact beam. From these figures, we can see that after optimizing the properties the FE model successfully predicts the dynamic behavior of the undamaged test specimen.

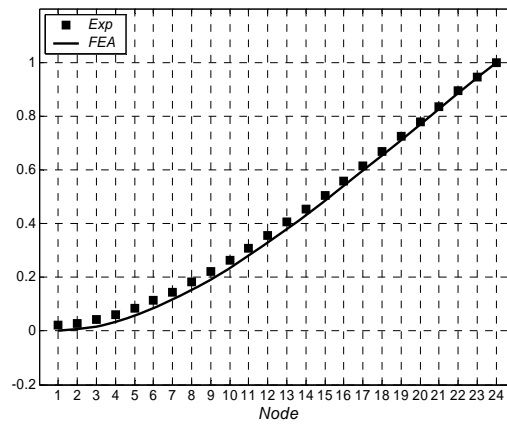


Figure 5.9: Mode shape 1 - Intact beam.

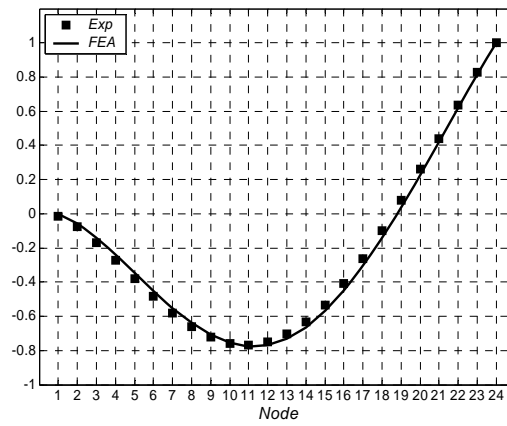


Figure 5.10: Mode shape 2 - Intact beam.

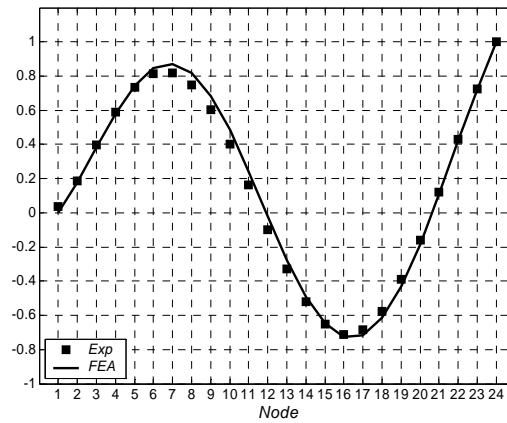


Figure 5.11: Mode shape 3 - Intact beam.

Experimental Damaged Case 1

An artificial bond failure was introduced into the test specimen by debonding the interface between the foam core and the upper face sheet. The damage size was 1 in length and 2 in width; the location was between nodes 5 - 6 according to damage case 2 simulated in section 3.6.1 (Figure 5.12). The same testing methodology used for the intact beam was followed in this case. The Magnitude and Phase of the FRF were plotted in Figure 5.13. Three new peaks were identified near to undamaged frequencies. These peaks were related to the modal frequencies of the structure. Table 5.2 lists the first three flexural frequencies corresponding to this test specimen.

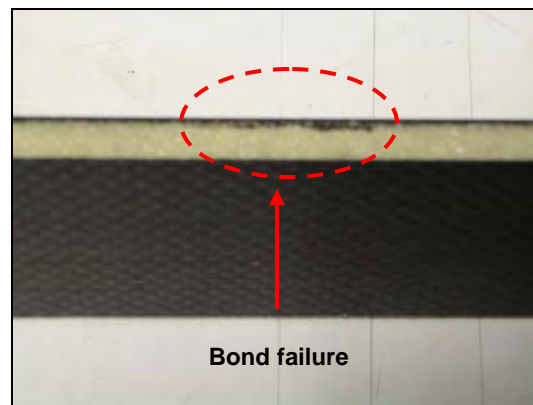


Figure 5.12: Damage case 1.

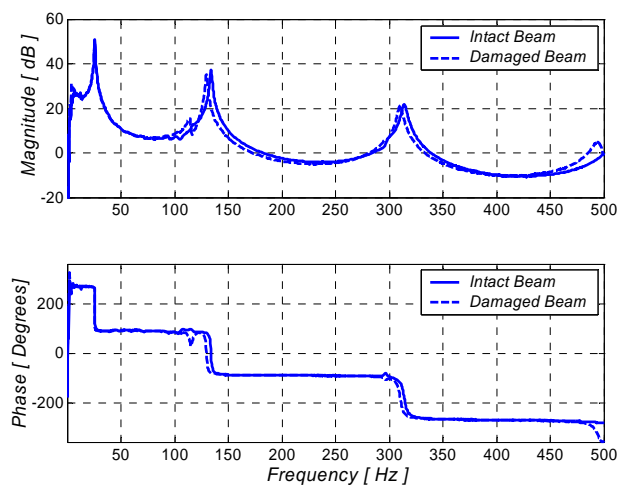


Figure 5.13: Bode plot - Damage case 1.

Table 5.2. Experimental natural frequencies.

Mode N°	Natural Frequency [Hz]
1 st	25.312
2 nd	129.687
3 rd	310.312

The natural frequencies have decreased from those corresponding to the undamaged case. However, noted in chapter 3, this feature can not be used to detect the damage. Therefore in the following test cases this modal parameter will not be shown as part of the results. Mode shapes and curvature mode shapes are plotted in Figure 5.14 and Figure 5.15.

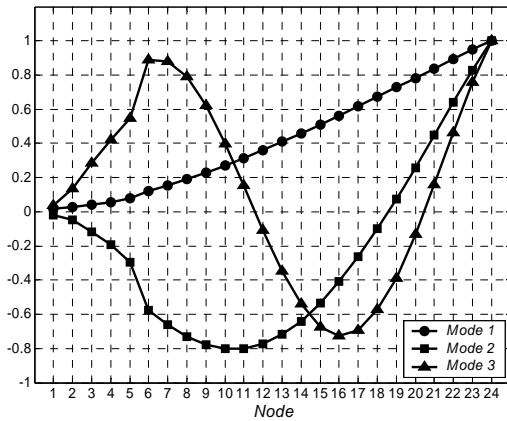


Figure 5.14: Mode shapes - Damage case 1.

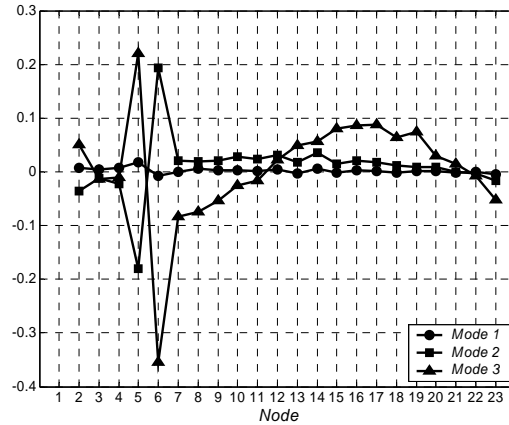


Figure 5.15: Curvature - Damage case 1.

Figures 5.16-5.18 compare measured damaged mode shapes with FEA results. As in the previous case, the numerical solution was very accurate. In Figures 5.19-5.21 theoretical and experimental differences in curvature were plotted. Because the curvature was calculated using the second derivate approximation, the numerical curvature mode shapes are less precise than de displacement mode shapes. The reason for the differences between the numerical and the experimental results in Figure 5.19 is because the changes in curvature are in the order of magnitude of the error in the measurements. Figure 5.22 shows the differences in the three curvature mode shapes in the same scale.

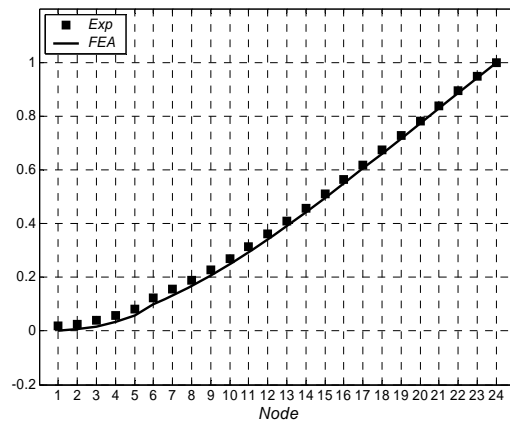


Figure 5.16: Mode shape 1 - Damage case 1.

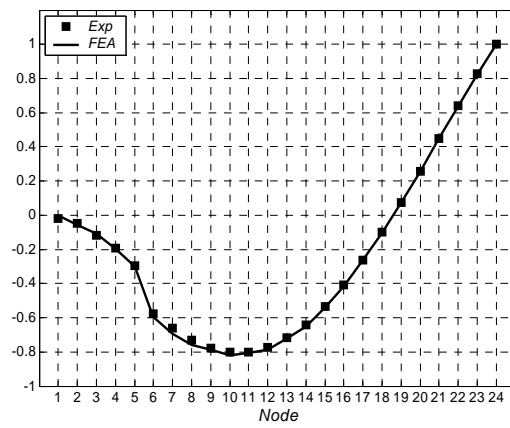


Figure 5.17: Mode shape 2 - Damage case 1.

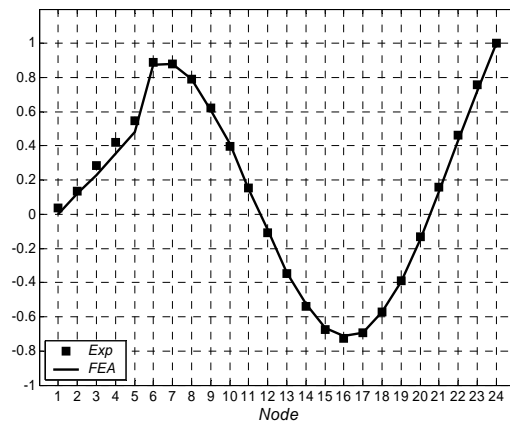


Figure 5.18: Mode shape 3 - Damage case 1.

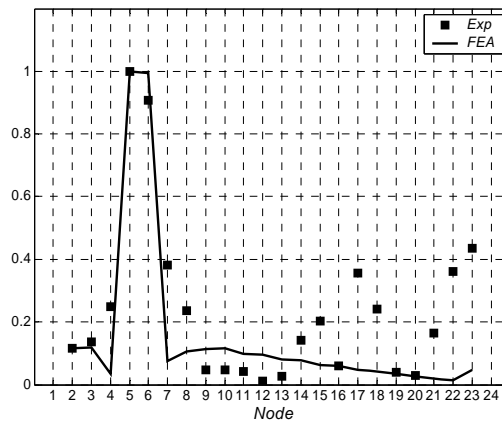


Figure 5.19: Difference in curvature mode shape 1.

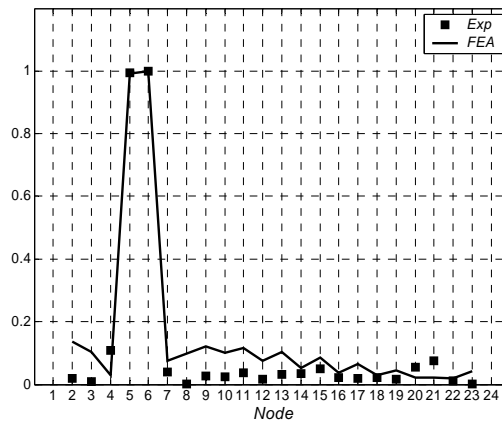


Figure 5.20: Difference in curvature mode shape 2.

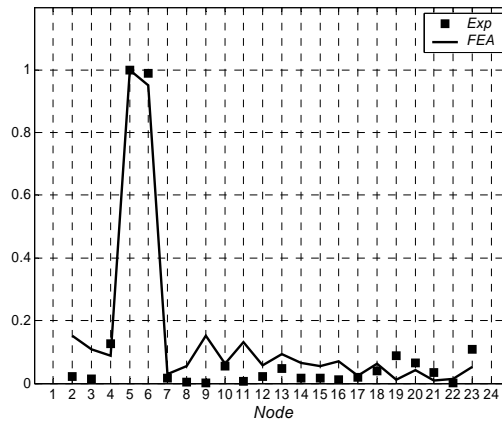


Figure 5.21: Difference in curvature mode shape 3.

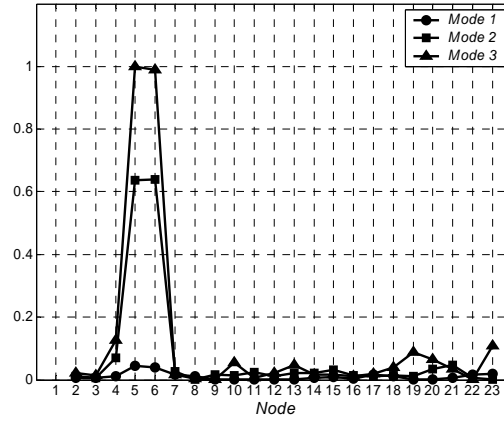


Figure 5.22: Difference in curvature - Damage case 1.

Experimental Damaged Case 2

This damage scenario contains a core failure placed at the same location as in the previous case. This core failure was created by making a 1 in x 2 in x 0.0625 in perforation through the foam core of the sandwich beam (Figure 5.23). Since the difference between curvatures mode shapes has been selected as a feature for damage detection, we will focus only in this result from modal testing. Figure 5.24 shows that the foam damage was successfully identify by the curvature approach.

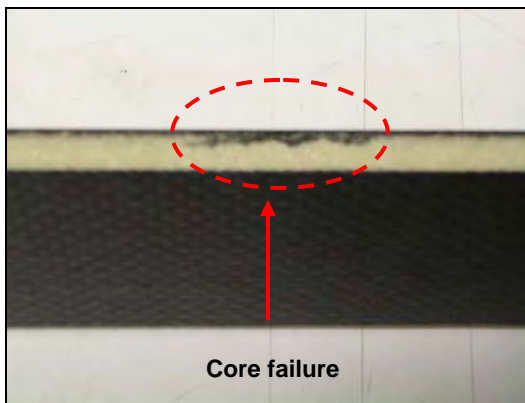


Figure 5.23: Damage case 2.

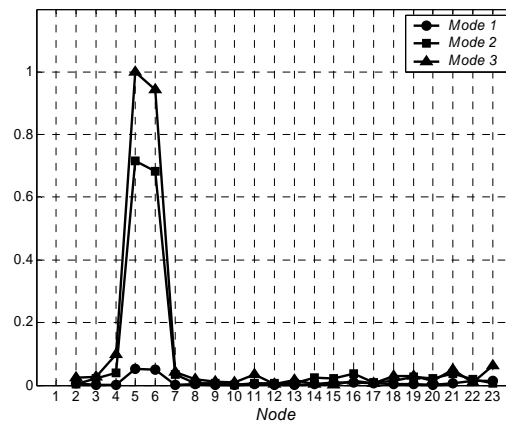


Figure 5.24: Difference in curvature.
Damage case 2.

Experimental Damaged Case 3

Test beam 3 involves a 0.375 in x 2 in width bond failure at node 11 (Figure 5.25). This damage was artificially introduced into the specimen by the same technique used in damaged beam 1. In this case, the size of the damage is significantly smaller than that in the two specimens tested so far. Figure 5.26 demonstrates that the natural mode shapes do not always change when the structure is damaged while the curvature mode shapes plotted in Figure 5.27 show irregularities in the damaged area. In Figure 5.28, the difference between undamaged and damaged curvature peaks the damage location.

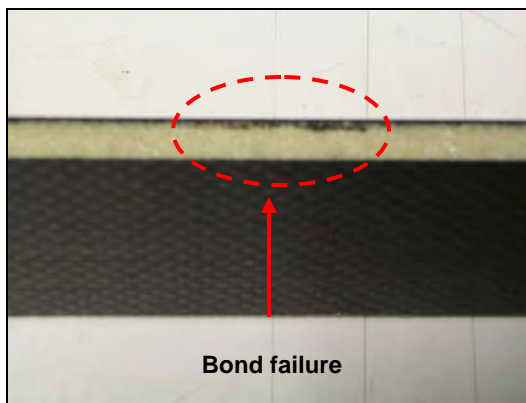


Figure 5.25: Damage case 3.

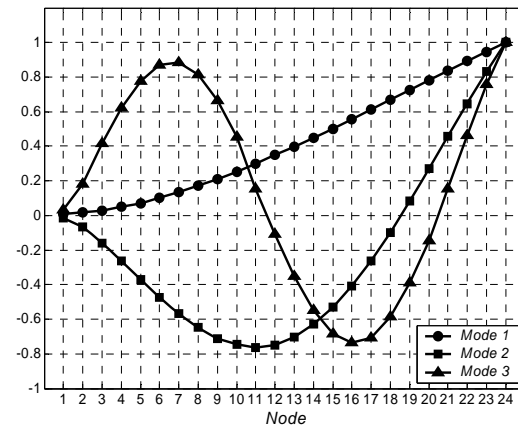


Figure 5.26: Mode shapes - Damage case 3.

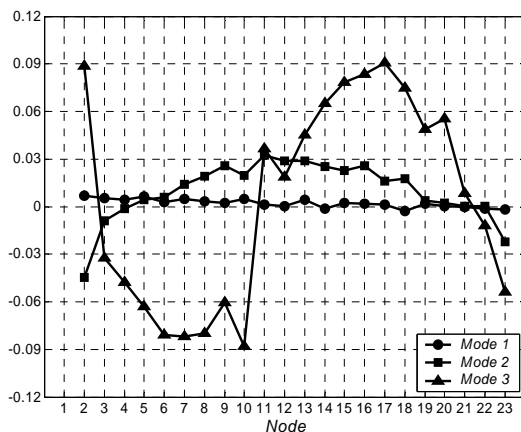


Figure 5.27: Curvature - Damage case 3.

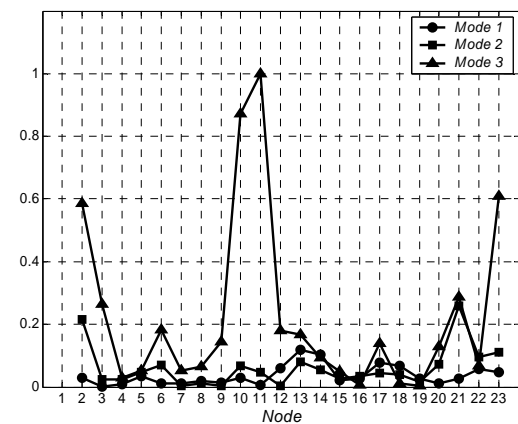


Figure 5.28: Difference in curvature.
Damage case 3.

Modes 1 and 2 do not show any significant difference, only mode 3 picks up the damage location in the vicinity of node 11.

Experimental Damaged Case 4

A superficial crack was created in the upper face sheet of the test specimen. The fissure was 0.75 in length oriented along the Y axis and it was placed between nodes 12-13 (Figure 5.29). Curvature mode shapes were computed and compared with the undamaged case in Figure 5.30.

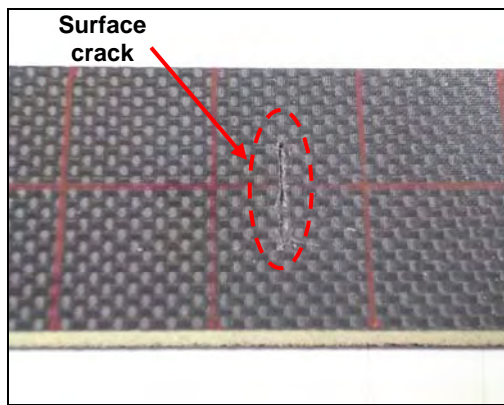


Figure 5.29: Damage case 4.

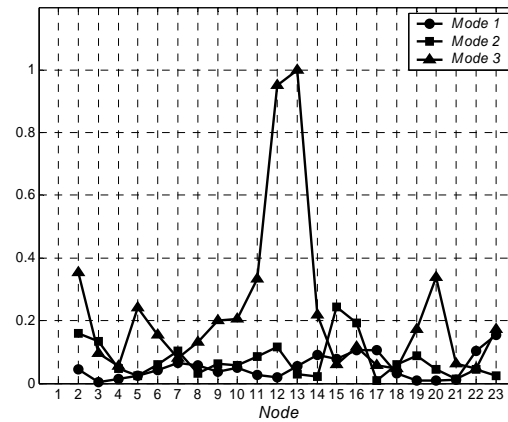


Figure 5.30: Difference in curvature.
Damage case 4.

In both cases, the first and second curvature mode shapes were unable to predict the defect location. Only the third mode was able to detect the presence of the damage. The curvature approach may not succeed when damage does not severely reduce the stiffness of the structure such (small damage size). The term small is related to the size of the structure under study. According to the results obtained in this section, we can conclude that a 0.5 in damage length is approximately the smallest size that the curvature method is able to detect accurately for the studied beams.

Multiple Damages States

In chapter 3 we investigated the behavior of curvature mode shapes when multiple damages were present in the beam. The numerical results showed that, theoretically, this method successfully identify simultaneous damage locations. To validate those results, multiple (two) damage scenarios were tested. The first of these multiple damage states involves two bond failures located between nodes 5 and 6 and nodes 9 and 10 respectively. The curvature mode shapes were calculated and compared with those corresponding to the intact beam (Figure 5.31).

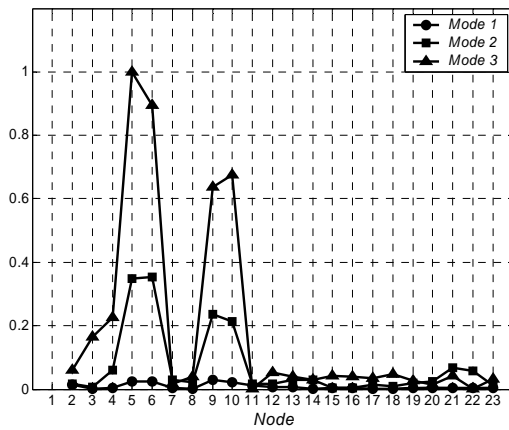


Figure 5.31: Difference in curvature.
Damage case 5.

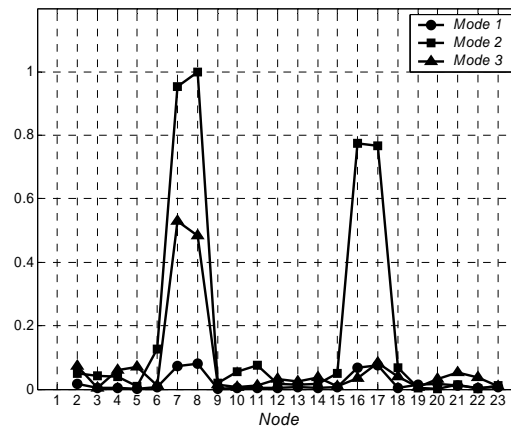


Figure 5.32: Difference in curvature.
Damage case 6.

Although all curvatures show peaks at the damage locations, the third mode shape was the most sensitive to the defects. The next multiple damage beam includes a bond failure between nodes 7 and 8 and a core failure between nodes 16 and 17. The differences in curvature mode shapes were plotted in Figure 5.32. In this case the damage locations were better identified by the second curvature mode shape. These experimental measurements demonstrate that the curvature approach is very suitable for multiple damage scenarios.

5.3 Infrared Thermography Testing

Infrared (IR) thermography measures surface emissions in the IR radiation band, which are directly related to surface temperature. Any phenomenon that creates measurable temperature changes can be visualized [57]. Recent achievements in thermal acquisition systems have led to improvements in the capabilities of thermographic methods for nondestructive inspection of metallic and composite panels [32]. Transient thermography involves heating the surface of a target structure for a short period of time followed by the capture of the thermal decay using an infrared camera at time intervals Δt .

Current systems enable the recording, storage, and processing of hundreds of digitalized images at very fast rates. The thermal images are typically analyzed for the presence of hot spots which may indicate the existence of defects. Noise and optical distortions produce difficulties for the interpretation of the recorded data. Post processing is a required procedure for the determination of the size and location of damages in inspected structures.

5.3.1 Test Specimens

In this work, experimental infrared thermography was applied on sandwich composite panels described in section 5.2.2. The study of the surface temperature distribution was focused on a 2 in x 4 in area of the sample. The regular thermal distribution over the specimen was used to fit parameters used in the numerical model described in section 4.2. Several damages scenarios were created by introducing surface and subsurface artificial defects. These included surface cracks, indentations and bond failure. First, the thermal fields around simple damage scenarios were recorded. Then, the same analysis was performed on multiple damages states.

5.3.2 Experimental Set Up

The test specimen was mounted vertically and heated by the action of a hot air flow supplied by a blower [58]. The blower was kept in front of the sample until its surface temperature reaches a constant value 80 °C. An AVIO TVS 8500 Thermal Video System [59] based on an infrared imager with an InSb FPA detector was used to measure the surface emissions in the 3.5-5.1 μm range. The IR camera collected surface temperature from a 15.8 in distance from the specimen. A field view of 4 in width and 3.55 in high was obtained. A sequence of 12 thermal images with size 256 x 256 pixels were recorded with a time step of 5 second for each sample tested. Five seconds is the smallest time step that the AVIO system is able to record. In order to synchronize the images in different series, the temperature of an arbitrary point was set as a reference to start recording the thermal response of the beam. Figure 5.33 illustrates the experimental test set up.

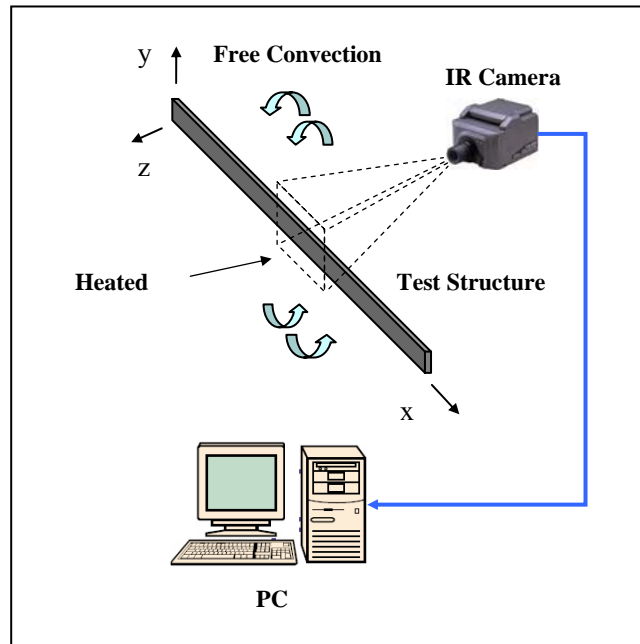


Figure 5.33: IR thermography testing set up.

The digitalized thermal response for the specimen was stored in a memory card for further analysis using the GORATEC PE Professional commercial software [60]. By

applying median based filters, noise and optical distortions were removed from the thermal images. Then, the original IR images were converted to Windows Bitmaps images (BMP). BMP image files are one of the file formats supported by the Image Processing Toolbox of MATLAB® [61]. The same defect edge extraction procedure used in section 4.6 was applied to the collected images resulting in a set of binary images. This method allowed the extraction of relevant features which will be used in chapter 6 for damage characterization purpose.

5.3.3 Results

Experimental Undamaged Case

The first thermal measurements correspond to a sandwich composite beam with no damages. This case allowed us to know the normal temperature distribution over this type of structure in response to a thermal excitation. This information was used to estimate the thermal properties of these particular materials. These include the thermal diffusivity α and the convection heat transfer coefficient h required for the numerical model. As mentioned in the previous section, each test was recorded in a series of 12 IR images at 5 second intervals. Figure 5.34 shows the cooling phase of the undamaged beam section.

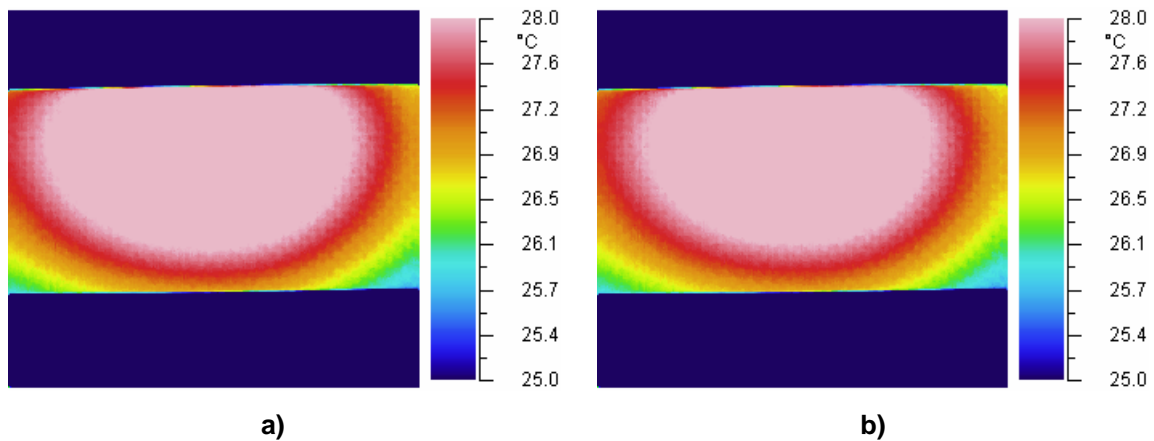


Figure 5.34. Undamaged case: a) 5 sec.; b) 10 sec.

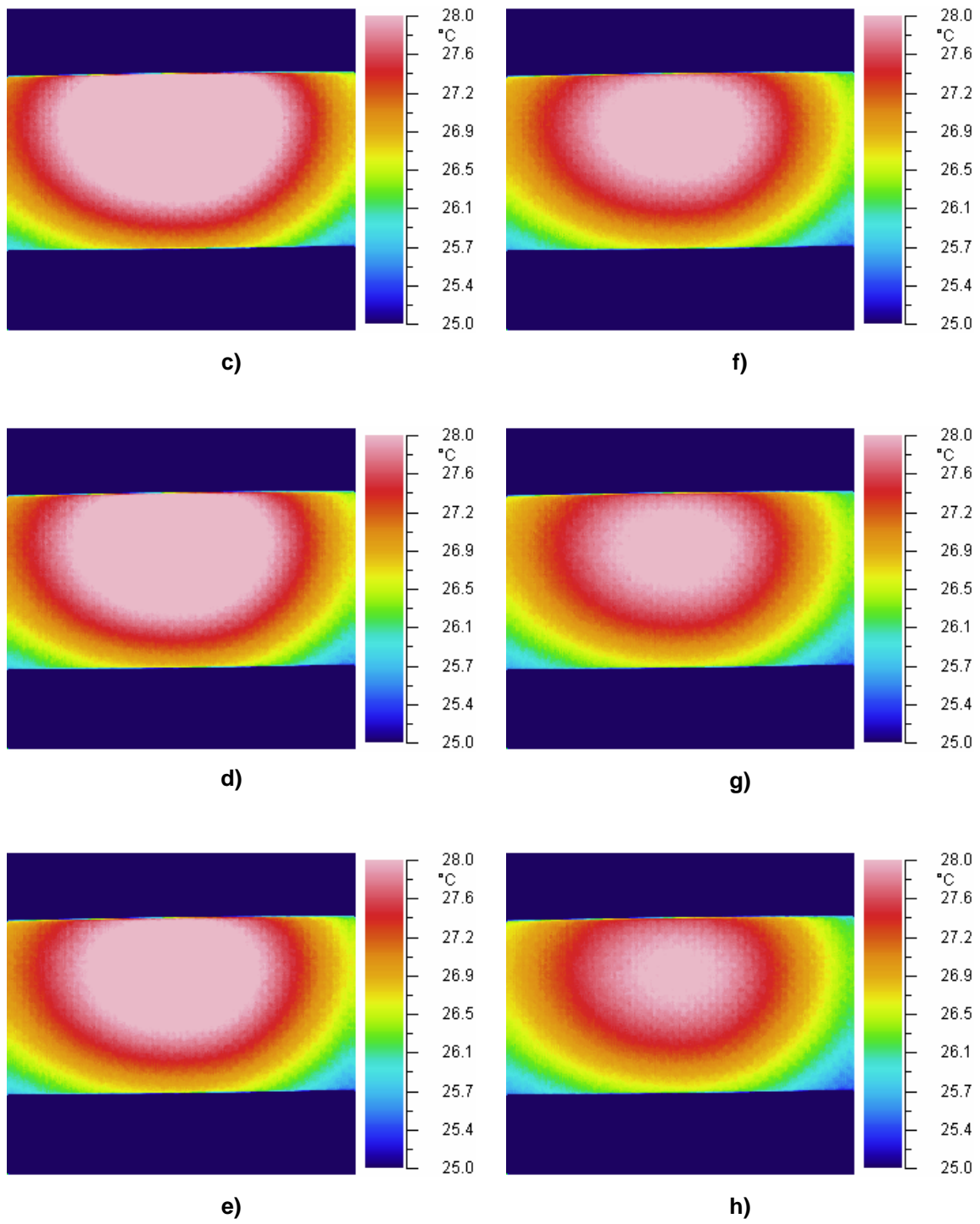


Figure 5.34. Undamaged case: c) 15 sec.; d) 20 sec.; e) 25 sec.; f) 30 sec.; g) 35 sec.; h) 40 sec.

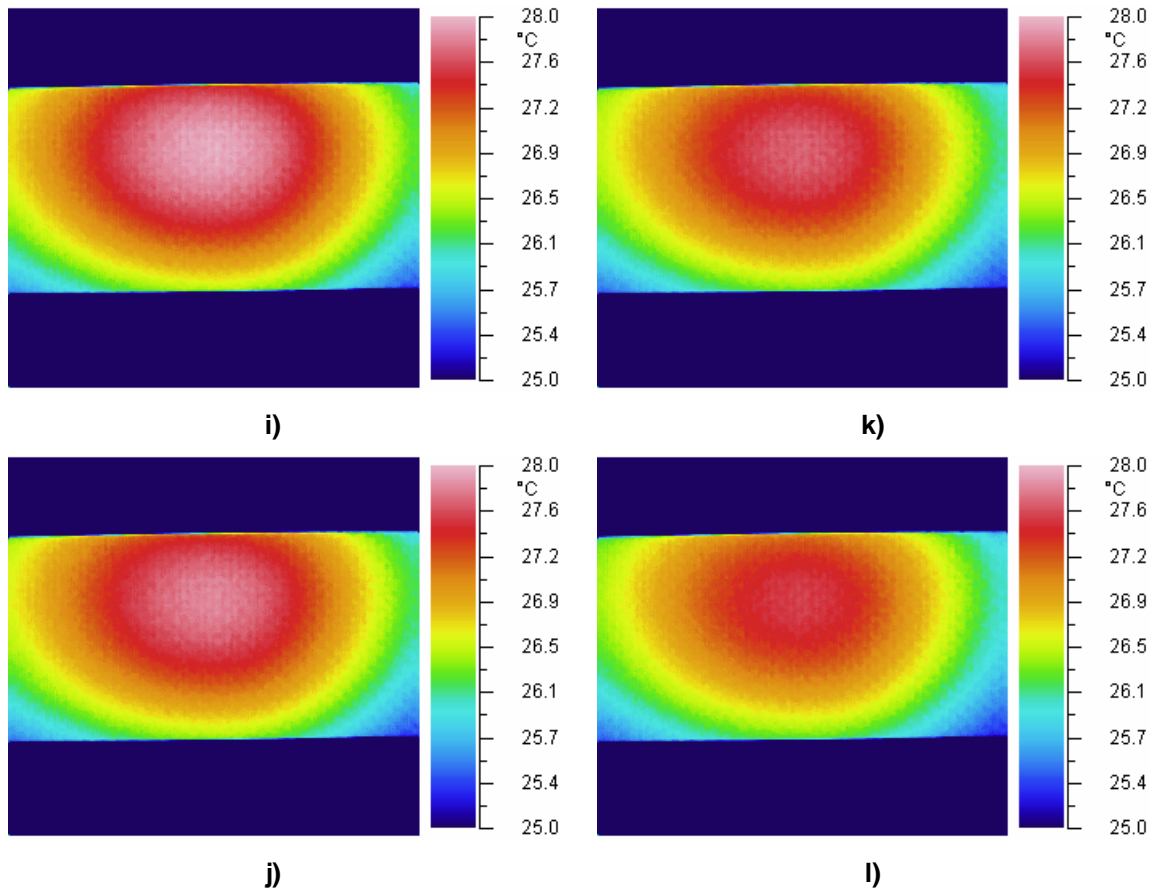


Figure 5.34. Undamaged case: i) 45 sec.; j) 50 sec.; k) 55 sec.; l) 60 sec.

As mentioned in chapter 4, the isotherms also are elliptical shapes shifted from the center of heating. This effect is a result of the variation of the coefficient h along Y direction.

Experimental Damaged Case 1

The first damage scenario studied using IR thermography was a 1/16 in indentation through the face sheet of the sandwich composite (Figure 5.35). The damage was placed inside the heated area. Thus, while the isotherms move during the cooling phase, the defect location becomes visible.

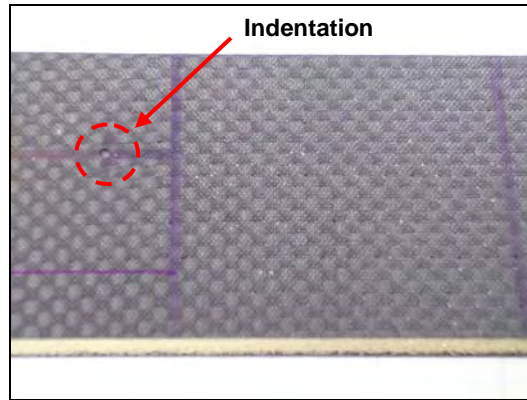


Figure 5.35: Damage case 1.

Figure 5.36 shows the thermal response for this damage case. As can be noticed, not all the thermal images provide clear evidence of the damage. This effect is related to both the time at which the image was taken and the temperature scale used to represent the thermal distribution. Clearly, a hot spot can be identified in Figures 5.36 b, c, f, and g. This feature will be extracted from these images using a defect edge extraction procedure based on image gradient computation (`contour` [61]). The information obtained from this technique will be used to characterize this damage case.

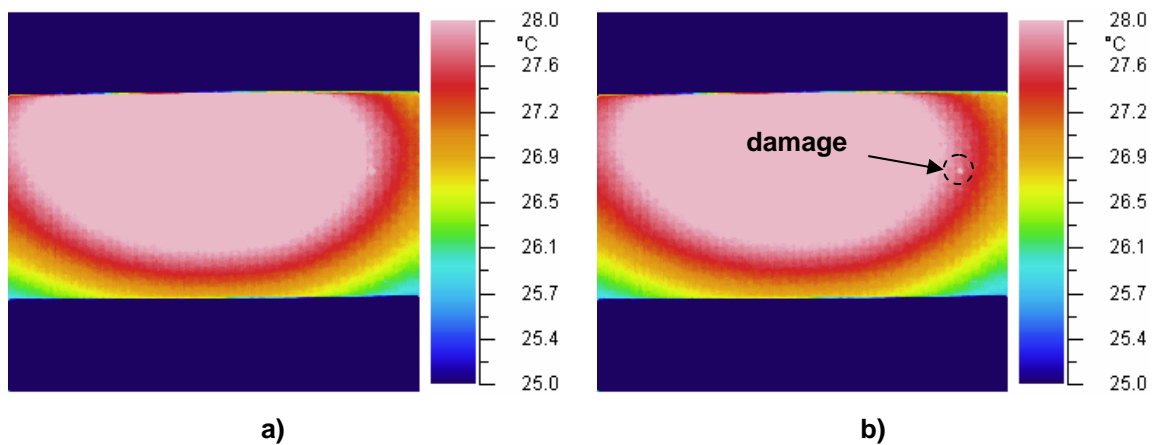


Figure 5.36. Damaged case 1: a) 5 sec.; b) 10 sec.

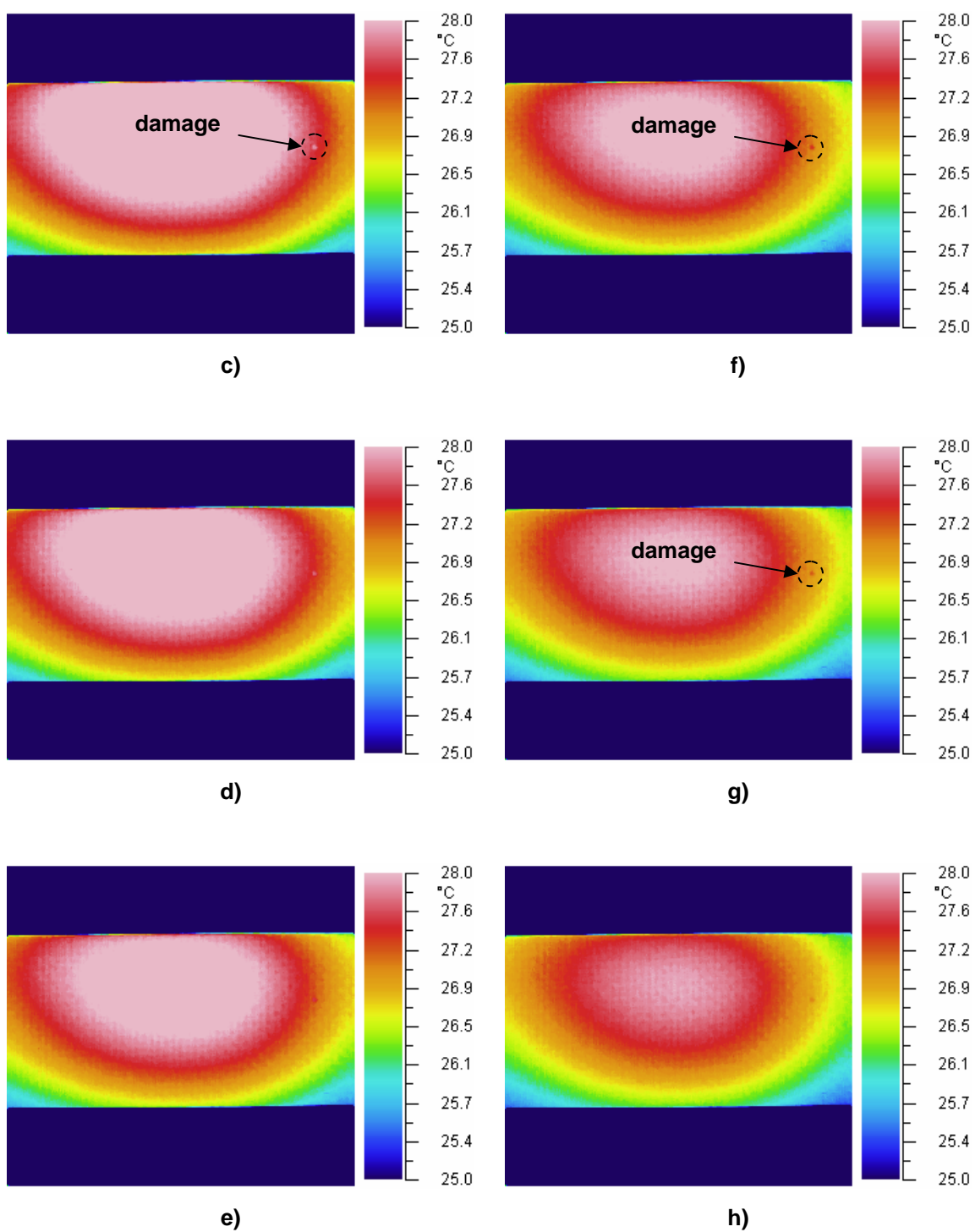


Figure 5.36. Damaged case 1: c) 15 sec.; d) 20 sec.; e) 25 sec.; f) 30 sec.; g) 35 sec.; h) 40 sec.

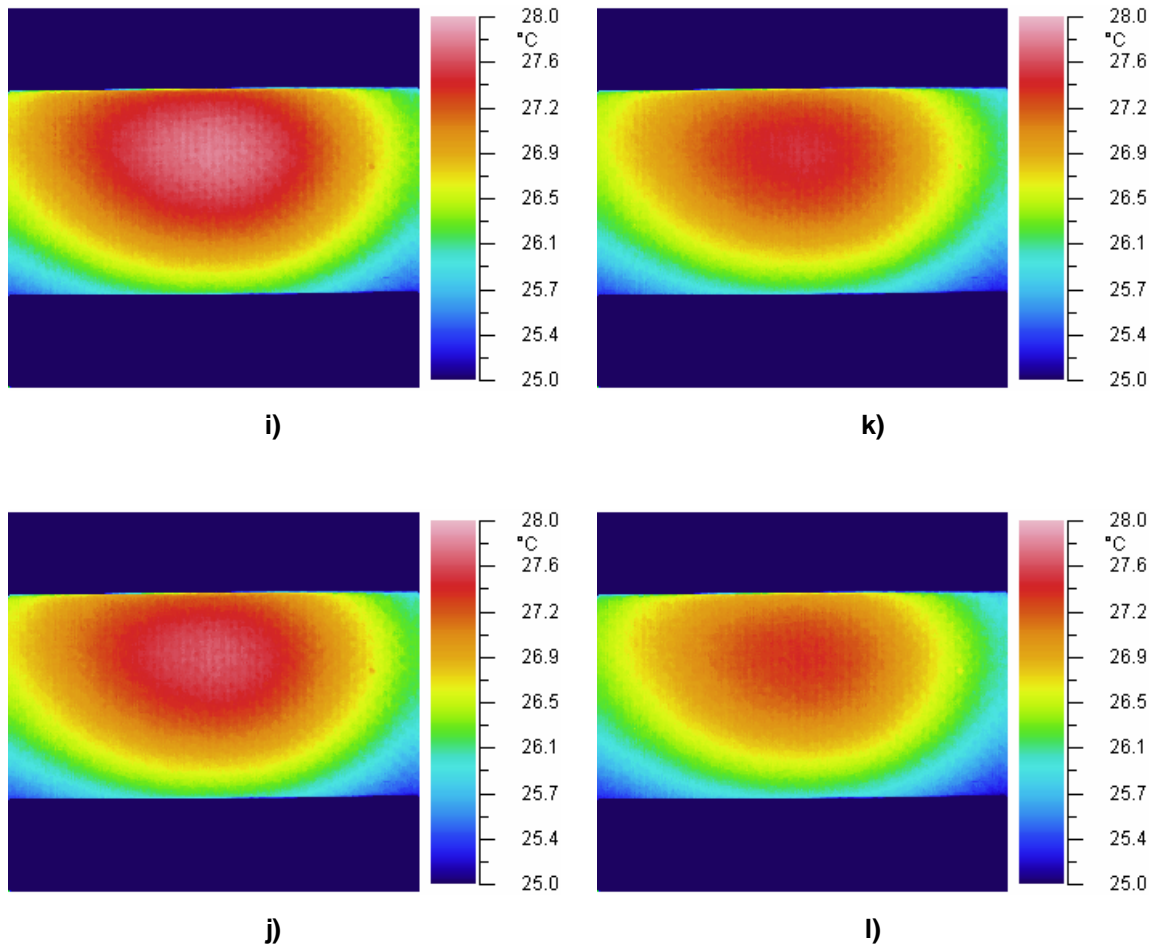


Figure 5.36. Damaged case 1: i) 45 sec.; j) 50 sec.; k) 55 sec.; l) 60sec.

Experimental Damaged Case 2

This damage state involves the same type of damage studied in the previous case but with a different location. Here, we are interested in determining the relationship between the damage site and the time at which it is detected. The thermal response for this damage case is plotted in Figure 5.37. From Figures 5.37 b, c, f, and g, there is no evidence of the damage. However, in Figures 5.32 i, j, and k the hot spot can be noticed inside the red area. Therefore we can conclude that the time of the damage visualization

is related to the relative position of the damage respect to the heated zone. Thus, the whole series of IR thermal images will be used to detect the damage.

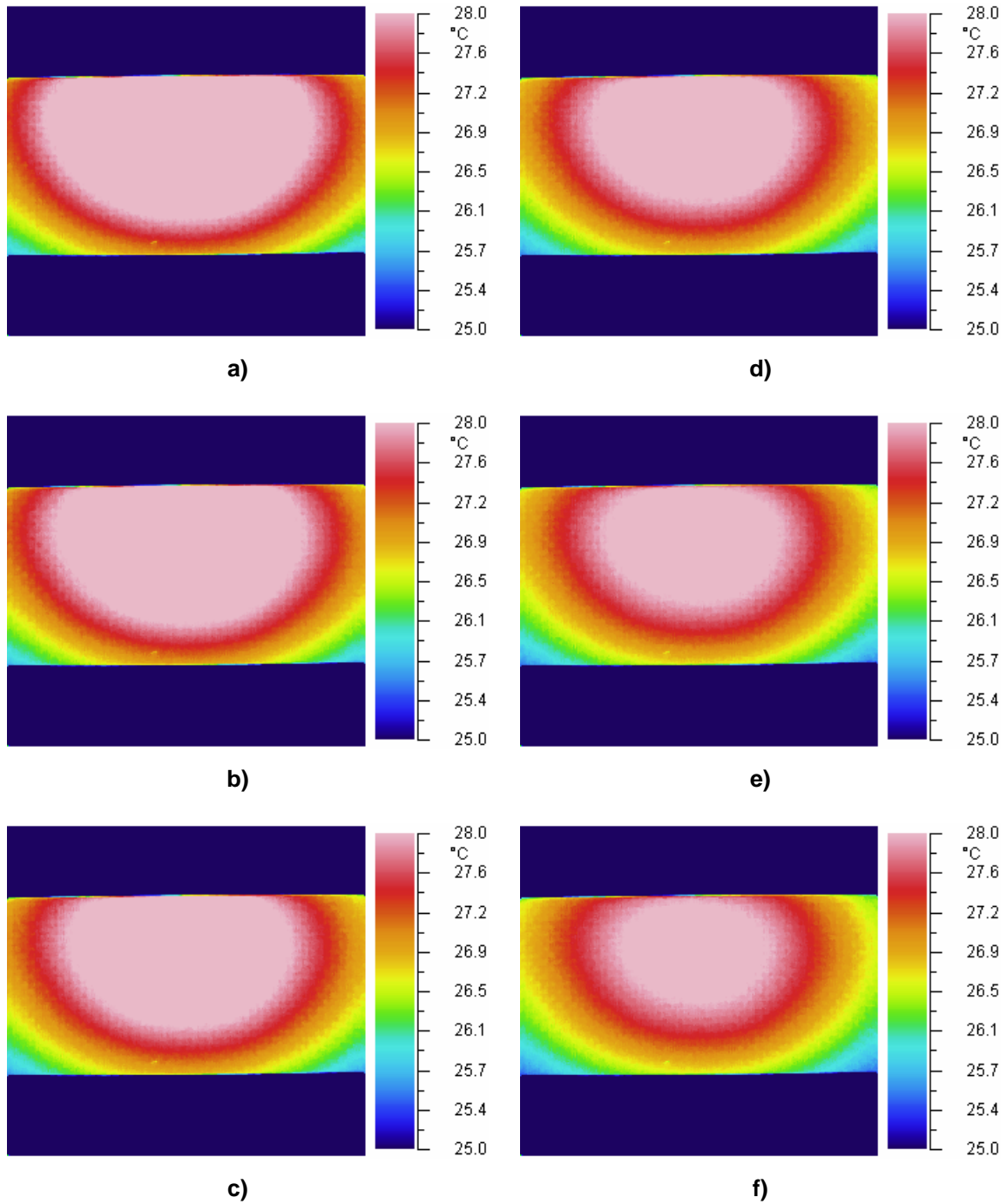


Figure 5.37. Damaged case 2: a) 5 sec.; b) 10 sec.; c) 15 sec.; d) 20 sec. e) 25 sec.; f) 30 sec.

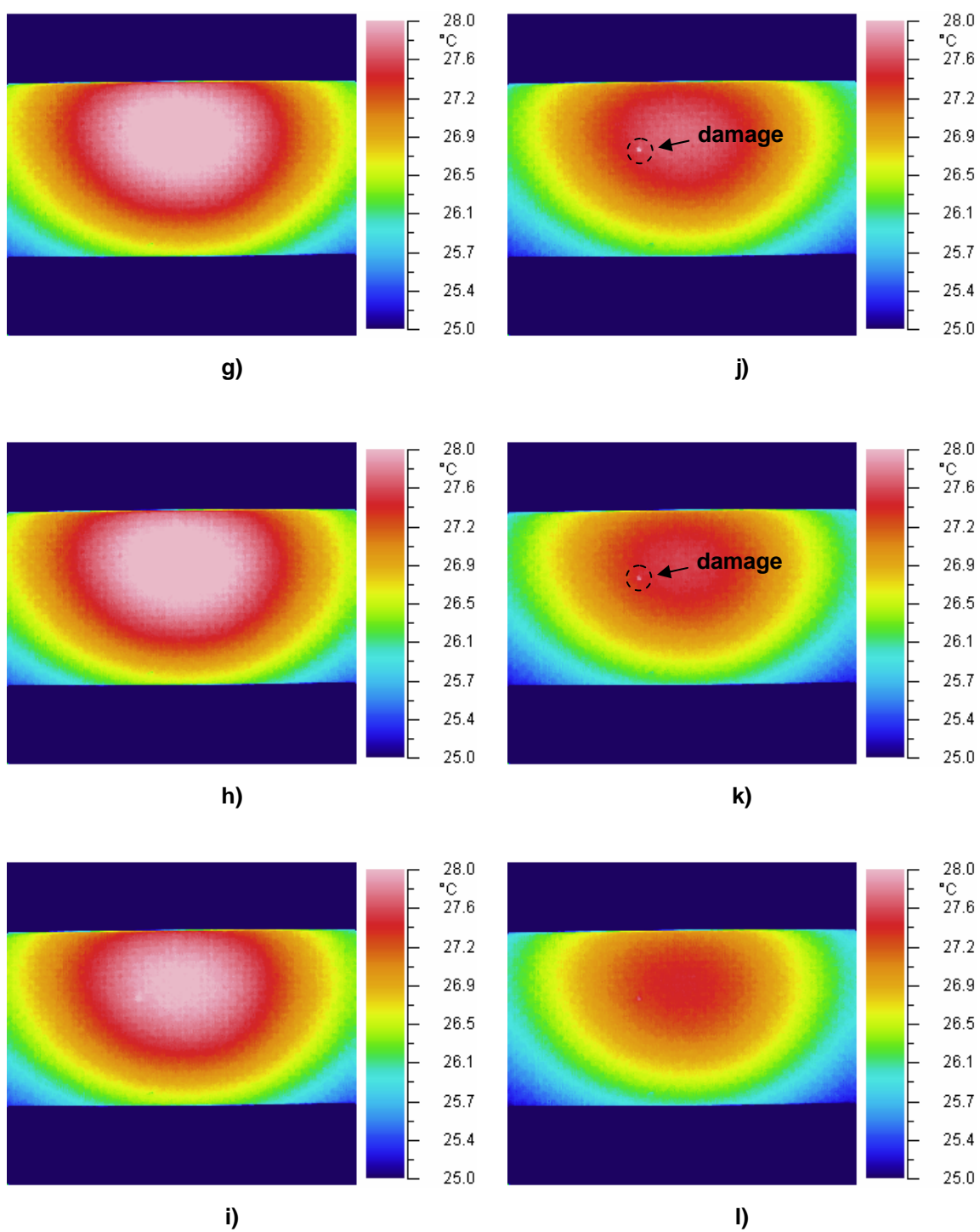


Figure 5.37. Damaged case 2: g) 35 sec.; h) 40 sec.; i) 45 sec.; j) 50 sec.; k) 55 sec.; l) 60sec.

Experimental Damaged Case 3

A 1/8 in hole through the face sheet of the sandwich beam was tested using the current technique (Figure 5.38). Although 12 IR images were recorded from this test case, only those where the damage is visible are plotted in the following figures. Figure 5.39 shows the thermal response at 5, 10, 30 and 35 seconds respectively. Due to the location of this damage, it can be identified at the beginning and at the middle of the period of observation.

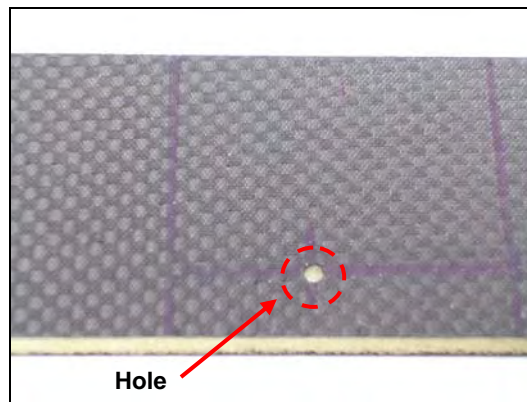


Figure 5.38: Damage case 3.

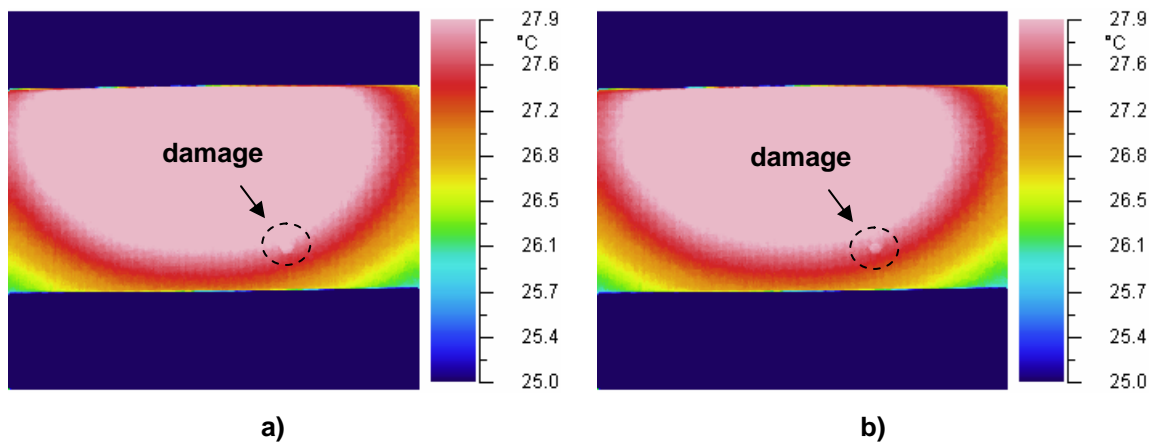


Figure 5.39. Damaged case 3: a) 5 sec.; b) 10sec.

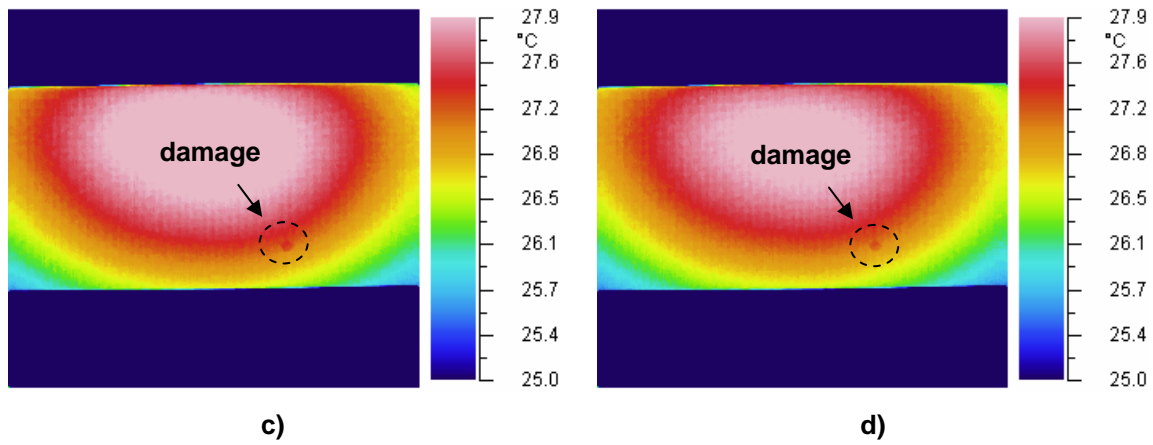


Figure 5.39. Damaged case 3: c) 30 sec.; d) 35 sec.

Experimental Damaged Case 4

The fourth damage case consists of a 3/8 in surface crack oriented in Y direction (Figure 5.40). The most representative thermal images are shown in Figure 5.41. Because of its location is near to the center of the heated area, the crack was not visible until the 50 seconds. But as mentioned previously, if it is located elsewhere with respect to the centre of the heated zone it appears at other time intervals.

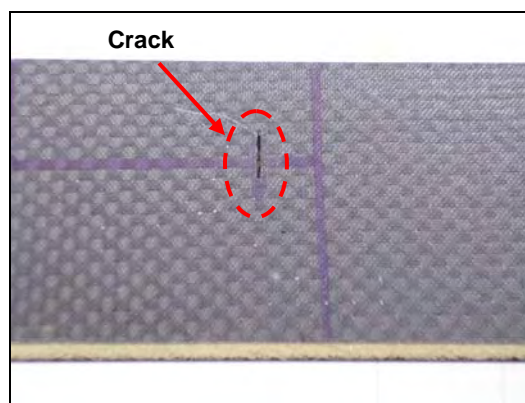
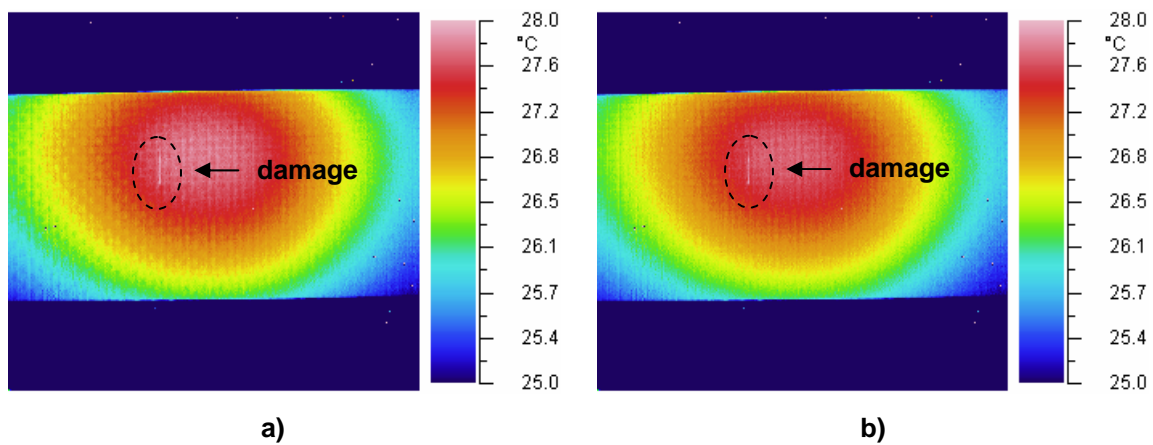


Figure 5.40: Damage case 4.



Figures 5.41. Damaged case 4: a) 50 sec.; b) 55 sec.

Experimental Damaged Case 5

All the damage cases studied so far were artificial surface damages. Now, IR thermography is tested in detecting internal defects. A 1 in x 2 in bond failure was introduced into the test specimen by debonding locally the interface between the foam core and one of the face sheets (Figure 5.42). The sample was heated by the same technique used in the other cases.

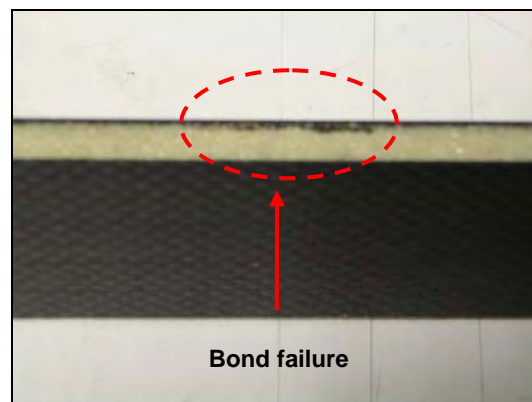
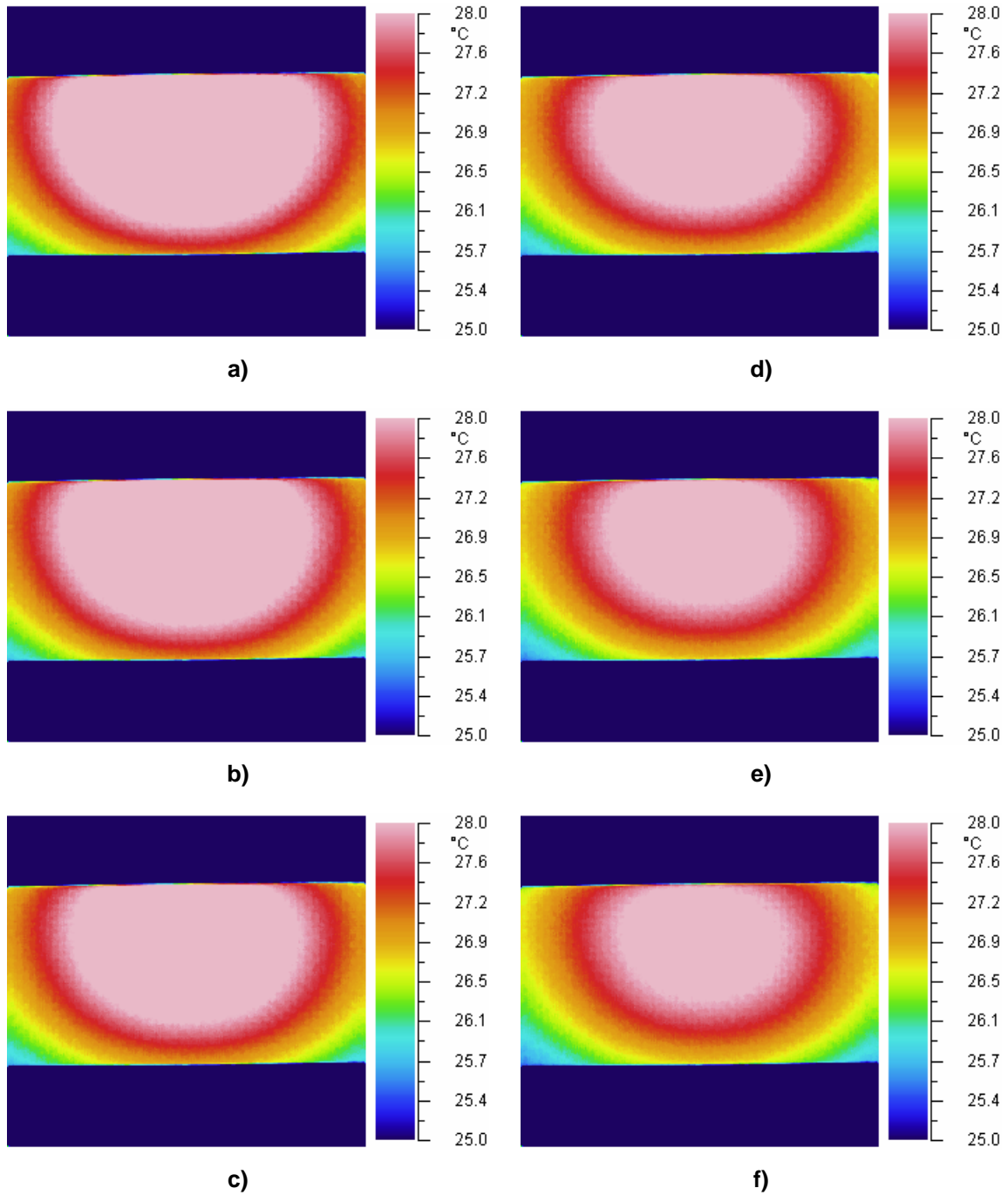
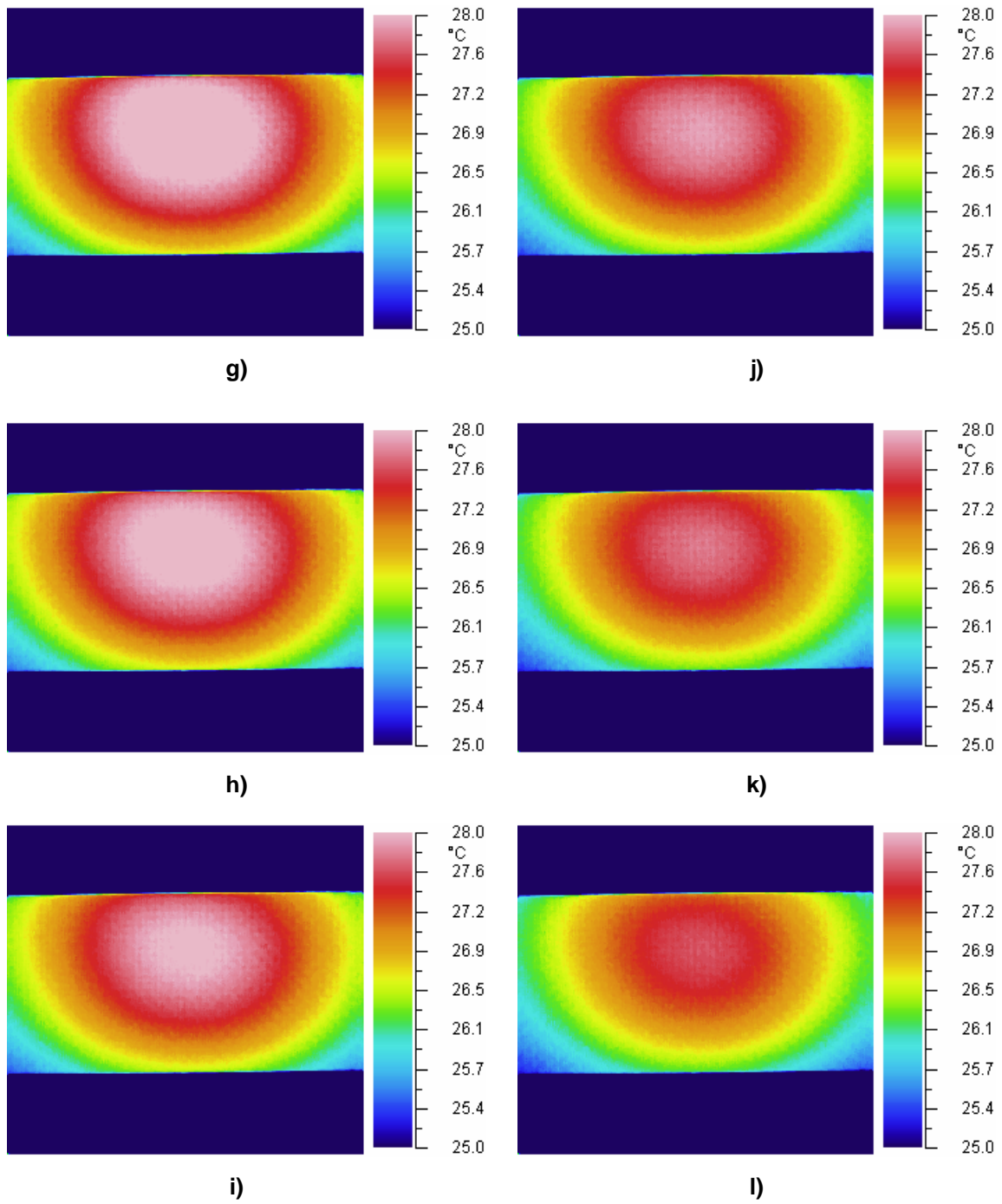


Figure 5.42: Damage case 5.

None of the Figures 5.43 shows evidence of the presence of the bond damage. This result leads to the conclusion that IR thermography is restricted to surface damage cases.



Figures 5.43. Damaged case 5: a) 5 sec.; b) 10 sec.; c) 15 sec.; d) 20 sec.; e) 25 sec.; f) 30 sec.



Figures 5.43. Damaged case 5: g) 35 sec.; h) 40 sec.; i) 45 sec.; j) 50 sec.; k) 55 sec.; l) 60 sec.

In section 5.2.3 the curvature approach successfully located bond failures while it was unable to identify small damages. According to previous mentioned the curvature approach and IR thermography have their own limitations. Thus, these two NDE methods are complementary each other and they can be used together to improve damage detection performances.

Chapter 6

Neural Network Implementation

This chapter deals with the analysis and classification of the numerical data and experimental measurements from previous chapters. A brief introduction to neural network (NN) theory is discussed. Then several types of NNs are mentioned and the selection of the probabilistic neural network (PNN) is justified. Single and multiple damage scenarios are studied in order to check the NNs performance in damage detection. Finally a unified approach for thermal and curvature data processing is proposed.

6.1 Preface

The diagnosis of a structure based on its response is an inverse process; the causes must be discerned from the effects [22]. This procedure requires specific data related to the response of the structure, to adequately search for defects through a mathematical model. A unique solution often does not exist for an inverse problem, especially when insufficient data is available. Thus, it is very difficult to evaluate an existing structure that has suffered some unknown type of damage using traditional damage detection methods based on a priori knowledge of damage scenarios.

In general, nondestructive damage detection involves the comparison of the changes in structural properties or responses, and it can be viewed as a classification problem. Effective classification or interpretation of the changes in the structural response or properties due to damage is a critical task. In chapter 1, the advantages of using artificial neural networks (ANNs) over other algorithms were discussed. These include [25] self-adaptiveness, generalization, abstraction capabilities and suitability for real-time applications.

ANNs are suitable for pattern classification and information processing tasks. ANNs are computational models composed of many simple and highly interconnected processing elements that process information and establish complex and highly nonlinear relationships and associations from large sets of data. ANNs, like people, learn by examples. In the approaches using ANNs, the data required to model an inverse relation are obtained as the solution of the direct problem [22]. For example, the changes in some structure parameters can be identified from the known structure response when the network has been trained properly. In the current work, these structural responses will be collected through computer damage simulations using the numerical models and through the experimental measurements. The advantages of using ANNs in general are their capacity to diagnose correctly, even when trained with partially inaccurate data, and their ability to continue learning and to improve their performance when presented with new training data.

A NN involves processing elements or neurons and interconnection weights between neurons. These interconnection weights determine the nature and the strength of the connection between neurons. A neuron with a single R-element input vector is shown in Figure 6.1. The individual element inputs p_1, p_2, \dots, p_R are multiplied by weights $w_{1,1}, w_{1,2}, \dots, w_{1,R}$ and the weighted values are fed to the summing junction. Their sum is simply \mathbf{Wp} , the dot product of the matrix \mathbf{W} and the vector \mathbf{p} .

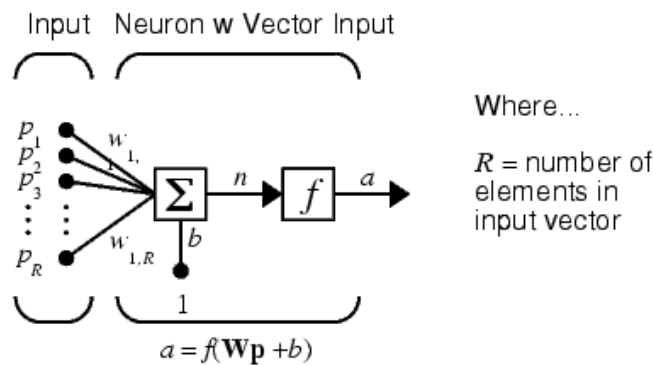


Figure 6.1: NN diagram.

The neuron has a bias b , which is summed with the weighted inputs to form the net input n . This sum, n , is the argument of the transfer function f , which produces the scalar output a . Examples of transfer functions are: hard-limit; linear; and log-sigmoid [62]. Note that w and b are both adjustable parameters of the neuron. Such parameters can be adjusted so that the network exhibits some desired behavior. Two or more of the neurons shown in Figure 6.1 can be combined in a layer, and a particular network could contain one or more such layers.

The overall methodology of using NNs is divided into two parts: (1) the training stage; and (2) the simulation stage. In the training stage, the network of interconnected neurons is presented with a set of input data and corresponding target output values. Then the interconnection weights among neurons and biases are iteratively adjusted, using predefined learning rules, so the NN can replicate the target output values with minimum error. The training algorithms direct how the weights and biases change in response to a given input and output pair during the training stage. All of these algorithms use a gradient based technique called back propagation, which involves updating the network weights and biases in the direction in which the error between the outputs and targets decreases most rapidly (the negative of the gradient). There are many variations of the back propagation algorithm: batch training (train); batch gradient descent (traingd); and batch gradient descent with momentum (traingdm). The knowledge learned by NNs is represented by the connection weights.

As mentioned in section 1.5, two types of learning methods are used for NNs: supervised and unsupervised training. Supervised training means that a network is presented with the correct response during training. On the other hand, unsupervised learning does not require knowing the correct response and can be used when there is a lack of knowledge of correct answers for training data. Once a NN has been trained and has reached an equilibrium state, the output in response to a particular input (test sample) is calculated as a summation of weighted inputs. The power of NNs comes to life when a

pattern that has no output associated with it, is given as an input. In this case, the network produces the output that corresponds to that of the least different pattern learned.

6.2 Neural Network Selection

In order to find the most effective ANN for damage severity and location predictions, different NNs were studied. Although traditional feed forward neural networks [15] are used in pattern classification, the non-linearity of the problem and the presence of random noise in the data demand a more robust model. For example perceptrons are especially suited for simple problems in pattern classification but they have several limitations. The most important is that perceptrons can only classify linearly separable sets of vectors. If a straight line or a plane can be drawn to separate the input vectors into their correct categories, the input vectors are linearly separable. If the vectors are not linearly separable, learning will never reach a point where all vectors are classified properly.

On the other hand, Hopfield networks [62] can act as error correction or vector categorization networks. Input vectors are used as the initial conditions to the network, which recurrently updates until it reaches a stable output vector. Hopfield networks are interesting from a theoretical standpoint, but are seldom used in practice. Even the best Hopfield designs may have false stable points that lead to incorrect answers. More efficient and reliable error correction techniques, such as back propagation, are available.

Radial basis networks [15] are statistical based models. These NNs require more neurons than standard feedforward back propagation networks, but often they can be designed in a fraction of the time it takes to train standard feedforward networks. One of the designs of radial basis networks is the probabilistic neural network (PNN) [62] which combines some of the best attributes of statistical pattern recognition and feed forward neural networks. The PNN features very fast training time, offers robustness to noisy data and guaranteed convergence to a Bayesian classifier [15] providing given enough training

data. The architecture of the PNN is shown in Figure 6.2. It has a radial basis layer and a special competitive layer. When an input is presented, the first layer computes distances from the input vector to the training input vectors, and produces a vector whose elements indicate how close the input is to a training input.

The second layer (competitive layer) sums these contributions for each class of inputs to produce as its net output a vector of probabilities. Finally, the “**compete**” transfer function on the output of the second layer picks the maximum of these probabilities, and produces a 1 for that class and a 0 for the other classes. Due to the mentioned advantages the PNN based on radial basis networks was chosen for the implementation. All the PNNs used in this work were designed using MATLAB[®] neural network toolbox.

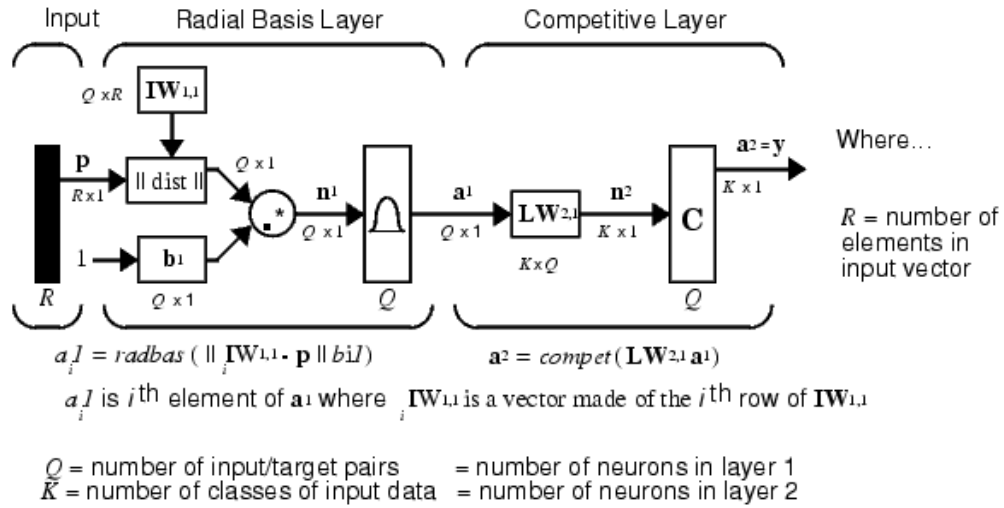


Figure 6.2: PNN architecture.

A novel class of artificial neural networks called, morphological associative memories (MAMs) [63, 64] were studied. They have the capability to retrieve complete stored patterns from noisy or incomplete input pattern keys. This is one of the most interesting characteristics of this type of ANNs. In MAMs the operations of multiplications and addition performed in the theory of ANNs are replaced by addition and maximum (or minimum) of sums, respectively. The network weights are computed

directly from the input/output values. Therefore convergence problems do not exist in this kind of networks. A MAM network and a PNN were compared based on their performance in recognizing noised data. According to the obtained results, PNNs showed to be more efficient than MAMs when both type erosive and dilative noise are present.

The data required for training the NNs is provided by numerical models. This information is preprocessed using MATLAB[®] routines. The preprocessing of the data involves two main stages: (1) the extraction of synthetic features related to the presence and the characteristics of the damage; (2) the normalization of the input patterns to improve convergence of the learning rule.

All the previous mentioned NNs are not designed to be incremental learners since old examples are represented explicitly in the networks. Every new example demands the modification of the network architecture by the addition of another pattern unit and associated connections. However once the NNs were properly trained, the weights and biases do not need to be recalculated when the network is used to classify a new input pattern.

6.3 Curvature Method

In chapter 3 we obtained the natural mode shapes for several damage scenarios using FE models. Then, the curvature mode shapes were computed and the difference with respect to the undamaged case was performed. Later, in chapter 5, the same procedure was followed for experimental mode shapes which were measured using modal testing. In both cases, the damage location was identified as peaks in the difference curvature mode shapes while the damage magnitude was estimated by means of the curvature normalization value. In this section, both structural features are used to train and test a PNN for damage predictions.

Since every curvature mode shape contains specific information related to the defect, they are processed separately by three different networks. Figure 6.3 shows the NN architecture developed for curvature data classification. Each PNN associates the input data to a predefined damage case (target). Predictions of PNN1, PNN2 and PNN3 are used as inputs to a fourth PNN (PNN4) which provides the ultimate opinion regarding damage location and size. PNN4 classifies the damage estimations a_1 ; a_2 ; and a_3 based on their probability of certainty (p_1 ; p_2 ; p_3). This means that if some of the estimates have a low probability of occurring, they will not affect the PNN4 prediction. The damage estimate with the highest probability dominates the PNN4 opinion. This probability must be inside a predefined threshold in order to be considered as a credible prediction.

For example if only one network predicts the damage a_i with the probability p_i , PNN4 will predict a damage a_i . If two networks estimate the same damage a_i with different probabilities p_i and p_j and the third network predicts a different damage a_k with a probability $p_k > p_i + p_j$, PNN4 will classify a damage a_k . On the other hand, if different damage scenarios are selected by PNN1, PNN2, and PNN3 the damage estimate with the highest probability will be chosen by PNN4 as the possible damage state. But if all the predictions are little probable, the case will be classify and labeled as undamaged. This architecture of NNs avoids false readings.

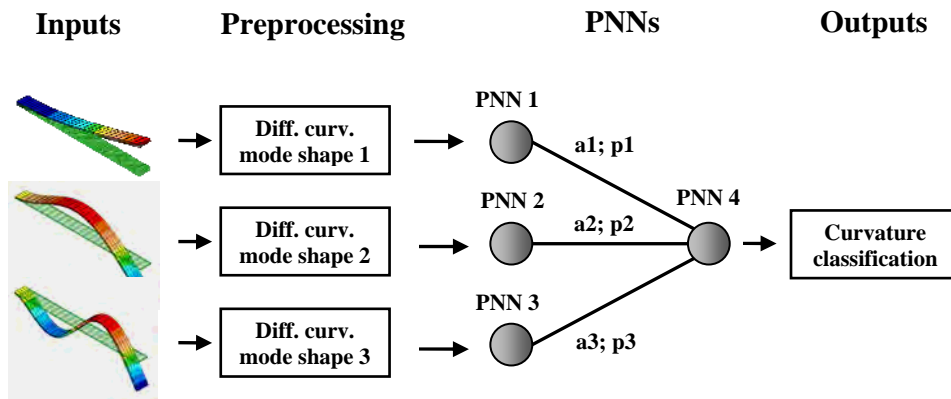


Figure 6.3: Scheme for NN curvature data classification.

6.3.1 Simple Damage Scenarios

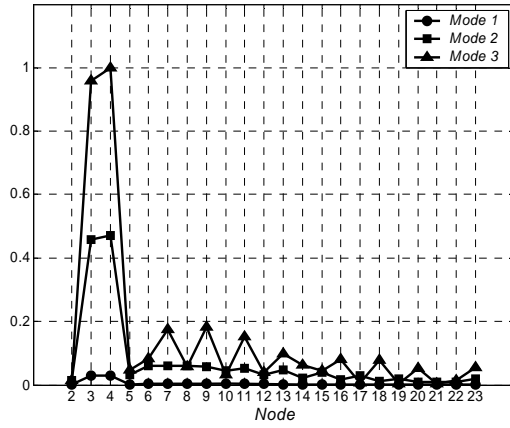
The simplest case of testing a NN involves classifying one of the training patterns and verifying that it has correctly associated it with the corresponding target. The NNs scheme of Figure 6.3 was trained using the data from damage cases listed in Table 6.1. These training cases correspond to simple damage scenarios simulated by the FE models of chapter 3. The curvature data for each case is plotted in Figure 6.4.

Several test cases were chosen to check the performance of the proposed NN architecture in damage detection. These include the numerical (N) and experimental (E) damage scenarios shown in Table 6.2. First, the NN system was fed with damage case N3 (Figure 6.5 a) and it was correctly associated with itself. This obvious result confirmed a priori that the NNs were properly trained. On the other hand, damage case N4 (Figure 6.5 b) was not used in the learning process. However, the NN system related this case to the closest learned damage scenario N5.

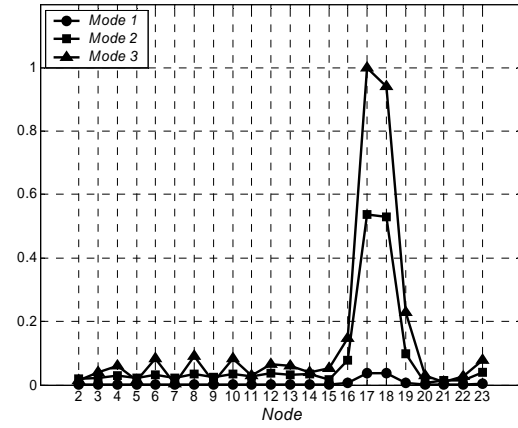
Table 6.1: Training with curvature damage scenarios.

Damage case	Type	Damage state	Size	Location
N1	Bond failure	Simple	1 x 2 in	Nodes 3 - 4
N2				Nodes 5 - 6
N3				Nodes 9 - 10
N5				Nodes 17 - 18
N8	Surface crack		0.75 in	Nodes 11 - 12
N9	Surface indentation		0.0625 in	Nodes 13 - 14

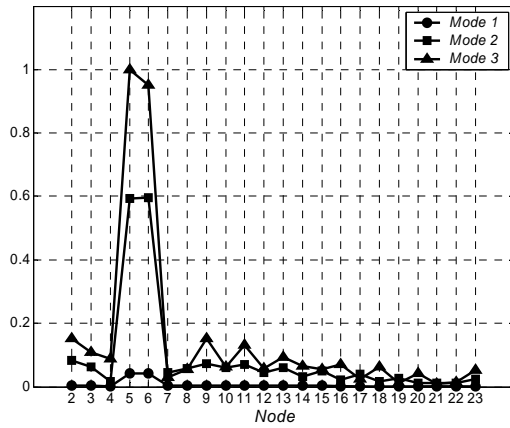
Cases N6 and N7 in Table 6.2 are multiple damage states and will be discussed in detail in the next section. Note that E1 and E2 are different types of failures but they have the same location as shown in Figure 6.5 c and d. However, both damages were associated to the same training case N2.



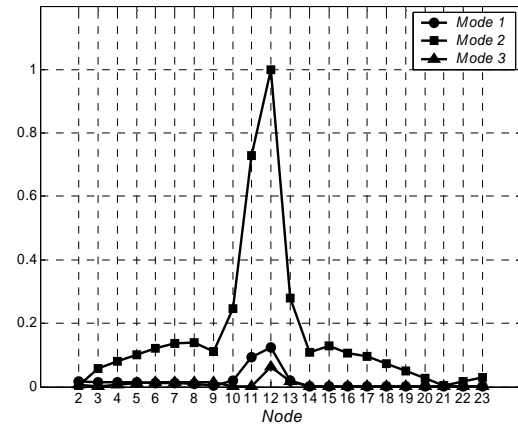
a) Damage N1.



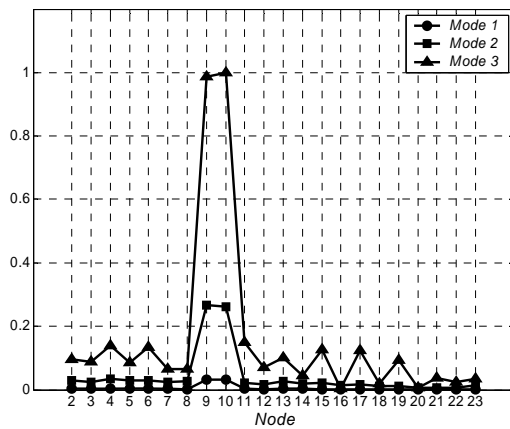
d) Damage N5.



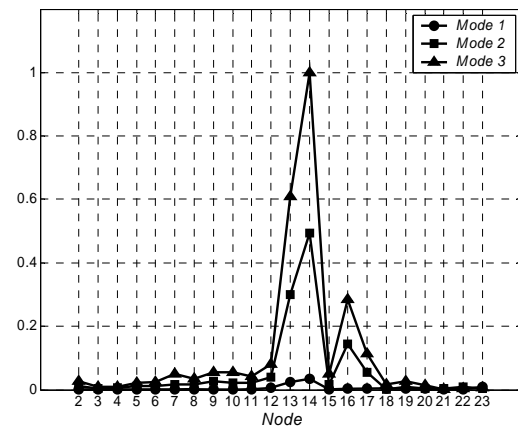
b) Damage N2.



e) Damage N8.

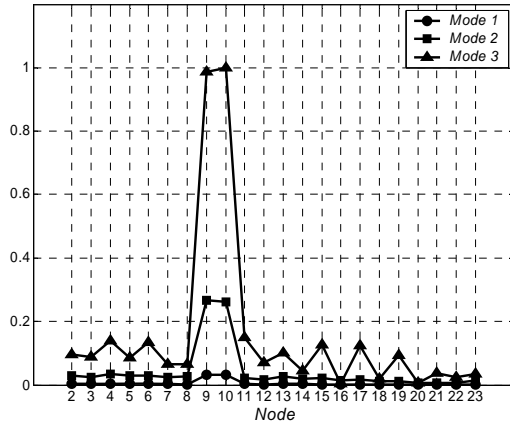


c) Damage N3.

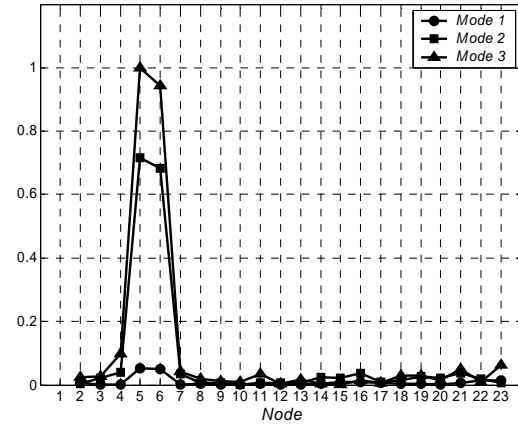


f) Damage N9.

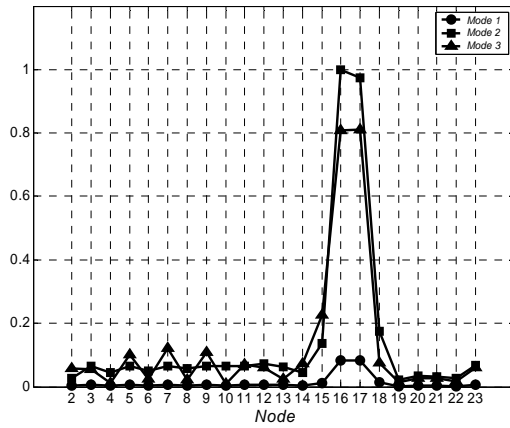
Figure 6.4. NN curvature training data: a); b); c) and d) bond failures; e) crack; f) indentation.



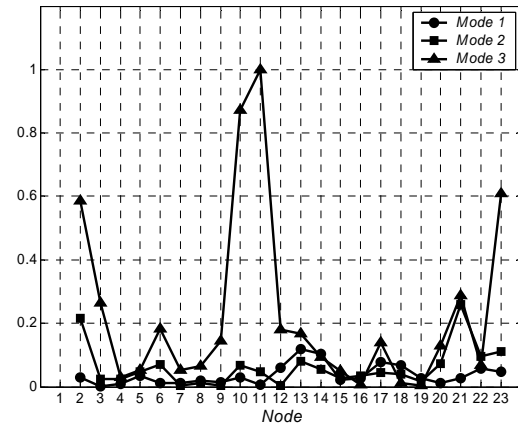
a) Damage N3.



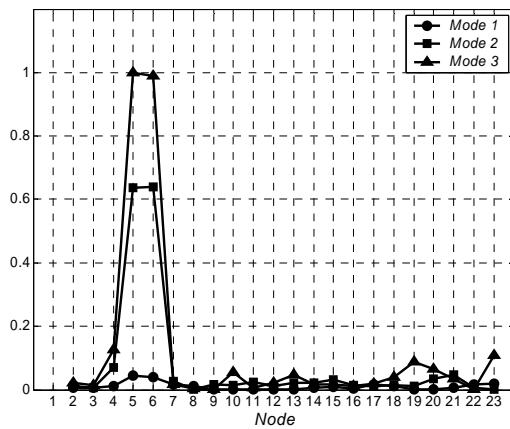
d) Damage E2.



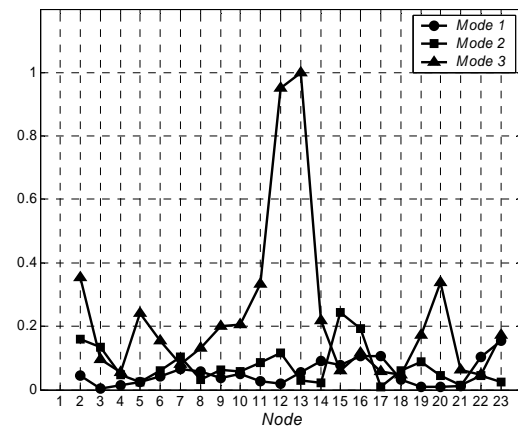
b) Damage N4.



e) Damage E3.



c) Damage E1.



f) Damage E4.

Figure 6.5. NN curvature test data: a); b); c); and e) bond failures; d) core failure; f) crack.

This means that the location of the peaks in the curvature mode shapes is the most significant feature when classifying by the NNs scheme. All the simulations results are summarized in Table 6.2.

Table 6.2: Results from curvature test damage cases.

Input case	Type	Damage state	Size	Location	Assoc. case
N3	Bond failure	Simple	1 x 2 in	Nodes 9 - 10	N3
N4				Nodes 16 - 17	N5
N6		Multiple		Nodes 3 - 4; 9 - 10	N1; N3
N7				Nodes 5 - 6; 16 - 17	N2; N5
E1		Simple	Nodes 5 - 6	N2	
E3			0.375 x 2 in	Node 11	N3
E2	Core failure		1 x 2 x 0.0625 in	Nodes 5 - 6	N2
E4	Surface crack		0.75 in	Nodes 12 - 13	N9

Because case E3 corresponds to a very small bond failure; the data obtained (Figure 6.5 e) does not accurately characterize the damage location. Curvature mode shapes 3 shows a peak at the damage location while curvature mode shape 1 and 2 were unable to predict the defect site. However E3 was related to damage case N3. The same effect can be observed in Figure 6.5 f for the case E4 which represents a surface crack. In this case curvature mode shapes 1 and 2 did not peak the damage location Thus, the NNs system connected E4 to damage case N9. These two cases prove that the NNs system can classify correctly the data using one curvature mode shape.

6.3.2 Multiple Damages Scenarios

As described in section 3.6.2, when the structure contains two or more damages at the same time, several peaks occur simultaneously in the curvature difference. These peaks are related to a particular damage location through the training data. Therefore in order to

detect all the damages in the structure, multi damage states are broken into single damage states before being analyzed by the NN. The linear behavior of the structure under small vibrations allows using of the principle of superposition. A mean based criterion was used to identify the maximum values on curvature differences.

To show how this technique works, we will study the multiple damage cases N6 and N7 from the previous section. Figure 6.6 shows the curvature data of case N6. Note that the difference in curvature for mode shapes 3 peaks at two different locations while for the curvature mode shape 2 there is a single maximum (nodes 3 - 4). In addition, it is required that the input data to the PNN4 (a_1 ; a_2 ; a_3) have the same size. In other words, PNN1, PNN2 and PNN3 must process patterns with the same amount of data for a specific damage case. For example if one mode shows 2 peaks and another mode shows only one peak, two curves need to be produced for each mode.

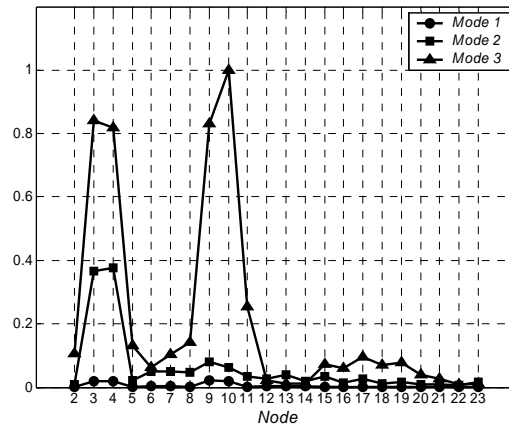
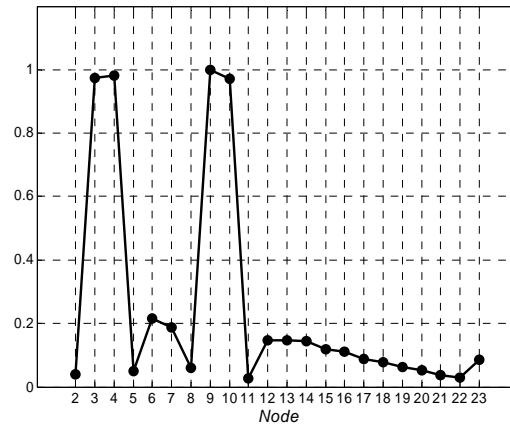
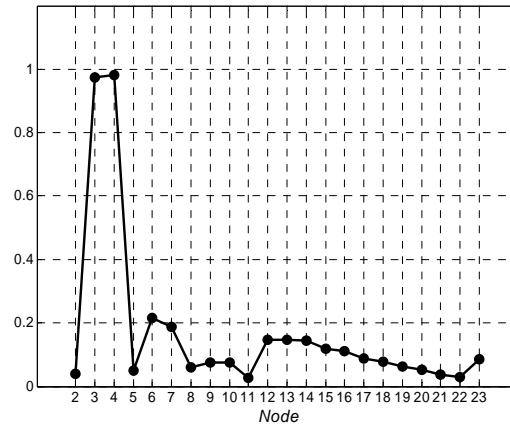


Figure 6.6: Multiple damages case N6.

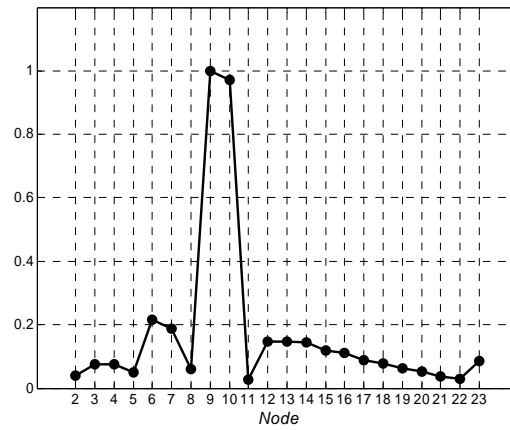
Therefore the number of curves will be equal to the largest number of peaks in the curvature mode shape difference. Figures 6.7 - 6.9 show that two single peaks were extracted from each curvature mode shape. To extract the second peak from Figure 6.8 a this method simulates the existence of a maximum in the location were it actually occurs in the test data (Figures 6.7 a and Figures 6.9 a). For the test scenarios presented in this section the NN system was trained with the curvature data of Figures 6.4.



a) Curvature peaks - Mode 1.

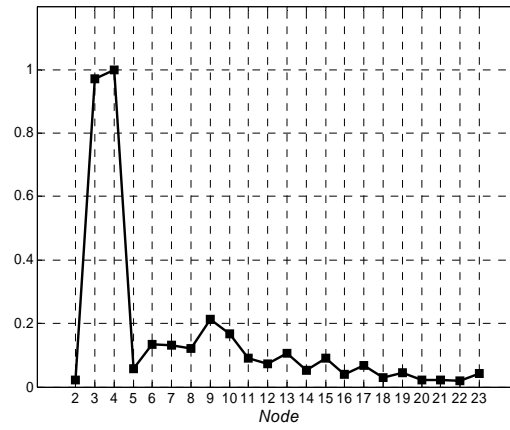


b) Curvature peak 1.

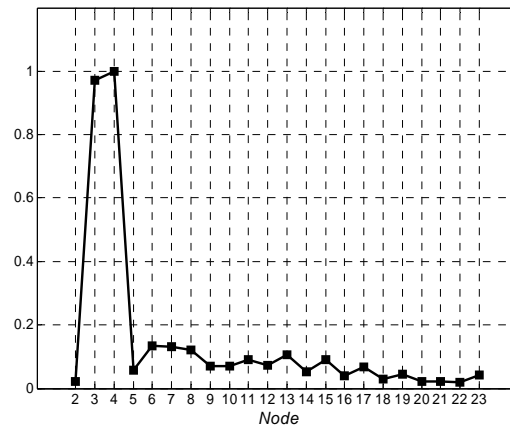


c) Curvature peak 2.

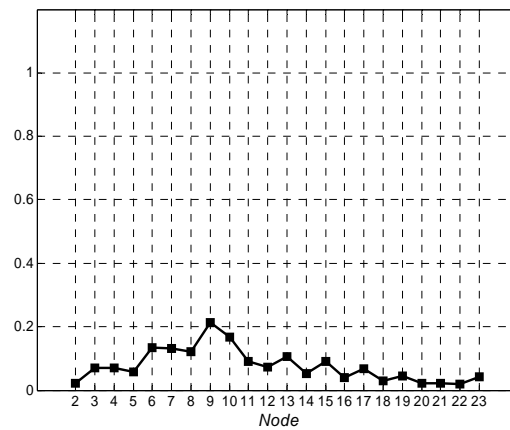
Figure 6.7. Damage case N6: Curvature peaks - Mode 1.



a) Curvature peaks - Mode 2.

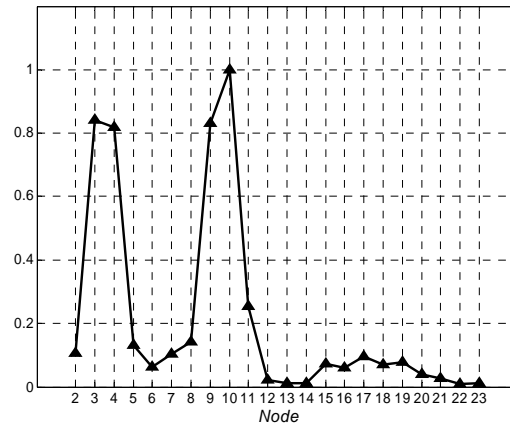


b) Curvature peak 1.

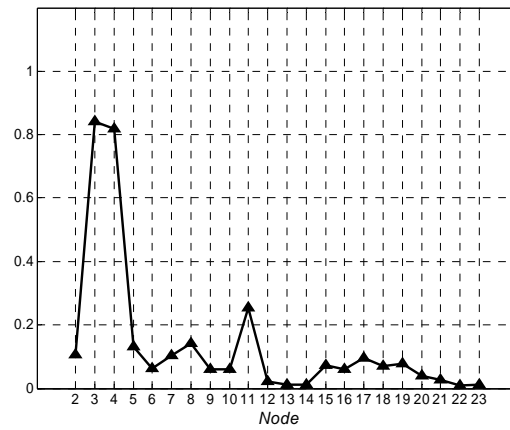


c) Curvature peak 2.

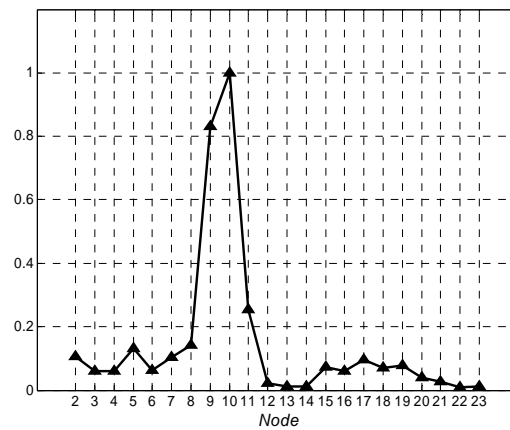
Figure 6.8. Damage case N6: Curvature peaks - Mode 2.



a) Curvature peaks - Mode 3.



b) Curvature peak 1.



c) Curvature peak 2.

Figure 6.9. Damage case N6: Curvature peaks - Mode 3.

The damage predictions were listed in Table 6.2. The case N6 was related to the training cases N1 and N3. This result is correct as expected since damage case N6 is a combination of cases N1 and N3. A similar situation occurs for damage case N7 (Figure 6.10). Figures 6.11 - 6.13 show the peaks extracted from each curvature mode shape. In this case the three curves peak at two different locations (nodes 5 - 6 and nodes 16 - 17). Because of case N7 was created based on cases N2 and N4, it was associated with the training cases N2 and N5. Remember that the single damage case N4 was connected to N5 when tested in the previous section.

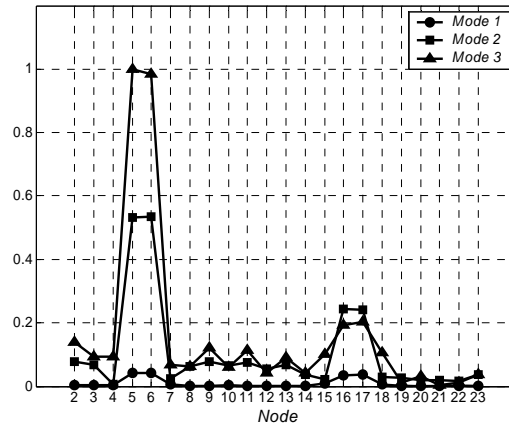
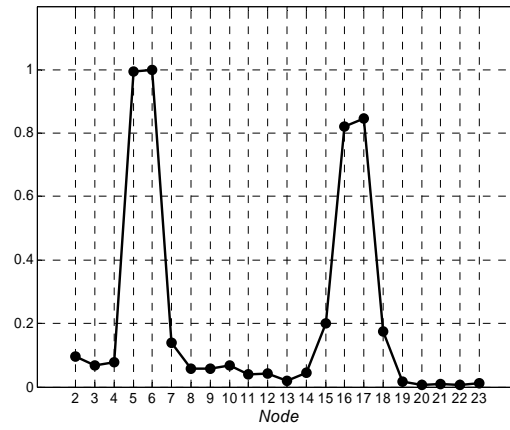


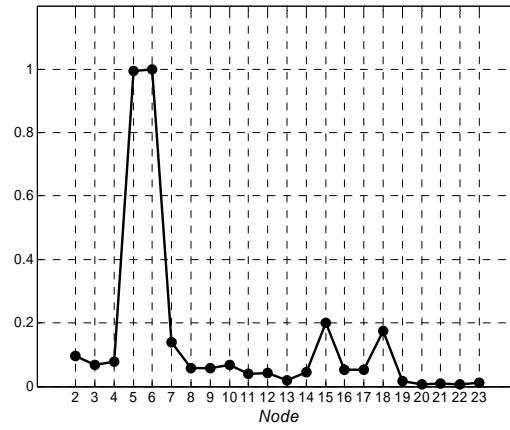
Figure 6.10: Multiple damages case N7.

It is important to mention that if the three curvatures have only one maximum each, the peaks extraction method does not modify the curvature data. This particular characteristic makes this procedure suitable for real application where, in most cases, structures may contain several defects at the same time.

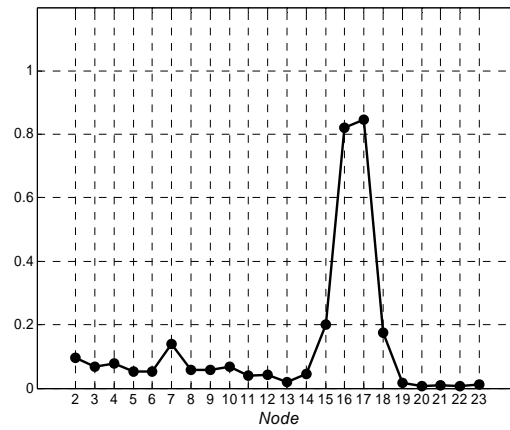
In the damage cases where the NN curvature approach fails to detect the damaged locations or its predictions have low probability of being correct, the NN thermal method can be used. As will be discussed in the next section, the thermal approach is suitable for small and surface damages, where the curvature approach may fail.



a) Curvature peaks - Mode 1.

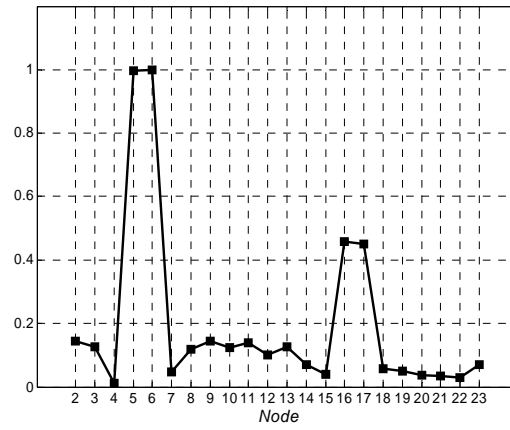


b) Curvature peak 1.

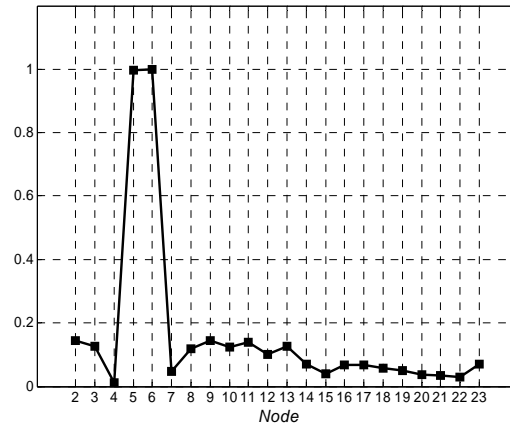


c) Curvature peak 2.

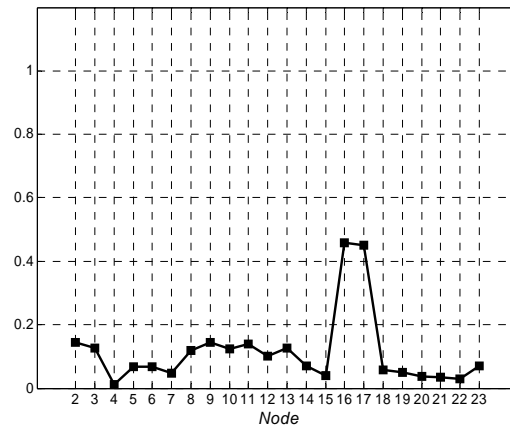
Figure 6.11. Damage case N7: Curvature peaks - Mode 1.



a) Curvature peaks - Mode 2.

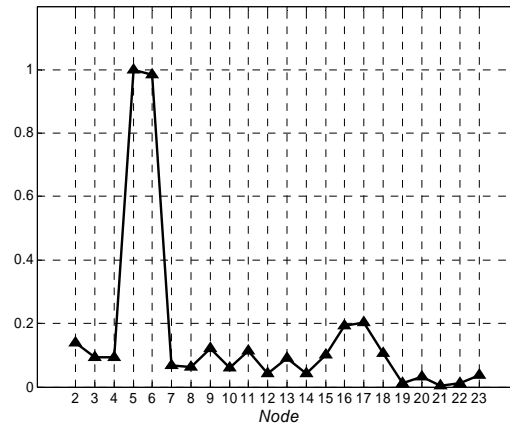


b) Curvature peak 1.

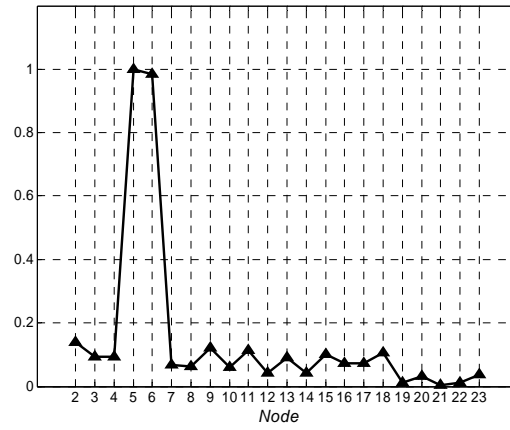


c) Curvature peak 2.

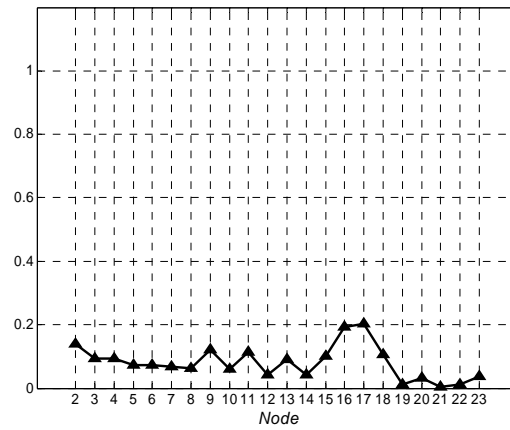
Figure 6.12. Damage case N7: Curvature peaks - Mode 2.



a) Curvature peaks - Mode 3.



b) Curvature peak 1.



c) Curvature peak 2.

Figure 6.13. Damage case N7: Curvature peaks - Mode 3.

6.4 Thermal Method

Algorithms mentioned in chapter 1 have been used in the process of interpreting thermographic images. In this section we will use a NN based algorithm to identify anomalies present in thermal images. These include: numerical solutions provided by finite volume (FV) models from chapter 3 and thermal transient measurements presented in chapter 5. In both cases, most of the information contained in the images is useless for anomaly identification. Therefore, features extraction techniques were used, which retain the relevant information. Figure 6.10 shows the pre-processing of an IR thermal image.

First the original images were cropped (Figure 6.14 b) and converted to grayscale (Figure 6.14 c) by eliminating the hue and saturation information while maintaining the luminance. Then, 2D adaptive noise removal filtering was performed (Figure 6.14 d). Later an edge extraction procedure based on image gradient computation was used resulting in a set of binary images (Figure 6.14 e). Each contour of these images was plotted as a single curve (Figure 6.14 f).

Three geometrical properties were calculated for every curve: centroid and moments of inertia respect to a pair of axis placed at the centroid. The first property indicates approximately the location of the contour in the image while the moments of inertia are related to the size and shape of the contour. A big contour centered in the image will probably correspond to a normal isotherm. On the other hand, a small contour could be associated with a surface defect.

Thus each thermal image is characterized by a set of geometrical features. In this case a unique PNN is used for contour classification (Figure 6.15). Each feature of a test image is compared with a contours data base and classified as normal or anomalous. This classification is based on numerical cases learned which were presented in chapter 4.

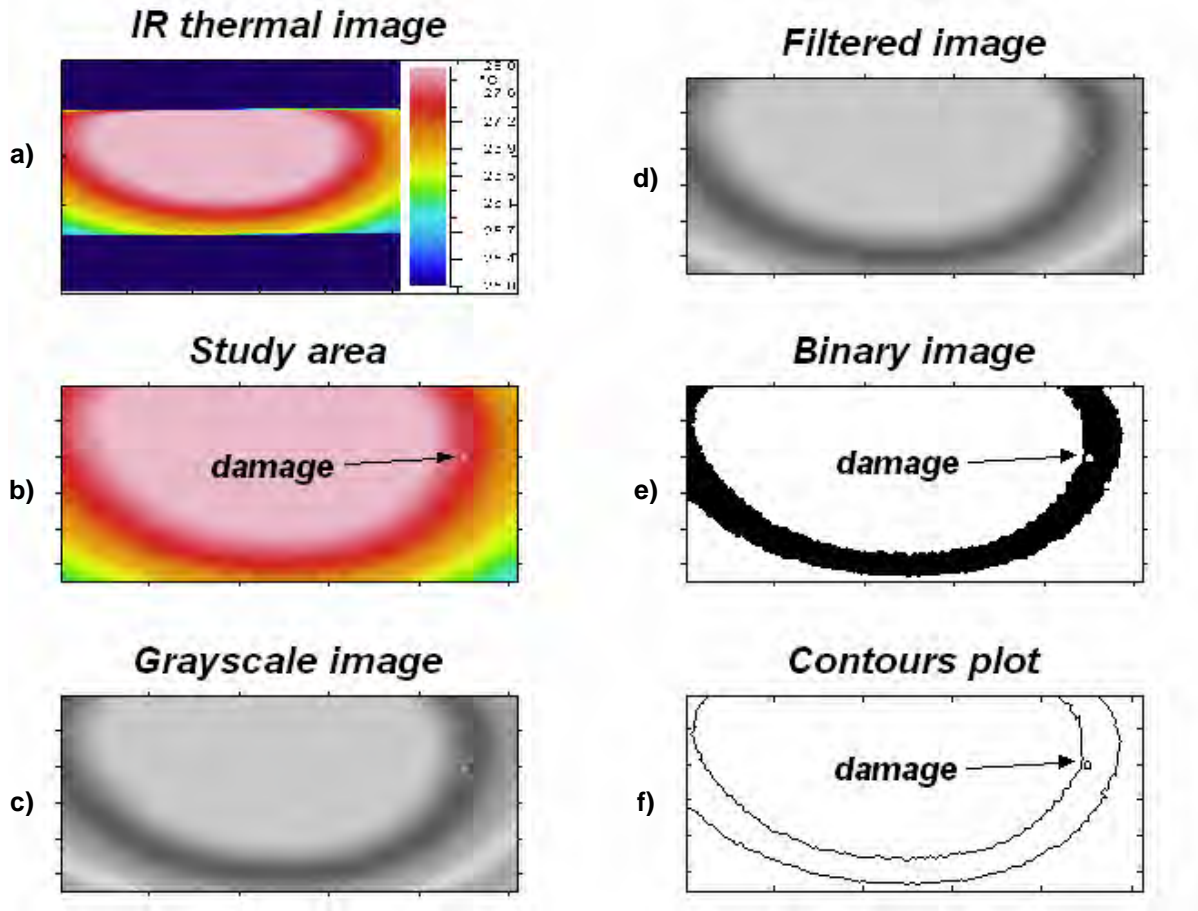


Figure 6.14: Pre processing scheme of IR thermal image.

Note that this approach does not require the knowledge of the undamaged case. Usually, any surface defect can be seen as a hot spot in the thermal distribution. However, as shown in chapter 5, not all the thermal images provided clear evidence of the damage at a particular time. This effect was related to both the time the image was taken and the relative position of the damage with respect to the heated zone. Therefore, the NN algorithm was designed to determine location and size of the defects from the temporal and spatial thermal distributions.

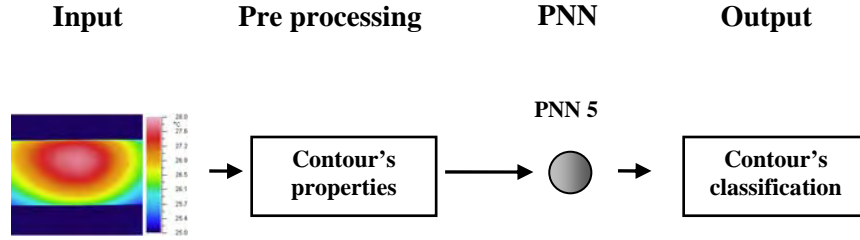


Figure 6.15: NN scheme for thermal data classification.

6.4.1 Simple Damage Scenarios

PNN5 was trained using the information of damage cases shown in Figure 6.16. All the training data corresponds to simple damage states provided by FV models. While some of these damage cases were studied in chapter 4, others were created specially for the training of PNN5. These include surface indentations at different locations and surface cracks. The contours were extracted from these thermal images by using the technique described in the previous section and shown in Figure 6.17. Each contour was labeled with the letter ***T*** (training) and a number from 1 to 56 for identification. Then they were used to train PNN5. Table 6.3 summarizes the training data. The notation with bold font corresponds to the damage contours.

As in the curvature approach, numerical (N) and experimental (E) damage scenarios were tested. The FV results of Figure 6.18 a, b and c (N9; N10; and N11) correspond to a single indentation, a surface crack and multiple (two) indentations. Damage case N11 (Figure 6.18 c) is a multiple damage scenario which will be discussed in the next section. The thermal measurements shown in Figure 6.18 d, e and f (E1; E2; and E3) belong to three artificial face sheet indentations. The word artificial means that the damages were introduced in the specimens in the lab under controlled conditions.

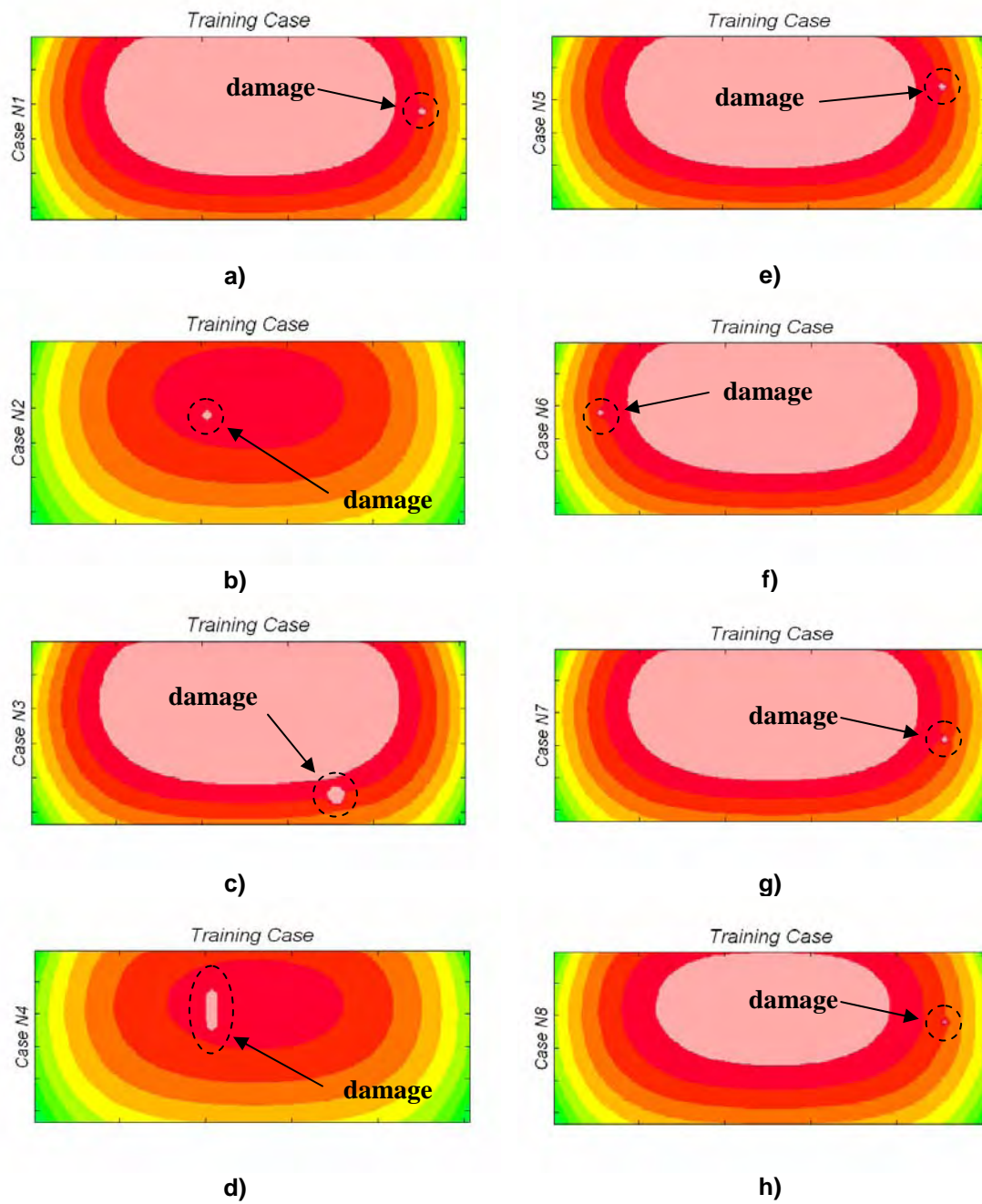


Figure 6.16. NN thermal training data: a) indentation 15 sec.; b) idem 50 sec.; c) notch 10 sec.; d) crack 55 sec.; e) indentation 15 sec.; f) idem; g) idem; h) idem 35 sec.

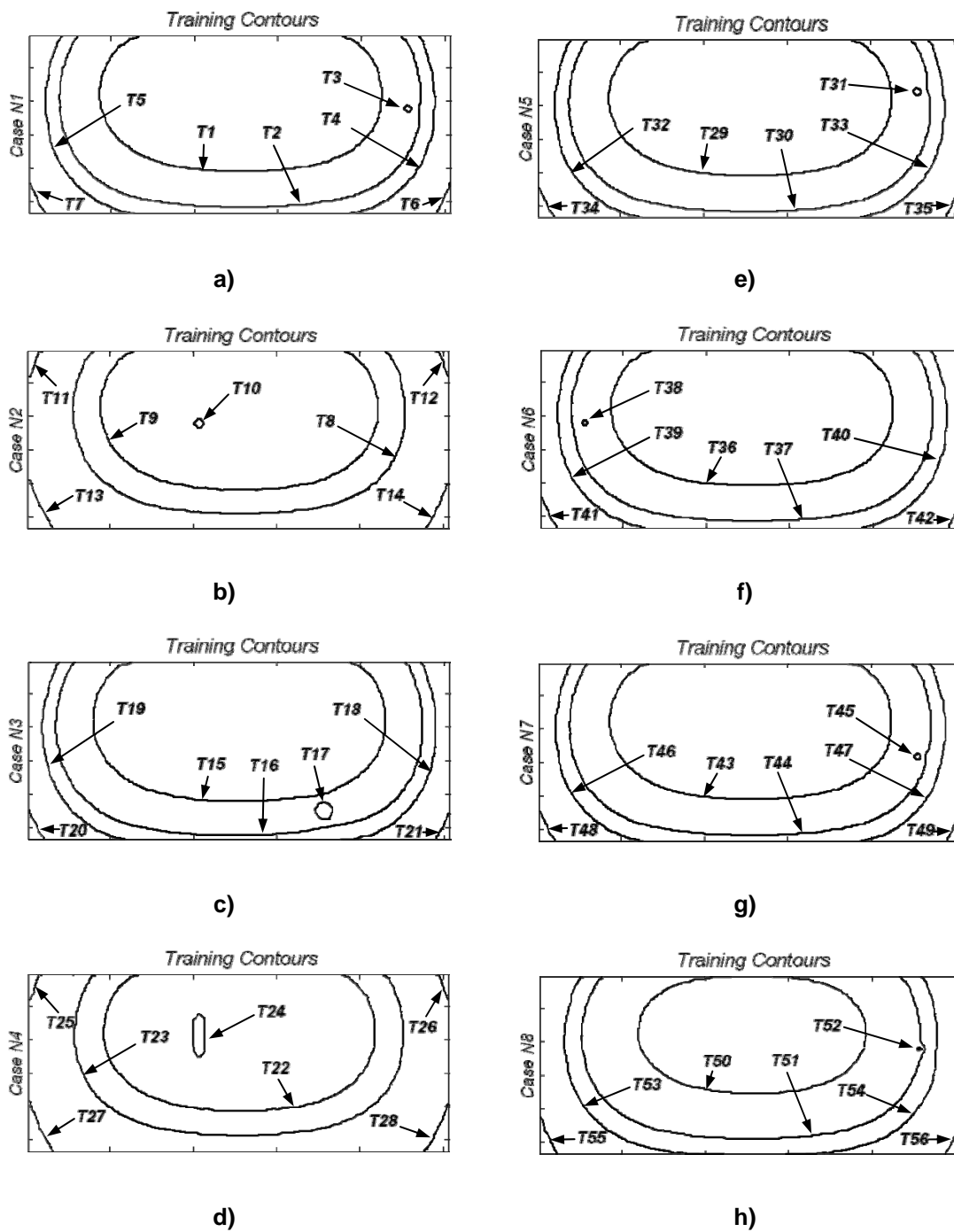


Figure 6.17. NN training contours: a) indentation 15 sec.; b) idem 50 sec.; c) notch 10 sec.; d) crack 55 sec.; e) indentation 15 sec.; f) idem; g) idem; h) idem 35 sec.

The features were labeled with the letter *S* (simulated) and a number from 1 to 18 as shown in Figure 6.19. Each one of these features was analyzed separately by the PNN5. First it discriminates between two types of contours: regular and possible damage contour. Then, if the contour being analyzed belongs to the second type, PNN5 matches it with the closest contour based on the training data.

The results from NN are listed in Table 6.4. Note that the NN successfully classified the normal contours for all the testing cases. With respect to the damage contours, *S3* was associated with *T3* which has similar location but correspond to different times (30 and 15 sec. respectively). *S5* and *T24* are the same damage type but they are also related to different times (50 and 55 sec. respectively). The measured contours *S12* and *S15* are the same damage at 15 and 30 sec. respectively. Both cases were associated with feature *T52*, which corresponds to the same damage obtained numerically.

Table 6.3: Training with thermal damage scenarios.

Damage case	Type	Damage state	Size	Contours
N1	Surface indentation	Simple	0.0625 in	T1; T2; T3 ; T4; T5; T6; T7
N2				T8; T9; T10 ; T11; T12; T13; T14
N3			0.125 in	T15; T16; T17 ; T18; T19; T20; T21
N4	Surface crack		0.75 in	T22; T23; T24 ; T25; T26; T27; T28
N5	Surface indentation		0.0625 in	T29; T30; T31 ; T32; T33; T34; T35
N6				T36; T37; T38 ; T39; T40; T41; T42
N7				T43; T44; T45 ; T46; T47; T48; T49
N8				T50; T51; T52 ; T53; T54; T55; T56

Finally, the contour *S18* was related to *T10* which corresponds to the same damage obtained numerically. As the NNs used for curvature data classification, the PNN5's predictions are based on the probability that the input pattern being classified is a training case.

If this probability is inside a predefined threshold, the prediction is considered credible; if not the classification is related to a default non-damage case. This architecture avoids false damage detections. Although the results obtained showed that the PNN5 successfully associated the test cases with those used in the training, the NN performance can be improved by increasing the number of training cases.

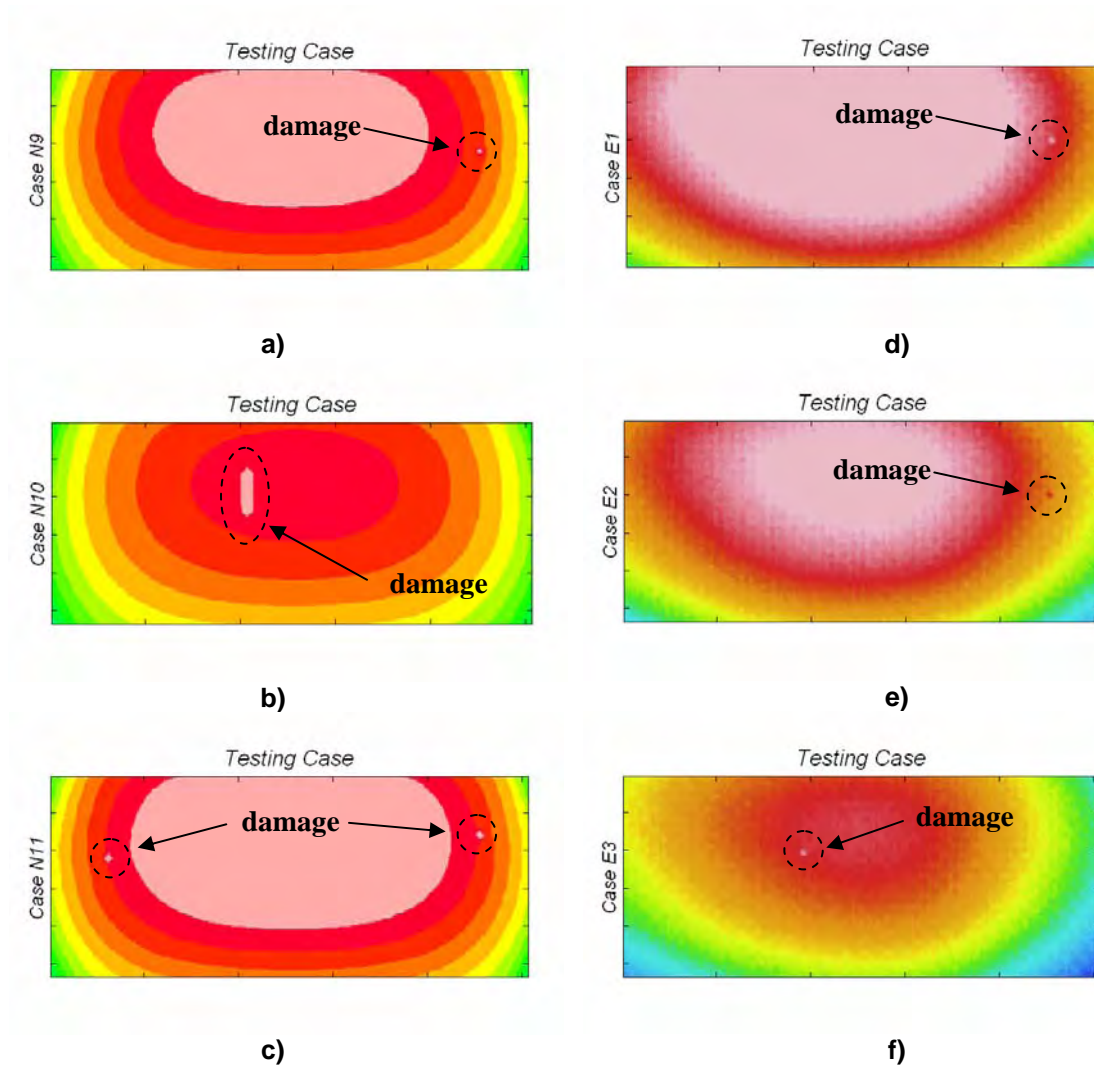


Figure 6.18. NN thermal test data: a) indentation 30 sec.; b) crack 50sec.; c) indentations 15 sec.; d) indentation 15 sec.; e) idem 30 sec.; f) idem 50 sec.

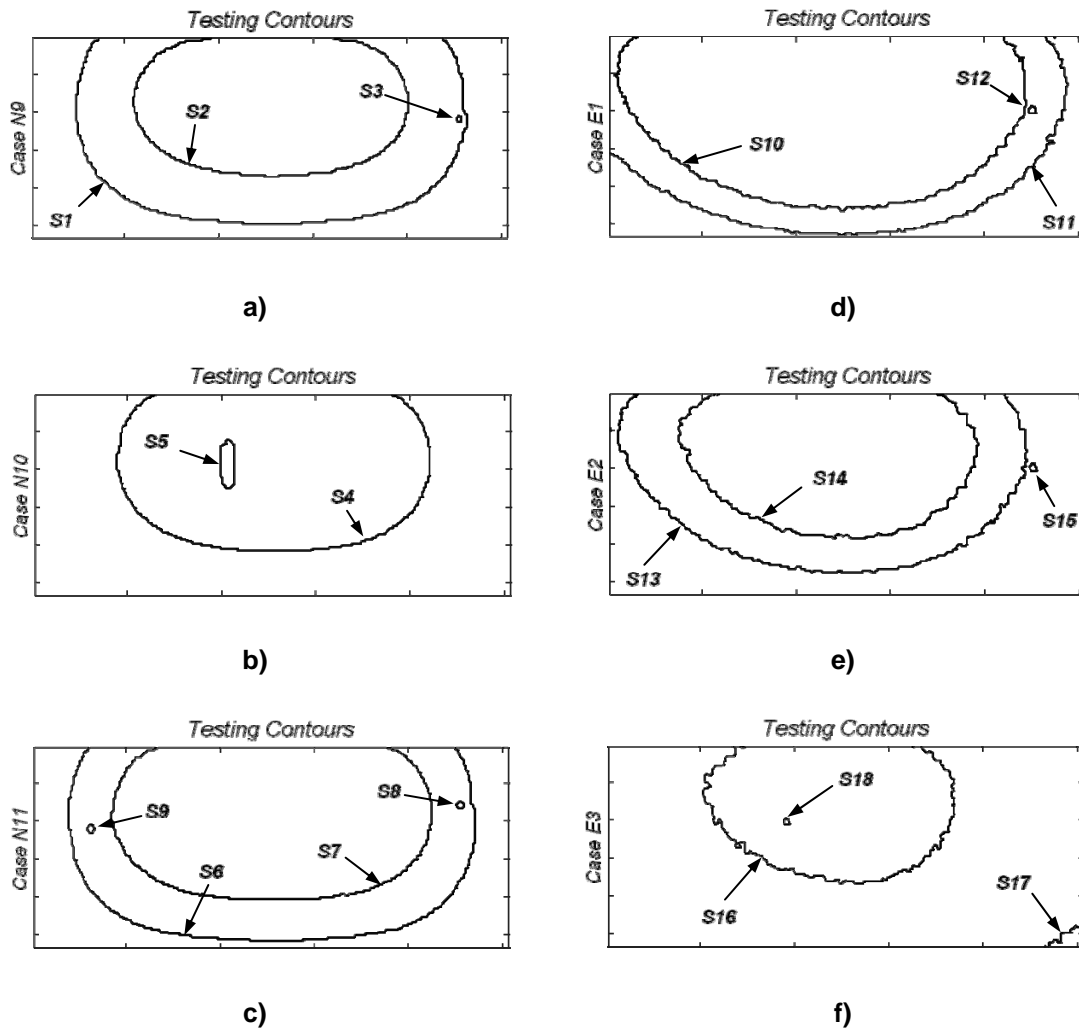


Figure 6.19. NN test contours: a) indentation 30 sec.; b) crack 50sec.; c) indentations 15 sec.; d) indentation 15 sec.; e) idem 30 sec.; f) idem 50 sec.

Table 6.4: Results from thermal test damage cases.

Input case	Type	Damage state	Size	Features	Associated feature
N9	Surface indentation	Simple	0.0625 in	S1; S2; S3	T51; T50; T3
N10	Surface crack		0.75 in	S4; S5	T9; T24
N11	Surface indentation	Multiple	0.0625 in	S6; S7; S8; S9	T30; T1; T31; T38
E1		Simple	0.0625 in	S10; S11; S12	T51; T51; T52
E2				S13; S14; S15	T51; 15; T52
E3				S16; S17; S18	T50, T21; T10

6.4.2 Multiple Damage Scenarios

An important consideration is what happens when a multiple damage scenario occurs. How will the NN classify this case if it was trained only with simple damage cases? To answer this question, the same procedure was applied using a two damage scenario. Two indentations similar to that in the previous cases were created in a FV model. The test case N11 of Figure 6.18 c shows two hot spots on both sides of the heated zone. Similarly, two damage contours (*S8* and *S9*) were obtained when applying the feature extraction technique (Figure 6.19 c). Because of the training cases N5 and N6 (Figure 6.16 e and f) contain damages placed near to those in N11; *S8* and *S9* were associated to *T31* and *T38* respectively. Thus, a single input image containing two damages was associated with two different cases used in the training of the NN. This flexible characteristic of the transient thermal method makes it suitable for real implementation where multiple damages scenarios may be common.

6.5 Curvature and Thermal Approaches Together

Since curvature and thermal analyses have their own limitations, the NN performance in damage detection can be improved by complementing those methods. Thus, the previous curvature and thermal data classifications are used as inputs to a new PNN which provides the final verdict about the presence and the location of damages. Therefore, a combined NN approach for damage detection is proposed. Figure 6.20 shows schematically the PNN arrangement and the flow of the information.

First, the input data is separated according to the native format used to store the information: xls for curvature measurements and image format (bmp, jpeg, and tiff) for IR thermal images. Then the data is preprocessed in order to extract the corresponding features; difference in curvature mode shapes and contour plots. After these features are classified, both approaches provide their own damage prediction.

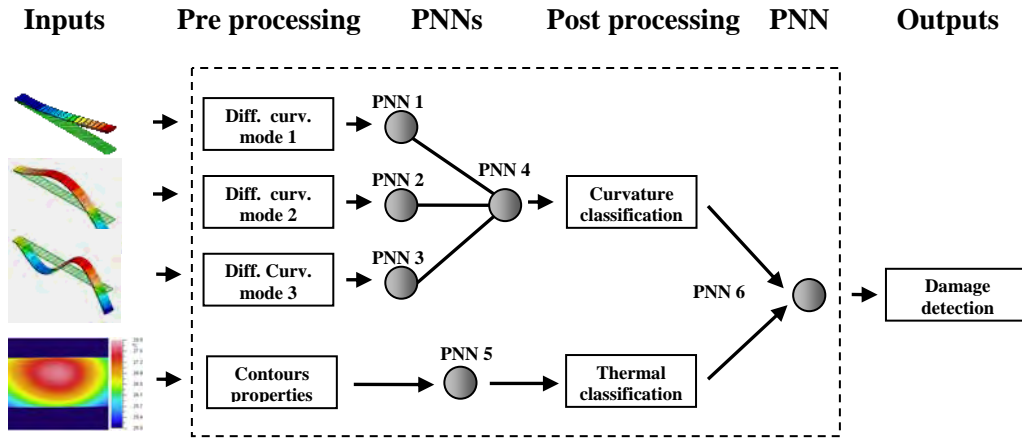


Figure 6.20: General NN approach for damage detection.

Depending on the type, size and location of the damages in the structure, three different situations can occur: both methods agree about the damage case, the two techniques make different predictions or none approach is able to identify the defect. To deal with this problem, PNN6 was designed to distinguish among the previous three situations. The output damage cases of the PNN4 and PNN5 are identified by the labels used in the training of the NNs. For example for the curvature data classification six damage scenarios were used which were labeled as N1; N2; N3; N5; N8; and N9. Depending on the input pattern being classified, the output of the PNN4 is one or more of these six labels. If the structure being monitored is not damaged, a special identifier is used to label this case (N0). A similar situation occurs with the thermal data classification. Based on these labels PNN6 decides if the damage cases associated by PNN4 and PNN5 are the same damage in the structure or each NN detected a different damage. In such a case both predictions are assumed to be correct and the state of the structure is labeled as a multiple damage case. When one of the two methods does not associate any damage with the input data and the other does, the corresponding damage case is assumed to be correct. If none technique identify the defect, PNN6 classifies the case as undamaged. Actually, the output of PNN6 is a set of labels which indicate the possible damages present in the structure based on both vibration and thermal training cases.

Chapter 7

Conclusions and Future Work

An experimentally validated ANNs damage detection system for location and severity predictions of damage in sandwich composite structures was developed. The system analyzes and classifies features extracted from vibration and thermal analysis. Several numerical models of sandwich composite structures with different type of defects were used to generate damage scenarios to train the ANNs. The ANNs system was later employed to classify measured data. The selection of the PNN architecture was based on its performance in pattern recognition. This ANN model belongs to the Bayesian classifiers. The processing system was tested and optimized on the numerical data, before final application to real experimental results. The issues that were resolved in this thesis are summarized in the topics stated below:

7. Modal testing and IR thermography were selected to investigate critical changes in structural parameters.
8. PNN architecture was proved to be the most efficient architecture for the measured data classification.
9. Two different features extraction techniques were used in order to retain the relevant information from the experimental data before the NN implementation: differences in curvature mode shapes and thermal contours.
10. Numerical models were created and validated with experimental measurements to generate several damage scenarios. The simulated responses were used in the ANNs training.
11. A combined ANNs approach which is able to deal with data provided by modal and thermal analysis was developed for damage predictions.
12. Finally, experimental results were used to demonstrate the capability of the proposed approach in detecting real damage cases.

According to the results presented in this work, we can conclude that the difference in curvature mode shapes and thermal transient responses provide necessary information for the existence and severity of the damage. In addition, the ANNs predictions successfully identified the damage location for both simple and multiple damage states. This particular characteristic makes the proposed damage detection system suitable for real applications where multiple damages scenarios are quite common.

However, the PNN model was not designed to be incremental learners since old examples are represented explicitly in the networks. Every new example demands the modification of the network architecture by the addition of another pattern unit and associated connections. Therefore, an incremental learning rule will be investigated in order to optimize the ANN training process and to minimize the run time of the classification algorithm.

In addition, both vibration and transient thermal response of more complex structures will be studied. Thus, the analysis of different types of mode of vibrations (flexural, torsional, longitudinal, etc.) will be required. Conversely to the difference in curvature mode shapes used in this work, a new feature which does not include the undamaged state of the structure will be investigated in order to make the damage detection approach more autonomous.

References

- [1] M. S. Agbabian, and S. F. Masri, 1988 *Proc. Int. Workshop on Nondestructive Evaluation for Perf. Of Civ. Struct. Publ. No. M8805*. Civ. Eng. Dept., University of Southern California, Los Angeles.
- [2] M. Sahin and R. A. Shenoi, 2003 *Engineering Structures* **25**, 1785-1802. Quantification and Localization of Damage in Beam like Structures by Using Artificial Neural Networks with Experimental Validation.
- [3] S. F. Masri, A. G. Chassiakos and T. K. Caughey, 1993 *J. of Appl. Mech. Trans., ASME* **60**, 123-133. Identification of Nonlinear Dynamic Systems Using Neural Networks.
- [4] G. W. Housner, 1997 *J. Eng. Mech., ASCE* **123(9)**, 897-971. Structural Control: Past, Present and Future.
- [5] M. F. Elkordy, K. C. Chang and G. C. Lee, 1993 *J Comp. in Civ. Eng., Trans., ASCE* **7(2)**, 130-145. Neural Networks Trained by Analytically Simulated Damage State.
- [6] J. Ghaboussi, J. H. Garret and X. Wu 1991 *J. Eng. Mech., Trans., ASCE* **117(1)**, 132-153. Knowledge Based Modeling of Material Behavior with Neural Networks.
- [7] J. Ghaboussi and M. R. Banan 1994 *SAE Tech. Paper 94116, 45th Annu. Earthmoving Ind. Conf. Peoria, Ill.* Neural Networks in Engineering Diagnostics.
- [8] S. Wu, J. Ghaboussi and J. H. Garret Jr. 1992 *Comp. and Struct.*, **42(4)**, 649-659. Use of Neural Networks in etction os structural Damage.
- [9] Bhagi, PurnaChnadra Rao, Saarland University, Saarbruecken, Germany. Introduction to Nondestructive Testing.
- [10] S. S. Kessler and S. M. Spearing, *Department of Aeronautics and Astronautics, Massachusetts Institute of Technology, Cambridge, MA, USA*. Structural Health Monitoring of Composite Materials Using Piezoelectric Sensors.
- [11] C. Zang and M. Imregun, 2000 *Archive of Applied Mechanics* **71**, 525-536. Combined Neural Network and Reduced FRF Techniques for Slight Damage Detection Using Measured Response Data.

- [12] Z. Hou, M. Noori and R. St. Amand, 2000 *Journal of Engineering Mechanics* **126(7)**, 677-683. Wavelet Based Approach for Structural Damage Detection.
- [13] S. H. Liao, 2004 *Expert Systems with Applications* **28**, 93-103. Expert Systems Methodologies and Applications, a decade review from 1995 to 2004.
- [14] J. P. Sawyer and S. S. Rao, 2000 *AIAA Journal* **38(12)**, 2328-2335. Structural Damage Detection and Identification Using Fuzzy Logic.
- [15] C. M. Bishop, Neural Networks for Pattern Recognition, OXFORD University Press, NY, 2004.
- [16] H. G. Allen, Analysis and Design of Structural sandwich Panels, Pergamon Press, Oxford, NY, 1969.
- [17] B. D. Agarwal and L. J. Broutman, Analysis and Performance of Fiber Composites, 2nd. Edition, J. Wiley & Sons, Inc., NY, 1990.
- [18] K. Pandey, M. Biswas and M. M. Samman, 1991 *Journal of Sound and Vibration* **145**, 321-332. Damage Detection from Changes in Curvature Mode Shapes.
- [19] P. Cawley and R. D. Adams 1979 *Journal of Strain Analysis* **14(2)**, 49-57. The Location of Defects in Structures from Measurements of Natural Frequencies.
- [20] C. P. Ratcliffe and W. J. Bagaria, 1998 *AIAA Journal* **36(6)**, 1074-1077. A Vibration Technique for Locating Delamination in a Composite Beam.
- [21] C. P. Ratcliffe, 1997 *Journal of Sound and Vibrations* **204(3)**, 505-517. Damage Detection Using a Modified Laplacian Operator on Mode Shape Data.
- [22] J. Zhao, J. N. Ivan and J. T. DeWolf, 1998 *Journal of Infrastructure Systems* **4**, 93-101. Structural Damage Detection Using Artificial Neural Networks.
- [23] O. Byon (G. Ben) and Y. Nishi, 1998 *Key Engineering Materials* **141-143**, 55-64. Damage Identification of CFRP Laminated Cantilever Beam by Using Neural Network.
- [24] C. Toro, B. Shafiq, D. Serrano, F. Just, 2003 *Sixth International Conference on sandwich structures*. Application of Neural Networks to Eigen-Parameter Based Damage Detection in Multi-Component Sandwich Ship Hull Structures.

- [25] M. Sahin and R. A. Shenoi, 2003 *Journal of Mechanical Engineering Science* **217** Part C. Vibration Based Damage Identification in Beam like Composite Laminates by Using Artificial Neural Networks.
- [26] M. Sahin and R. A. Shenoi, 2003 *Engineering Structures* **25**, 1785-1802. Quantification and Localization of Damage in Beam like Structures by Using Artificial Neural Networks with Experimental Validation.
- [27] S. S. Kessler, S. M. Spearing, M. J. Atalla and C. E. Cesnik, Department of Aeronautics and Aeronautics, Massachusetts Institute of Technology, Cambridge, MA, USA. Constantinos Soutis, Department of Aeronautics, Imperial College of Science Technology and Medicine, London, UK. Damage Detection in Composite Materials Using Frequency Response Methods.
- [28] S. F. Masri, M. Nakamura, A. G. Chassiakos and T. K. Caughey, 1996 *Journal of Engineering Mechanics* **122**, 350-360. Neural Network Approach to Detection of Changes in Structural Parameters.
- [29] S. F. Masri, A. W. Smyth, A. G. Chassiakos, T. K. Caughey and N. F. Hunter, 2000 *Journal of Engineering Mechanics* **126**, 666-676. Application of Neural Networks for Detection of Changes in Nonlinear Systems.
- [30] J. K. C. Shih, M. Shin, R. Delpak, C. W. Hu, P. Plassmann, Wawrzynek and M. Kogut, 2000 *The e-Journal of Nondestructive Testing* **5(02)**. Application of Infrared Thermography for Damage Detection in Structural Concrete - A Preliminary Report.
- [31] W. Bai and B. S. Wong, 2000 *Institute of Physics Publishing, Measurement Science and Technology* **12**, 141-150. Evaluation of Defects in Composite Plates under Convective Environments Using Lock-In Thermography.
- [32] Y. A. Plotnikov and W. P. Winfree, *NASA Langley Research Center, M.S. 231, Hampton, VA 23681-0001*. Advanced Image Processing for Defect Visualization in Infrared Thermography.
- [33] J. G. Bakuckas JR., W. H. Prosser and W. S. Johnson, 1994 *Journal of Composite Materials*, **28(4)**, 305-328. Monitoring Damage Growth in Titanium Matrix Composites Using Acoustic Emission.
- [34] A. Quispitupa, B. Shafiq, F. Just and D. Serrano, 2003 *Engineering Structures*, Acoustic Emission Based Tensile Characteristics of Sandwich Composites.

- [35] D. Balageas, S. Bourasseau, M. Dupont, E. Bocherens, V. Dewynter-Marty and P. Ferdinand, 2000 *Journal of Intelligent Material Systems and Structures* **11**, 426-437. Comparison between nondestructive evaluation techniques and integrated fiber optic health monitoring systems for composite sandwich structures.
- [36] T. A. Anderson, G. I. Lemoine and D. R. Ambur, *American Institute of Aeronautics and Astronautics*. An artificial neural network based damage detection scheme for electrically conductive composite structures.
- [37] L. Meirovitch, *Fundamentals of Vibrations*, McGraw Hill, NY, 2001.
- [38] A. Quarteroni, R. Sacco and F. Saleri, *Numerical Mathematics, Texts in Applied Mathematics* 37, Springer, NY, 2000.
- [39] ALGOR[®] FEMPRO Version 13.22. <http://www.algor.com>.
- [40] MatWeb Material Property Data, <http://www.matweb.com>.
- [41] MATLAB[®] Version 6.0.0.88 Release 12. The MathWorks, Inc. <http://www.mathworks.com>.
- [42] P. H. Oosthuizen and D. Naylor, *Introduction to Convective Heat Transfer Analysis*, McGraw-Hill, NY, 1999.
- [43] F. Incropera and D. DeWitt, *Fundamentals of Heat and Mass Transfer*, J. Wiley & Sons, NY, 2002.
- [44] J. Ferziger and M. Peric, *Computational Methods for Fluid Dynamics*, Springer, NY, 1997.
- [45] S. Patankar, *Numerical Heat Transfer and Fluid Flow*, Hemisphere Publishing Corp., WAS. D.C., 1980.
- [46] H. Versteeg and W. Malalasekera, *An Introduction to Computational Fluid Dynamics, The Finite Volume Method*, Pearson Prentice Hall, Malaysia, 1995.
- [47] Lahey ED Version 3.80, Soft At Its Gets. <http://www.getsoft.com>.
- [48] TECPLOT Version 9.2-0-3, Amtec Engineering, Inc.
- [49] B. J. Schwarz and M. H. Richardson, 1999 *Vibrant Technology, Inc.* Jamestown, CA. 95327. CSI Reliability Week, Orlando, FL. Experimental Modal Analysis.

- [50] M. H. Richardson and M. A. Mannan, 1993 *Vibrant Technology, Inc.* Jamestown, CA. and *Royal Institute of Technology*, Stockholm, Sweden. IMAC XI. Correlating Minute Structural Faults with Changes in Modal Parameters.
- [51] M. A. Mannan and M. H. Richardson, 1990 *Royal Institute of Technology*, Stockholm, Sweden and *Structural Measurements Systems*. Milpitas, CA. IMAC VIII. Detection and Location of Structural Cracks using FRF Measurements.
- [52] Single vibrator system model VTS 100, *VTS Vibration Test Systems*. <http://www.vts2000.com>.
- [53] SigLab software, Spectral dynamics, <http://www.spectralsynatics.com>, <http://www.mathworks.com>.
- [54] DSPT SigLab Dynamic Signal Analysis system model 2042, DSPT Technology Inc. <http://www.dspt.com>.
- [55] OMETRON VH300+ Laser doppler vibrometer type 8329, Brüel & Kjær. <http://www.bk.dk>.
- [56] G. F. Lang, *Sound and Vibration, January 2005*. Experimental FEA ... Much More Than Pretty Pictures!
- [57] D. W. Banks, C. P. Van Dam, H. J. Shiu, and G. M. Miller, 2000 *9th. International Symposium on Flow Visualization*. Visualization of In-Flight Flow Phenomena Using Infrared Thermography.
- [58] Master Heat Gun[®] model HG-301A, Master Appliance Corp. <http://www.masterappliance.com>
- [59] AVIO TVS 8500 Thermal Video System, Nippon Avionic Co., Ltd. <http://www.avio.co.jp>.
- [60] GORATEC PE Professional Version 3.11, Goratec Technology GmbH. Munich, Germany. <http://www.goratec.de>
- [61] MATLAB[®] Image Processing Toolbox Version 3.1 Release 12.1. <http://www.mathworks.com/access/helpdesk/help/toolbox/images/>.
- [62] MATLAB[®] Neural Network Toolbox Version 4.0.1 Release 12.1. <http://www.mathworks.com/access/helpdesk/help/toolbox/nnet/>.

- [63] G. X. Ritter, P. Sussner and J. L. Diaz de Leon, 1998 IEEE Transaction on Neural Networks 9(2), 281-293. Morphological Associative Memories.
- [64] J. L. Ortiz, H. Parsiani, and L. Tolstoy, *University of Puerto Rico at Mayagüez*. Application of Morphological Associative Memories and Fourier Descriptors for Recognition of Noisy Subsurface Image.
- [65] G. N. Vanderplaats, Numerical Optimization Techniques for Engineering Design with Applications, McGraw-Hill, NY, 1984.

Appendix A

Matlab Code for Damage Detection

```
% -----  
%                                     Preprocessing of Vibration Data  
% -----  
  
clear all;  
clc;  
close all;  
  
% -----  
%                                     Read Vibration Data  
% -----  
  
disp(' ')  
disp(' ')  
file02 = input('    Enter Vibration Data : ');  
disp(' ')  
file01 = input('    Enter Thermal Image : ');  
disp(' ')  
  
set(0,'Units','centimeters')  
scnsize = get(0,'ScreenSize');  
figure('Units','centimeters','Position',[0 0 1*scnsize(3)  
0.95*scnsize(4)],'visible','on')  
  
if ( file02 == 0);  
else  
  
path02 = 'C:\Andres\Thesis_Andres\Modes Data\';  
Data1 = xlsread([path02 file02 '.xls']);  
nodes = Data1(:,1);  
nodes_number = nodes(length(nodes));  
  
mode01 = Data1(:,2);  
mode02 = Data1(:,3);  
mode03 = Data1(:,4);  
  
mode11 = Data1(:,5);  
mode12 = Data1(:,6);  
mode13 = Data1(:,7);  
  
mode01n = mode01./(max(abs(mode01)));  
mode11n = mode11./(max(abs(mode11)));  
  
mode02n = mode02./(max(abs(mode02)));  
mode12n = mode12./(max(abs(mode12)));  
  
mode03n = mode03./(max(abs(mode03)));  
mode13n = mode13./(max(abs(mode13)));
```



```

% -----
%                               Curvature Mode Shapes Calculation
% -----

element = nodes(2) - nodes(1);

for k = 2:(length(nodes) - 1);
    curv_m01n(k-1) = (mode01n(k-1) - 2*mode01n(k) + mode01n(k+1))/(element^2);
    curv_m02n(k-1) = (mode02n(k-1) - 2*mode02n(k) + mode02n(k+1))/(element^2);
    curv_m03n(k-1) = (mode03n(k-1) - 2*mode03n(k) + mode03n(k+1))/(element^2);

    curv_m11n(k-1) = (mode11n(k-1) - 2*mode11n(k) + mode11n(k+1))/(element^2);
    curv_m12n(k-1) = (mode12n(k-1) - 2*mode12n(k) + mode12n(k+1))/(element^2);
    curv_m13n(k-1) = (mode13n(k-1) - 2*mode13n(k) + mode13n(k+1))/(element^2);

    nodes_c(k-1) = nodes(k);
end

% -----
%                               Difference in Curvature Mode Shapes Calculation
% -----

diff_c1n = abs(curv_m01n - curv_m11n);
diff_c2n = abs(curv_m02n - curv_m12n);
diff_c3n = abs(curv_m03n - curv_m13n);

max_1 = max(diff_c1n);
max_2 = max(diff_c2n);
max_3 = max(diff_c3n);

diff1n = diff_c1n./max_1;
diff2n = diff_c2n./max_2;
diff3n = diff_c3n./max_3;

% -----
%                               Peaks in Difference Curvature Mode Shapes
% -----

[npeaks(1) ppeaks1 ind1 mean21] = npeaks(diff1n');
[npeaks(2) ppeaks2 ind2 mean22] = npeaks(diff2n');
[npeaks(3) ppeaks3 ind3 mean23] = npeaks(diff3n');

[val pos] = max(npeaks);

switch (pos)
case (1)
    ppeaks = ppeaks1;
    ind = ind1;
case (2)
    ppeaks = ppeaks2;
    ind = ind2;
case (3)
    ppeaks = ppeaks3;
    ind = ind3;
end

cpeaks(:, :, 1) = peaks(diff1n', npeaks(pos), ppeaks, ind, mean21);
cpeaks(:, :, 2) = peaks(diff2n', npeaks(pos), ppeaks, ind, mean22);
cpeaks(:, :, 3) = peaks(diff3n', npeaks(pos), ppeaks, ind, mean23);

```

```

ncpeaks(:, :, 1) = cpeaks(:, :, 1).*max_1;
ncpeaks(:, :, 2) = cpeaks(:, :, 2).*max_2;
ncpeaks(:, :, 3) = cpeaks(:, :, 3).*max_3;

% -----
%                                     Patterns
% -----

CP = zeros(size(ncpeaks,1)+1,size(ncpeaks,2)-1,size(ncpeaks,3));

for k = 1:size(ncpeaks,3);
for j = 2:size(ncpeaks,2);
    CP(1,j-1,k) = max(abs(ncpeaks(:,j,k)));
    CP(2:size(CP,1),j-1,k) = ncpeaks(:,j,k)./(max(abs(ncpeaks(:,j,k)))));
end
end

% -----
%                                     Plots
% -----

LineWidth = 1.5;
MarkerSize = 8;
MarkerFaceColor = 'k';

subplot(2,2,1);
h = plot(nodes, model1n, 'r', nodes, model2n, 'b', nodes, model3n, 'g');

grid on;
axis([0 nodes_number+1 -1.2 1.2]);
title('\it{ Mode Shapes }','fontsize',14)
xlabel('\it{ Node }','fontsize',10)
set(gca,'XTick',[1:24],'YTick',[-1.2:0.4:1.2],'fontsize',8,'PlotBoxAspectRatio',[2.5 1.25 1]);
set ( h, 'LineWidth', LineWidth, ...
        'MarkerSize', MarkerSize, ...
        'MarkerFaceColor', MarkerFaceColor )

pause(2)

subplot(2,2,1);
h = plot(nodes_c, diff1n, 'r', nodes_c, diff2n, 'b', nodes_c, diff3n, 'g');

grid on;
axis([0 nodes_number+1 0 1.2])
title('\it{ Difference Curvature }','fontsize',14)
xlabel('\it{ Node }','fontsize',10)
set(gca,'XTick',[1:24],'fontsize',8,'PlotBoxAspectRatio',[2.5 1.25 1]);
set ( h, 'LineWidth', LineWidth, ...
        'MarkerSize', MarkerSize, ...
        'MarkerFaceColor', MarkerFaceColor )

pause(2)

for s = 1:size(cpeaks,3);
for k = 2:size(cpeaks,2);

subplot(2,2,2);

```

```

switch (s)
case (1)
    LineStyle = 'r-';
case (2)
    LineStyle = 'b-';
case (3)
    LineStyle = 'g-';
end

plot(nodes_c, diff1n, 'k-', nodes_c, diff2n, 'k-', nodes_c, diff3n, 'k-');

hold on;
grid on;
axis([0 nodes_number+1 0 1.2])
xlabel('\it{ Node}', 'fontsize', 10)
set(gca, 'XTick', [1:24], 'fontsize', 8, 'PlotBoxAspectRatio', [2.5 1.25 1]);

pause(1)

h = plot(nodes_c, cpeaks(:,k,s), [ LineStyle ]);

grid on;
axis([0 nodes_number+1 0 1.2])

title(['\it{ Curvature Peak }' num2str(s) ' - ' num2str(k-
1)], 'fontsize', 14)
xlabel('\it{ Node}', 'fontsize', 10);
set(gca, 'XTick', [1:24], 'fontsize', 8, 'PlotBoxAspectRatio', [2.5 1.25 1]);
set ( h, 'LineWidth', LineWidth, ...
        'MarkerSize', MarkerSize, ...
        'MarkerFaceColor', MarkerFaceColor )

hold off;
pause(2)

end
end

% -----
%                               Probabilistic Neural Network Simulations
% -----

tic

load cnets

Y1 = sim(cnet1, CP(:, :, 1));
Y1 = vec2ind(Y1);

Y2 = sim(cnet2, CP(:, :, 2));
Y2 = vec2ind(Y2);

Y3 = sim(cnet3, CP(:, :, 3));
Y3 = vec2ind(Y3);

load CTrainData

[n m] = size(P1);

tcases = [1:m/4];

```

```

for k = 1:m/4;
tcases = [tcases ones(1,3).*k];
end

b1 = ones(size(P1,2),1)*8.3225e0;
b2 = ones(size(P2,2),1)*8.3225e0;
b3 = ones(size(P3,2),1)*8.3225e0;

for k = 1:size(CP,2);
a1(:,k) = radbas(netprod(dist(P1',CP(:,k,1)),b1));
YS1(1,k) = tcases(Y1(1,k));
YS1(2,k) = a1(Y1(1,k),k);
end

for k = 1:size(CP,2);
a2(:,k) = radbas(netprod(dist(P2',CP(:,k,2)),b2));
YS2(1,k) = tcases(Y2(1,k));
YS2(2,k) = a2(Y2(1,k),k);
end

for k = 1:size(CP,2);
a3(:,k) = radbas(netprod(dist(P3',CP(:,k,3)),b3));
YS3(1,k) = tcases(Y3(1,k));
YS3(2,k) = a3(Y3(1,k),k);
end

for k = 1:val;
Prob(:,k) = [a1(:,k) a2(:,k) a3(:,k)];
Probs = sum(Prob(:,k),2);
max_P(k) = max(Probs);
Probn(:,k) = Probs./max_P(k);
YSi = sim(cnet4,Probn(:,k));
YS(1,k) = vec2ind(YSi);
YS(2,k) = Probs(YS(1,k));
YS(1,k) = tcases(YS(1,k));
end

time = toc;

subplot(2,2,2);

for k = 1:size(YS,2);

pause(2)

h = plot(nodes_c, P1(2:n,YS(1,k)), 'r', nodes_c, P2(2:n,YS(1,k)), 'b', nodes_c,
P3(2:n,YS(1,k)), 'g');

hold on;
grid on;
axis([0 nodes_number+1 0 1.2])
title('\it{ Damage Location }','fontsize',14)
xlabel('\it{ Node }','fontsize',10)
set(gca,'XTick',[1:24],'fontsize',8,'PlotBoxAspectRatio',[2.5 1.25 1]);
set ( h, 'LineWidth', LineWidth, ...
'MarkerSize', MarkerSize, ...
'MarkerFaceColor', MarkerFaceColor )
end
end

```

```

% -----
%                                     Read Thermal Data
% -----

if ( file01 == 0);
else

path01 = 'C:\Andres\Thesis_Andres\Thermal Data\';
I01 = imread([path01 file01], 'bmp');

% -----
%                                     Preprocessing of Thermal Data
% -----

[om,on,or] = size(I01);

if ( om == 401 & on == 451);
I01 = I01(121:280,59:397,:);
else
I01 = I01(60:170,1:256,:);
end

I01 = imresize(I01,[111 256], 'bicubic');
I01 = I01(3:110,2:255,:);
I00(:, :, 1) = rgb2gray(I01);
[m,n,r] = size(I00);
count = 1;

for k = 1:r;
IM1(:, :, k) = wiener2(I00(:, :, k));
count = count + 1;
IM2(:, :, k) = im2bw(IM1(:, :, k));
count = count + 1;
end

% -----
%                                     Plots
% -----

LineWidth = 1.5;
MarkerSize = 10;
MarkerFaceColor = 'b';

subplot(2,2,3);
image(I01);
title('\it{ Thermal Image }', 'FontSize', 14);
xlabel('\it{ }', 'FontSize', 10); ylabel('\it{ }', 'FontSize', 10);
set(gca, 'XTicklabel', [], 'YTicklabel', [], 'fontsize', 8, 'PlotBoxAspectRatio', [2.5
1.25 1]);
axis equal; axis([1 253 1 107]);

pause(2)

subplot(2,2,4); [C1 h1] = contour(IM2(:, :, 1), 1, 'k-');
title('\it{ Contours }', 'FontSize', 14);
xlabel('\it{ }', 'FontSize', 10); ylabel('\it{ }', 'FontSize', 10);
set(gca, 'XDir', 'normal', 'YDir', 'reverse', 'XTicklabel', [], 'YTicklabel', [], ...
'fontsize', 8, 'PlotBoxAspectRatio', [2.5 1.25 1]);
axis equal; axis([1 253 1 107]);

```

```

[i1,j1] = find(C1==0.5);

j1(length(j1)+1) = length(C1)+1; C1(:,j1(length(j1))) = 0.5;

for k = 1:length(j1)-1;
    obj1size(k) = (j1(k+1)-1)-j1(k);
end
obj1 = zeros(2,max(obj1size),length(i1));
for k = 1:length(j1)-1;
    obj1(:,1:obj1size(k),k) = C1(:,j1(k)+1:j1(k+1)-1);
end

clear i;

obj1 = [obj1(1,:,:) + obj1(2,:,:) * i];

for k = 1:length(i1);
    cent1(k) = mean([obj1(:,1:obj1size(k),k)]);
    obj1c(:, :, k) = obj1(:, :, k) - cent1(k);
end

count = 1;

subplot(2,2,4);

for k = 1:length(i1);

contour(IM2(:, :, 1), 1, 'k'); hold on;
title('\it{ Contours }', 'FontSize', 14);
xlabel('\it{ }', 'FontSize', 10); ylabel('\it{ }', 'FontSize', 10);
set(gca, 'XDir', 'normal', 'YDir', 'reverse', 'XTicklabel', [], 'YTicklabel', [], ...
    'fontsize', 8, 'PlotBoxAspectRatio', [2.5 1.25 1]);
axis equal; axis([1 253 1 107]);

pause(1)

h= plot(obj1(:,1:obj1size(k),k));

text(real(cent1(k)),imag(cent1(k)), ['S' num2str(count)], 'FontSize', 08);
count = count + 1;
title('\it{ Contours }', 'FontSize', 14);
xlabel('\it{ }', 'FontSize', 10); ylabel('\it{ }', 'FontSize', 10);
set(gca, 'XTicklabel', [], 'YTicklabel', [], 'fontsize', 8, 'PlotBoxAspectRatio', [2.5
1.25 1]);
set ( h, 'LineWidth', LineWidth, ...
    'MarkerSize', MarkerSize, ...
    'MarkerFaceColor', MarkerFaceColor )

hold off; pause(2)

end

subplot(2,2,4); [C1 h1] = contour(IM2(:, :, 1), 1, 'b-');
title('\it{ Contours }', 'FontSize', 14);
xlabel('\it{ }', 'FontSize', 10); ylabel('\it{ }', 'FontSize', 10);
set(gca, 'XDir', 'normal', 'YDir', 'reverse', 'XTicklabel', [], 'YTicklabel', [], ...
    'fontsize', 8, 'PlotBoxAspectRatio', [2.5 1.25 1]);
axis equal; axis([1 253 1 107]);

```

```

%-----
%
%-----
Patterns

tol = 1.5e1;
c = 1;

for k = 1:length(i1);
    Iy1(k) = sum((real(obj1c(:,1:obj1size(k),k)).^2));
    Ix1(k) = sum((imag(obj1c(:,1:obj1size(k),k)).^2));
    F1(:,k) = [Ix1(k);Iy1(k)];

    if ( norm(F1(:,k)) < tol );
    else
        P(:,c) = [real(cent1(k));imag(cent1(k));Ix1(k);Iy1(k)];
        ind1(c) = k;
        c = c + 1;
    end
end

PS = [P];

load TTrainDataN

for k = 1:4;
    PNS(k,:) = PS(k,:)./max_PNT(k);
end

%-----
%
%-----
Probabilistic Neural Network Simulations

load tnets

SP = sim(tnet1,PNS);

SP = vec2ind(SP);

[o q] = size(PNT);

tcases = [1:q/2 1:q/2];

b1 = ones(size(PNT,2),1)*8.3255e0;

for k = 1:size(PNS,2);
    a1(:,k) = radbas(netprod(dist(PNT',PNS(:,k)),b1));
end

for k = 1:length(SP);
    Prob = [a1];
    Probn = Prob(:,k)./max(Prob(:,k));
    YS(1,k) = tcases(SP(k));
end

count = 1;

for k = 1:length(YS);
    switch (YS(k));
    case (3);
        tassoc(count) = YS(k);
        count = count + 1;

```

```

case (10);
    tassoc(count) = YS(k);
    count = count + 1;
case (17);
    tassoc(count) = YS(k);
    count = count + 1;
case (24);
    tassoc(count) = YS(k);
    count = count + 1;
case (31);
    tassoc(count) = YS(k);
    count = count + 1;
case (38);
    tassoc(count) = YS(k);
    count = count + 1;
case (45);
    tassoc(count) = YS(k);
    count = count + 1;
case (52);
    tassoc(count) = YS(k);
    count = count + 1;
otherwise
    tassoc = 0;
end
end

if ( tassoc ~= 0 )
load TTrainData

subplot(2,2,4); image(I01); hold on;
set(gca,'XTicklabel',[],'YTicklabel',[],'fontSize',8,'PlotBoxAspectRatio',[2.5
1.25 1]);

h = plot(PT(1,tassoc),PT(2,tassoc),'k+');
title('\it{ Damage Location }','FontSize', 14);
xlabel('\it{ }','FontSize', 10); ylabel('\it{ }','FontSize', 10);
axis equal; axis([1 253 1 107]);
set(gca,'XTicklabel',[],'YTicklabel',[],'fontSize',8,'PlotBoxAspectRatio',[2.5
1.25 1]);
set ( h, 'LineWidth', LineWidth, ...
    'MarkerSize', MarkerSize, ...
    'MarkerFaceColor', MarkerFaceColor )
else
subplot(2,2,4); image(I01); hold on;
set(gca,'XTicklabel',[],'YTicklabel',[],'fontSize',8,'PlotBoxAspectRatio',[2.5
1.25 1]);

text([55 128], 'No Damage Detected', 'FontSize', 14);
title('\it{ Damage Location }','FontSize', 14);
xlabel('\it{ }','FontSize', 10); ylabel('\it{ }','FontSize', 10);
axis equal; axis([1 253 1 107]);
set(gca,'XTicklabel',[],'YTicklabel',[],'fontSize',8,'PlotBoxAspectRatio',[2.5
1.25 1]);
set ( h, 'LineWidth', LineWidth, ...
    'MarkerSize', MarkerSize, ...
    'MarkerFaceColor', MarkerFaceColor )
end
end

%-----

```